Title

THERMOELECTRIC CHARGE IMBALANCE IN SUPERCONDUCTING ALUMINUM AND THE DEVELOPMENT OF A SCANNING TUNNELING MICROSCOPE

Author

Mamin, H.J.

Publication Date

1984-10-01

UC-37+25

LBL-18324

THERMOELECTRIC CHARGE IMBALANCE IN SUPERCONDUCTING ALUMINUM AND THE DEVELOPMENT OF A SCANNING TUNNELING MICROSCOPE

H.J. Mamin
(Ph.D. Thesis)

October 1984

Lawrence Berkeley Laboratory
University of California
Berkeley, California 94720

Prepared for the U.S. Department of Energy
under Contract DE-AC03-76SF00098

DISCLAIMER

THERMOELECTRIC CHARGE IMBALANCE IN SUPERCONDUCTING ALUMINUM AND THE DEVELOPMENT OF A SCANNING TUNNELING MICROSCOPE

Harry Jonathon Mamin

Center for Advanced Materials Division
Lawrence Berkeley Laboratory
University of California
Berkeley, CA 94720

ABSTRACT

Two experiments in solid-state physics have been performed, the observation of the superconducting fountain effect and the development of a Scanning Tunneling Microscope. In the first experiment, the quasiparticle transport current induced in a superconducting aluminum film by a temperature gradient has been measured by means of the spatially decaying charge imbalance generated near the end of the sample, where the current is divergent. The magnitude and decay length of the charge imbalance are in good agreement with the predictions of a simple model that takes into account the nonuniformity of the temperature gradient. The inferred value of the thermopower in the superconducting state agrees reasonably well with the value measured in the normal state. Measurements of the decay length of the charge imbalance induced by current injection yield a value of the inelastic relaxation time τ_E of about 2 ns, which is substantially smaller than that obtained from other measurements for reasons which are not completely understood. In the second experiment, a Scanning Tunneling Microscope, an instrument first developed at IBM Zurich, has been developed at U.C.

Berkeley in order to study surface structure. On uncleaned gold surfaces, a typical vertical resolution of 0.1 Å and a lateral resolution of 20-30 Å have been achieved, with one instance of lateral resolution under 10 Å.

John Clarke

October 30, 1984

ACKNOWLEDGEMENTS

I would never have been able to complete the work described here without the assistance of a great many people. I particularly wish to thank my advisor, John Clarke, for his guidance and support, not to mention his patience, throughout the course of these experiments. I also want to thank Dale Van Harlingen, who provided me with inspiration and instilled me with confidence. These two set high standards and helped me reach these standards, and their good humor and patience allowed me to overcome the exploded Dewars, blown-out SQUIDs, and fabrication headaches.

I have also benefitted a great deal from the other Clarke group members. Dan Seligson, Roland Lee, Tom Lemberger and Wolf Goubau all helped me make the transition from fledgling graduate student to solid-state experimentalist. I am very grateful to John Martinis for his often invaluable advice on fabrication, and to Claude Hilbert for supplying an essential component, the SQUID.

I had profitable discussions with a number of people about the thermoelectric experiment. I thank Gerd Schön, Jay Lawrence, Bruce Pipes, and Paul Dolan for sharing their insights. I thank Marianne Stuivinga for a copy of her thesis. I again thank Tom Lemberger, this time for useful discussions regarding his proposed new mechanism for charge imbalance decay. I also gratefully acknowledge the use of the Microfabrication Facility in the Electronics Research Laboratory of the University of California at Berkeley Electrical Engineering and Computer Science Department.

On the STM work, I wish to thank my coworkers, David Abraham and Eric Ganz. They have made the past year not only a productive one, but a very enjoyable one. I am grateful to our skilled machinists for their valuable contributions: Al Daft and Bob Hamilton for advice on cutting ceramics and crystals, Tom Pederson for building the sample manipulation pieces, and Andy Brocato for building the vibration isolation systems. I am also grateful to the other STM groups which have offered their knowledge and advice freely: Calvin Quate and his group at Stanford, particularly Scott Elrod and Andy Bryant; Robert Wilson and Shirley Chiang at IBM San Jose; J. Golovchenko at AT&T Bell Laboratories at Murray Hill; and the pioneering group of G. Binnig and H. Rohrer at IBM Zurich.

I thank David and Eric again for their careful editing of this thesis. Gloria Pelatowski did an excellent job on the figures with very little notice. I am grateful to the Technical Information Division word processing group of the Lawrence Berkeley Laboratory for cheerfully and efficiently typing this thesis with all its revisions.

Finally, I wish to thank my friends and my family for their support and encouragement. Their faith in me through the years helped me to persevere and complete this work.

This work was supported by the Director, Office of Energy Research, Office of Basic Energy Science, Materials Science Division, U.S. Department of Energy, under Contract No. DE-AC03-76SF00098.

TABLE OF CONTENTS

OVERVIEW. v

CHAPTER ONE: INTRODUCTION TO THERMOELECTRIC EFFECTS IN SUPERCONDUCTORS. 1

CHAPTER TWO: THEORY. 9

CHAPTER THREE: EXPERIMENTAL TECHNIQUES 21

A. Choice of Material 21

B. Sample Fabrication 22

C. Cryostat Design. 28

D. Measurement Techniques 31

CHAPTER FOUR: RESULTS AND DISCUSSION 33

A. Normal State Thermopower 33

B. Attempted Observation of $\vec{I}\cdot\vec{\nabla}T$ Effect 36

C. Measurement of λ_{Q^*} from Current Injection. 37

D. Thermopower in the Superconducting State 48

CHAPTER FIVE: SUMMARY. 56

CHAPTER SIX: INTRODUCTION TO THE STM 58

A. Overview 58

B. Background 58

C. Theory 62

D. Applications 65

CHAPTER SEVEN: CONSTRUCTION. 68

A. Vibration Isolation System 68

B. Walker Fabrication and Performance 76

C. Fine Positioning Control 84

D. Feedback Electronics 86

E. Computer Interfacing 92

F. UHV System 96

CHAPTER EIGHT: MEASUREMENTS AND DISCUSSION 98

A. Noise and Spurious Effects 99

B. Preliminary Results. 102

CHAPTER NINE: SUMMARY. 116

REFERENCES. 118

OVERVIEW

This thesis describes two quite different experiments in the field of solid-state physics performed by the author under Professor John Clarke. The first experiment, described in the first five chapters, was done in collaboration with Dale Van Harlingen. The second project, described in the remaining chapters, is being performed in collaboration with David Abraham and Eric Ganz; it is still in progress at the time of this writing. It has been a team project, and all work done so far has been the result of our joint efforts.

The purpose of the first experiment was to observe a small non-equilibrium effect predicted to exist in superconductors in the presence of a temperature gradient. Chapter One presents an introduction to this effect, including a discussion of previous attempts to observe similar effects. Chapter Two develops some of the theory of the effect, while Chapter Three describes the experimental setup. The results are presented in Chapter Four and some conclusions are drawn. Chapter Five contains a brief summary.

The second experiment involves developing a Scanning Tunneling Microscope, an instrument first developed at IBM Zurich used for looking at surfaces of metals and semiconductors. Background and fabrication details are provided in Chapters Six and Seven, while some preliminary results and future plans are discussed in Chapters Eight and Nine.

CHAPTER ONE

INTRODUCTION TO THERMOELECTRIC EFFECTS IN SUPERCONDUCTORS

Although the theory of Bardeen, Cooper and Schrieffer[1] has been quite successful in explaining the equilibrium properties of superconductors, it has not been completely adequate for explaining nonequilibrium effects. Recently a number of subtle and unexpected nonequilibrium effects have been explored, giving rise to the new field of nonequilibrium superconductivity. Pals et al.[2] have recently reviewed this field.

One class of nonequilibrium effects is that of thermoelectric effects. It is well-known that the familiar effects present in normal metals, namely the Seebeck and Peltier effects and the Thompson heat, vanish in superconductors. Thermoelectric effects do exist in superconductors, however, which are in fact unique to te superconducting state. Van Harlingen,[3] Schon,[4] and Falco and Garland[5] have recently reviewed the various effects which can occur. Study of these effects can provide useful information about nonequilibrium dynamics in superconductors.

Ginzburg[6] explained in 1944 why the normal state thermoelectric effects vanish in superconductors. He considered a two-fluid model as developed by Gorter and Casimir[7] and pointed out that a temperature gradient $\vec{\nabla}T$ in a superconductor should produce a quasiparticle current $\vec{j}_N = L_T(-\vec{\nabla}T)$ that is cancelled everywhere by a counterflowing supercurrent $\vec{j}_S$; here $L_T(T)$ is the thermoelectric coefficient. The existence of the superfluid component prevents any electrochemical

potential differences from being set up; the net current is also zero, so the thermoelectric effects are not normally observed. Any attempt to observe the effect must distinguish between the two types of current.

This effect of counterflowing normal and superfluid currents is analogous to the fountain effect in superfluid helium. (For a good discussion of similarities between superconductors and superfluid helium, see Vinen.[8]) Since this paper concerns what is often called the superconducting fountain effect, it is worthwhile reviewing the original fountain effect. This effect involves two reservoirs of liquid helium joined by a thin capillary. When one side is heated, superfluid flows through the capillary into the hotter reservoir, where the concentration of superfluid is smaller. The effect gets its name from the fact that the liquid in the hotter reservoir can easily be made to overflow.

When a steady state temperature difference is maintained between the reservoirs, a hydrostatic pressure difference is set up to balance the osmotic pressure difference. In steady state the temperature gradient across the capillary drives a flow of normal fluid from the hotter vessel to the colder. The volume rate of flow is[9]

$$\dot{\vec{V}}_N = \frac{\beta}{\eta_N} \rho S(-\vec{\nabla}T) \quad . \tag{1.1}$$

Here ρ is the density, S the entropy, β a geometrical factor, and η_N the viscosity of the normal component. This hydrodynamic flow is

cancelled by an equal and opposite flow of superfluid, just as in the superconducting case.

Clearly there is some important difference between the two cases, since the fountain effect is quite easily and dramatically demonstrated in liquid helium, while it is quite difficult to observe in superconductors. Of course, there can be no "overflow" of charge in a superconductor. Nonetheless, one might expect the thermoelectric currents to manifest themselves in some way. The difference is that in a superconductor the thermoelectric currents which flow are quite small, due to the effect of the lattice. In liquid helium, the quasiparticle-quasiparticle scattering rate is much larger than the other dominant quasiparticle scattering rate, which is that due to collisions with the container walls. This implies the flow is hydrodynamic; local equilibrium among the quasiparticles is established in the frame moving with the drift velocity of the quasiparticles. In a superconductor, the quasiparticle-quasiparticle scattering rate is much less than the scattering rate due to phonons or lattice defects, so that the hydrodynamic flow of quasiparticles is strongly suppressed. This results in very small thermoelectric currents. As seen in Eq. (1.1), a similar situation would exist in liquid helium if the normal viscosity η_N were very large, or if the geometrical factor β were very small, as would be the case in an extremely narrow capillary. It is this hydrodynamic flow and counterflow of currents which is responsible for the very large thermal conductivity of superfluid helium, while in superconductors this mechanism makes only a negligible contribution. One can say the lattice clamps the normal current in a

superconductor in the same sense that a very thin capillary would clamp the normal fluid in superfluid helium.

There have been a number of experiments designed to investigate thermoelectric phenomena in superconductors, in particular the fountain effect. Clarke and Freake[10] suggested that there should be an asymmetry in the critical current of a Josephson junction in the presence of a temperature gradient. The phase difference across the junction depends on the supercurrent flowing through it, not on the normal current, so that the junction can in some sense distinguish between the two types of current. In practice, they checked whether the external bias current needed to drive the junction into the resistive state depended on the polarity when a temperature gradient was applied. They studied Pb-Pb point contacts that were separated by an oxide tunnel barrier. Their measurements agreed roughly with the predicted effect in magnitude, and the sign was consistent with the fact that the thermopower of Pb in the normal state is negative. Welker and Bedard[11] attempted to reproduce this result using Nb. They took care to have clean, metallic point contacts and saw no effect. When they introduced surface contamination into the contact, they were able to induce an effect, but one consistently of the wrong sign. Matsinger et al.[12] also repeated the experiment with clean contacts and obtained a null result. Smith et al.[13] suggested subsequently that the effect observed by Clarke and Freake could have been produced by a thermoelectrically-induced tunneling current that arises in the presence of a temperature gradient when the energy

dependence of the height of the tunneling barrier is taken into account. However, there remains no satisfactory explanation as to why no thermoelectric effect was observed in the clean contacts. It should be noted that because of its three-dimensional geometry and thus complicated current flow, the point-contact system is not ideal for the study of the fountain effect.

In related experiments, Schmidt and coworkers[14] observed thermoelectrically-induced asymmetries in superconductor-normal metal-superconductor Josephson junctions; indeed, they were able to use heat currents large enough to induce a voltage across the junction in the absence of an electrical current. This work[15] was extended to the case of two-junction interferometers, where it was found that the thermoelectrically-induced voltage was periodic in the applied flux. Although these phenomena arise predominantly from thermoelectric currents in the normal layers, small corrections due to thermoelectric effects in the superconductors are expected. In these experiments, however, it was not possible to resolve these contributions and compare them with theory.

Other experiments have attempted to observe the electrostatic field induced by a temperature gradient which is the analog to the hydrostatic pressure difference in the fountain effect in liquid helium.[16-18] This effect cannot be measured with a normal voltmeter, which measures differences in electrochemical potential. Electrostatic techniques must be used. As these techniques are also sensitive to changes in the work function of the material, which can

be temperature dependent, these techniques give a large background signal. Some discontinuity in the electrostatic potential at T_c has been observed, although the various experiments are not totally consistent. In any event, these experiments do not measure properties related to the quasiparticle dynamics or transport coefficients in the superconductor.

Another series of experiments involved the flux induced in a bimetallic superconducting ring when a temperature difference is established between the two interfaces.[19-24] In the fountain effect, supercurrents flow through the bulk of the superconductor; these currents are associated with a gradient in the phase of the macroscopic superconducting wavefunction. The requirement that the wavefunction be single-valued imposes a condition which demands that the applied temperature gradient generate a flux through the ring. The flux observed in these experiments is generally orders of magnitude larger than predicted, and does not exhibit the predicted temperature dependence. Early experiments may have been sensitive to spurious trapped flux effects. The experiment of Van Harlingen[24] et al. involved a toroidal geometry for which such effects should not have been important. The evidence is that their observed effect was thermoelectric in origin, but the measured flux was still as much as five orders of magnitude larger than predicted by theory and diverged near T_c more rapidly than expected. It seems likely that the observed flux arises from an unconsidered thermoelectric mechanism, but there appears to be no generally accepted explanation.[3]

More recent experiments have focused on possible charge imbalance effects that may arise in the presence of temperature gradients. Charge imbalance[25] is an imbalance in the hole-like and electron-like excitations which gives rise to a detectable difference in condensate and quasiparticle chemical potentials. Falco[26] observed a voltage at a normal probe making a tunneling contact to a superconducting film carrying a heat current. However, it was later determined[27,28] that for his configuration one would not expect a voltage linear in $\vec{\nabla}T$, and in fact, Falco did not observe a change in sign when he reversed the sense of the temperature gradient. It was subsequently suggested,[27,28] that this effect arose from terms proportional to $\nabla^2 T$ and/or $(\vec{\nabla}T)^2$, and no quantitative interpretation of the experiment seems possible. Artemenko and Volkov[29] showed that a charge imbalance is generated near the end of a superconductor or near a superconductor-normal metal interface in the presence of a temperature gradient. Van Harlingen[30] investigated this effect by measuring the voltage induced across Pb-Cu-PbBi and In-Al-Sn sandwiches by a temperature gradient. He found good agreement with theory with fitted values of the thermopower about 4 times larger than that of pure normal Pb and consistent with normal state values of In. Unfortunately it was not possible to measure the normal state thermopower of the superconductors used in the experiment. Subsequently, a similar experiment reported by Battersby and Waldram[31] on Pb-Cu-Pb sandwiches gave close agreement with theory using a normal state thermopower measured in pure bulk Pb.

Finally, it should be noted that there is one class of experiments involving a thermoelectric effect for which the results are now

well-understood and in substantial agreement with theory. These experiments[32,33] involve a charge imbalance which is generated by $\vec{I}\cdot\vec{\nabla}T$; that is, a temperature gradient in the presence of a supercurrent. This effect is unrelated to the fountain effect, however, and does not involve the thermopower.

Thus, we see that many of the attempts to observe thermoelectric effects in superconductors have been unsuccessful and have produced conflicting results. Of the more successful experiments, none has been able to produce a measured value of the thermopower that can be compared with the normal state value measured in the same sample.

The present paper describes an experiment designed to measure the charge imbalance induced thermoelectrically near the end of a superconducting film by means of normal probes making tunneling contacts to the superconductor. In this way, one can measure directly the spatial decay of the charge imbalance, and thus infer a value for the thermopower that can be compared with the value obtained in the same material in the normal state. A report of this work has appeared elsewhere.[34] We outline the theory for the effect in Chapter Two. Chapter Three describes the experimental procedures, and Chapter Four contains the results and their interpretation. Chapter Five contains a brief summary.

CHAPTER TWO

THEORY

We begin with a brief review of the salient aspects of charge imbalance. The total electronic charge Q_{tot} in a superconductor can be written in the form[35]

$$Q_{tot} = \frac{2e}{\Omega} \sum_k v_k^2 + \frac{2e}{\Omega} \sum_k (u_k^2 - v_k^2) f_k \quad . \tag{2.1}$$

Here, Ω is the volume, f_k is the occupancy of the state k, $u_k^2 = (1 + \xi_k/E_k)/2$ and $v_k^2 = (1 - \xi_k/E_k)/2$, where ξ_k is the kinetic energy of an electron relative to the chemical potential of the condensate and $E_k = (\Delta^2 + \xi_k^2)^{1/2}$, with Δ the energy gap. The first term on the right hand side of Eq. (2.1) is the charge associated with the condensate, while the second term is that associated with the quasiparticles, which may be written as

$$Q^* = \frac{2e}{\Omega} \sum_k q_k f_k \quad , \tag{2.2}$$

where $q_k = \xi_k/E_k$ is the effective quasiparticle charge. The quantity q_k approaches +1 for $k >> k_F$, and −1 for $k << k_F$; as a function of ξ_k it varies smoothly from −1 to +1 over an energy range of roughly Δ.

In thermal equilibrium, $Q^* = 0$. In a nonequilibrium state for which $Q^* \neq 0$, conservation of charge requires a corresponding change in the condensate charge, introducing a shift in the pair chemical potential, μ_s. It can be shown that[35] Q^* is related to μ_s via the relation

$$Q^* = -2eN(0)(\mu_s - \mu_0) \quad , \tag{2.3}$$

where $N(0)$ is the single spin density of states at the Fermi energy, and μ_0 is the equilibrium chemical potential, which depends on electron density and temperature. This relationship is illustrated in Fig. 1.

We next discuss the introduction of Q^* and μ_s into the transport equations. The quasiparticle current in a superconductor can be written

$$\vec{j}_N = \sigma(\vec{E} - \vec{\nabla}\mu_0/e) + L_T(-\vec{\nabla}T) \quad , \tag{2.4}$$

where σ is the electrical conductivity of the quasiparticles in the superconducting state and $\vec{E}$ is the electric field. In a steady state situation, the electrochemical potential of the pairs must be constant to prevent an acceleration of the supercurrent, so that we impose the constraint

$$\vec{E} - \vec{\nabla}\mu_s/e = 0 \quad . \tag{2.5}$$

Combining Eqs. (2.4) and (2.5) we obtain

$$\vec{j}_N = \sigma\vec{\nabla}(\mu_s - \mu_0)/e + L_T(-\vec{\nabla}T) \quad . \tag{2.6}$$

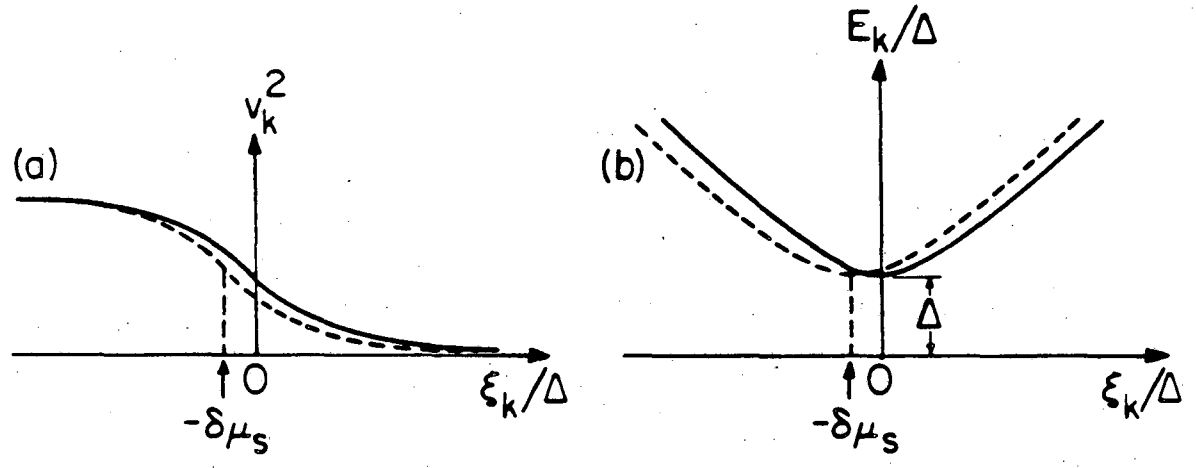

Fig. 1. (from Clarke[25]) The effect on (a) condensate density and (b) the quasiparticle excitation spectrum when an excess of electron-like excitations is present in the superconductor. In (a), the area between the two curves represents the decrease in condensate charge. By charge neutrality, this decrease must equal the charge imbalance Q*. As shown in (b), the excitation minimum is always at the actual chemical potential of the pairs.

Thus, in the absence of charge imbalance, so that $\mu_s = \mu_o$, the temperature gradient produces a normal current $L_T(-\vec{\nabla}T)$. This current will be locally canceled by counterflowing supercurrent.

On the other hand, when $Q^* \neq 0$, we can introduce Eq. (2.3) into Eq. (2.6) to obtain

$$\vec{j}_N = [\sigma/2N(0)e^2]\vec{\nabla}Q^* + L_T\,(-\vec{\nabla}T) \quad . \tag{2.7}$$

The steady-state charge imbalance is determined from the Boltzmann equation[35]

$$\frac{dQ^*}{dt} = -\vec{\nabla}\cdot\vec{j}_N - \frac{Q^*}{\tau_{Q^*}} = 0 \quad , \tag{2.8}$$

where we have assumed a relaxation time approximation so that Q^*, which is created at the rate $-\vec{\nabla}\cdot\vec{j}_N$, relaxes with a characteristic time τ_{Q^*}. We can readily solve Eqs. (2.7) and (2.8) for the one-dimensional case ($0 \leq x < \infty$) in the presence of a temperature gradient dT/dx. In addition to the constraint $j_S(x) + j_N(x) = 0$ that holds throughout the superconductor, the requirement that each current be continuous across the boundary $x = 0$ imposes the condition $j_S(0) = j_N(0) = 0$. As a result, $j_N \neq 0$ near the boundary $x = 0$, and there will be a corresponding charge imbalance. Combining Eqs. (2.7) and (2.8) we find

$$j_N - \lambda_{Q^*}^2 d^2 j_N/dx^2 = L_T \frac{-dT}{dx} \tag{2.9}$$

and

$$Q^* - \lambda_{Q^*}^2 d^2Q^*/dx^2 = \tau_{Q^*} L_T \frac{d^2T}{dx^2} \quad , \tag{2.10}$$

where

$$\lambda_{Q^*} = [\sigma\tau_{Q^*}/2N(0)e^2]^{1/2} = (v_F l \tau_{Q^*}/3)^{1/2}$$

is the charge-imbalance diffusion length, v_F is the Fermi velocity, and l is the electronic mean free path. For the case $d^2T/dx^2 = 0$, and subject to the boundary condition $j_N(0) = 0$, we can solve Eqs. (2.9) and (2.10) to find

$$Q^*(x) = 2N(0)/e^2\lambda_{Q^*} S \frac{dT}{dx} \exp(-x/\lambda_{Q^*}) \tag{2.11}$$

and

$$j_N(x) = -L_T \frac{dT}{dx} [1 - \exp(-x/\lambda_{Q^*})] \quad , \tag{2.12}$$

where $S = L_T/\sigma$ is the thermopower in the superconducting state. Figure 2 sketches j_N, j_S, and Q^* vs x.

In the foregoing discussion we have assumed complete local cancellation of normal current and supercurrent. This cancellation is a consequence of the Meissner effect, which occurs even in the presence of a temperature gradient provided the configuration is such that $\vec{\nabla} \times \vec{j}_N = 0$ (ref. 3). When this condition is violated, the London equation, which relates the magnetic field to $\vec{\nabla} \times \vec{j}_S$ (not $\vec{\nabla} \times \vec{j}_{Total}$) no longer implies the Meissner effect. Ginzburg[6] predicted that in an anisotropic superconductor, an applied temperature

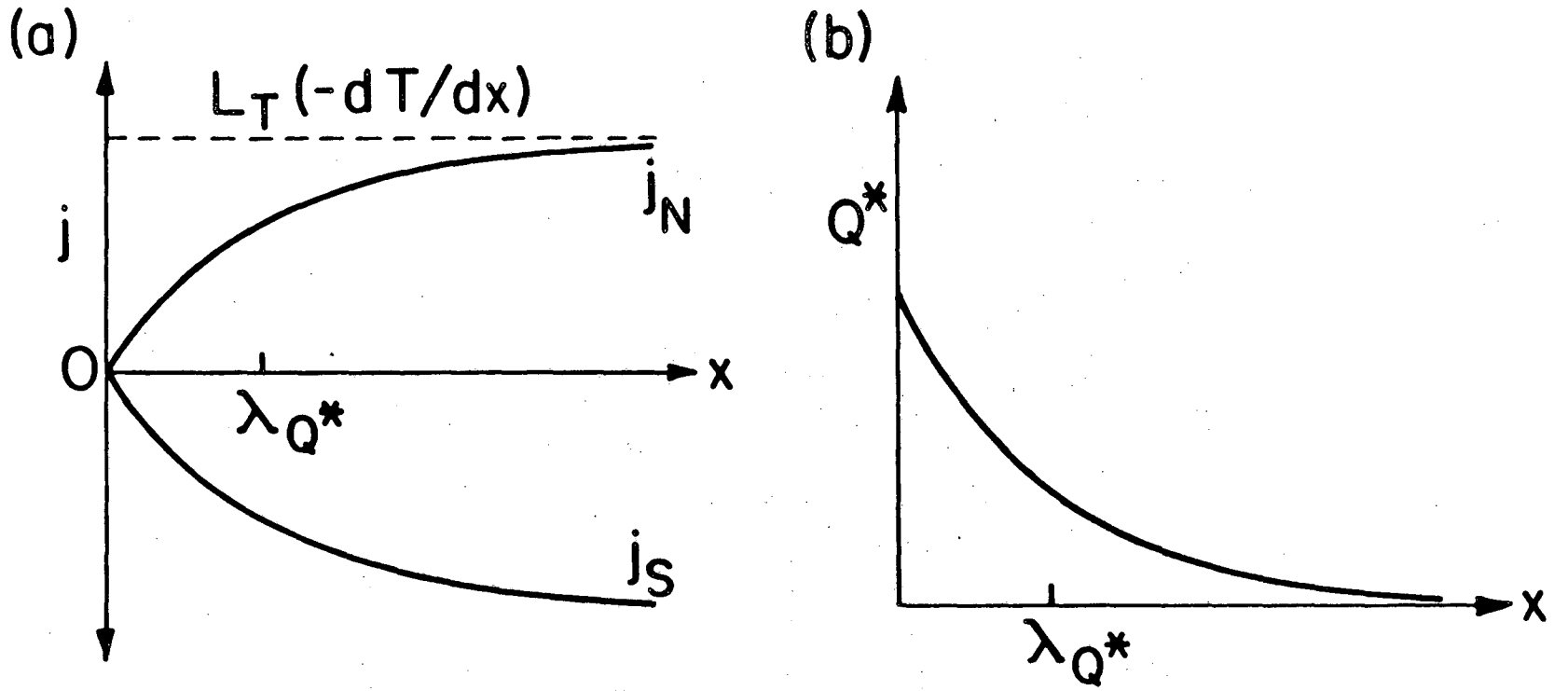

XBL 836-5953

Fig. 2. (a) Normal current (j_N) and supercurrent (j_S), and (b) Q* vs distance x near the end of a superconductor in the presence of a temperature gradient dT/dx.

gradient not along a principal axis will create a situation in which $\vec{\nabla} \times \vec{j}_N \neq 0$. The effect is to produce an excess supercurrent which flows around the superconductor, creating a flux through it. Calculations[36] done for Sn, a fairly anisotropic material, predict the effect should be observable only within a few milliKelvin of T_c. In spite of at least one attempt,[37] it is commonly believed the effect has not yet been observed. In the present experiment, the effect should be utterly negligible, and the assumption $j_N + j_S = 0$ is justified.

In the foregoing discussion we have furthermore neglected terms of order $(dT/dx)^2$, which arise from the temperature dependence of L_T and which can be shown to be very small.[28] We assumed also that $d^2T/dx^2 = 0$, but we see from Eq. (2.10) that if $d^2T/dx^2 \neq 0$ there will be an additional contribution to Q*. These effects have been used[27,28] to explain the result of Falco's experiment.[26] As we shall see in Chapter Four we shall need to take this contribution into account in our own experiment.

One detects Q* by means of a normal electrode making a tunneling contact to the superconductor. If the bias voltage across the junction is V, the current which flows is $I = G_{NS}V - G_{NN}Q^*/2N(0)e$, where G_{NN} is the zero bias tunneling conductance above T_c, and G_{NS} is the tunneling conductance at a given temperature. The first term is the usual ohmic response to a small bias voltage; the second term is the nonequilibrium term which reflects the fact that the charge imbalance induces an electrochemical potential shift. For zero tunneling

current, the voltage across the junction is $V(x) = Q^*(x)/2N(0)e^2 g_{NS}(0)$, where $g_{NS}(0) = G_{NS}/G_{NN}$ is the zero bias tunneling conductance normalized to its value at the transition temperature of the superconductor. In the experiment to be described, we measured $V(x)$ by means of a series of probes near the end of a superconducting film in the presence of a known temperature gradient. Using the above relation between $V(x)$ and $Q^*(x)$, and Eq. (2.11), we thereby determined both S and the decay length of Q^*.

The length λ_{Q^*} which describes the decay of the charge imbalance should not depend on how the charge imbalance is created. For example, experiments on Sn films have directly measured the spatial decay of charge imbalance generated by a phase slip center, which is a non-equilibrium phenomenon observed in superconducting microstrips and filaments.[38,39] Our configuration also allows us to make an independent measurement of λ_{Q^*} with $dT/dx = 0$ by passing a tunnel current through one of the junctions and measuring the voltage due to the resulting charge imbalance at nearby probes.

The decay length λ_{Q^*} depends on $\tau_{Q^*}^{-1}$, the charge imbalance relaxation rate. Some of the processes which contribute to the relaxation are shown in Fig. 3 along with the excitation spectrum $E_k = (\Delta^2 + \xi_k^2)^{1/2}$. The processes shown are all inelastic. Elastic processes are governed by the coherence factor

$$(uu'-vv')^2 = \frac{1}{2}\left(1 + \frac{\xi\xi' - \Delta^2}{EE'}\right) .$$

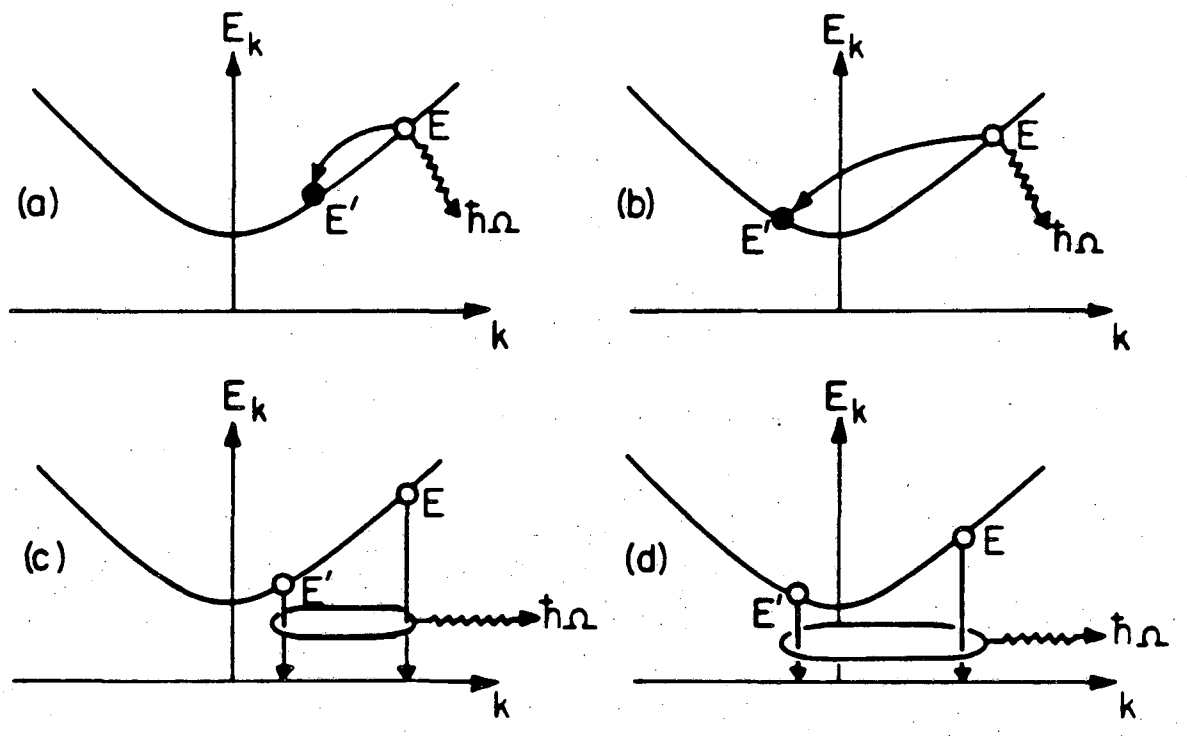

XBL 808-5642

Fig. 3. (from Clarke[25]) Four inelastic processes that contribute to the relaxation of the charge of a quasiparticle with energy E: (a) scattering to a state of lower charge on the $k>k_F$ branch; (b) scattering to a state of lower charge of opposite sign on the $k<k_F$ branch; (c) recombination with a quasiparticle near the gap edge on the $k>k_F$ branch; (d) recombination with a quasiparticle near the edge on the $k<k_F$ branch. Processes (a) and (b) are governed by the coherence factor $(uu'-vv')^2$, while (c) and (d) are governed by the coherence factor $(vu'+uv')^2$.

For an elastic process to change Q*, a quasiparticle must cross to the opposite branch of the excitation spectrum. In this case $E' = E$ and $\xi' = -\xi$. The coherence factor is then zero and this process is strictly forbidden. In the presence of gap anisotropy or inhomogeneity, the coherence factor may not be identically zero, and elastic scattering may contribute significantly. Evidence of this contribution to $\tau_{Q^*}^{-1}$ has been seen in aluminum, for which there is a sizeable amount of gap anisotropy.[40]

In the usual case in which only inelastic processes contribute, the charge imbalance relaxation rate will depend on the electron-phonon scattering rate. Of the inelastic processes, only certain processes contribute significantly, those for which the initial or final energies of one of the quasiparticles involved is within roughly Δ of the excitation energy minimum. In the process shown in Fig. 3(a), for example, if E and E' are both much greater than Δ, Q* is virtually unchanged, as the effective charge q_k only varies significantly over an energy range of roughly Δ within the excitation minimum. In Fig. 3(c), for example, for $E, E' \gg \Delta$, Q* is changed by nearly -2, but the coherence factor governing such a recombination process is nearly zero. For each process, only if E and/or E' is within about Δ of the excitation minimum will there be both significant change in Q* and significant probability of occurrence.

Roughly speaking, for $\Delta \ll k_B T$ the quasiparticles will be spread throughout an energy range of about $k_B T$, so that only a fraction $\Delta/k_B T$ will be within Δ of the excitation minimum and will contribute

to the charge imbalance relaxation. One then expects that $\tau_{Q^*}^{-1} \sim \Delta/k_B T\ \tau_E^{-1}$; here τ_E is the electron-phonon scattering time at T_c and at the Fermi surface. More detailed calculations[35,41] predict

$$\tau_{Q^*}^{-1} = [\pi\Delta(T)/4k_B T]\tau_E^{-1} \tag{2.13}$$

very close to T_c. For T far from T_c, one must solve the kinetic equations numerically to find τ_{Q^*}, as done by Chi and Clarke.[40]

Measurements of λ_{Q^*} can thus be used to infer values for τ_E, which is an important parameter in metals. The fact that τ_E is much larger in Al than in other superconductors with transition temperatures in the He^4 range immediately leads us to choose this material for the present experiment.

Finally, we remark that the transport coefficients, σ, L_T, and S in the superconducting state are expected to differ from their values σ^N, L_T^N, and S^N in the normal state as a result of coherence factors and the reduction in quasiparticle density as the temperature is lowered from T_c. In the limit $\Delta/k_B T \ll 1$, it can be shown that[4,19,42] $L_T/L_T^N = 1 - (\Delta/k_B T)^3/2\pi^2$. Since $\Delta/k_B T \leq 1$ over the temperature range $T/T_c \geq 0.9$ of interest in this paper, the two coefficients differ by at most 5%. Since the experimental error is considerably larger than this, we shall neglect any temperature dependence of L_T. The exact temperature dependence of σ appears to be the subject of some debate,[43] but the variation over the temperature range of interest appears to be small, and we shall also neglect it. Thus,

while recognizing that σ, L_T, and S are not strictly independent of temperature, for the purpose of analyzing our experimental data we shall assume that they are constant.

CHAPTER THREE

EXPERIMENTAL TECHNIQUES

A. Choice of Material

As mentioned above, we chose aluminum for the experiment because it was necessary for λ_{Q*} to be longer than the narrowest probe we could make, which was roughly 2 μm with our photolithographic setup. The decay length in Al was expected to be about 40–60 μm, a scale which can be probed readily with microfabrication. Tin, on the other hand, was expected to have a decay length of 2–3 μm, a much harder scale to probe. P. Dolan and P.B. Pipes[44] made an attempt to perform the experiment on Sn, but they concluded that the signal was too small to detect.

Although we felt the experiment was possible only using aluminum, this choice resulted in other difficulties. First, the relatively low T_c, around 1.2 K, meant that either a He^3 system had to be used, or great care taken to have a cryostat and pumping system which could reach a couple hundred mK below T_c. We adopted the latter approach and with some effort could reach 1.02 K, giving us a marginally acceptable temperature range.

The second, and much more severe, disadvantage to aluminum is that it oxidizes so readily, making it difficult to make low resistance junctions. The low resistance is necessary to reduce the level of Johnson noise because of the small signal, in the picovolt range. The small probe geometry made this all the more difficult. The fabrication procedure was dictated by the need to solve this problem.

B. Sample Fabrication

The difficulty in attaining lower resistance junctions led to a variety of fabrication schemes, including a rather convoluted one. Ideally one would place the normal metal probe material, copper in our case, on top of the aluminum without breaking vacuum. In this way the aluminum would not build up significant oxide underneath the probes. With this procedure, however, the probes must then be etched out of this copper coating. We attempted this with photoresist patterning and a chemical etch, but the undercutting was too severe; the narrow probes were etched completely away.

Our next scheme involved putting the probes down first, which could be done with a lift-off technique, and then depositing the aluminum sample over the probes. Since copper oxidizes much less readily than aluminum, breaking vacuum after depositing the copper was not a problem, and acceptably low resistances were obtained. We used this technique for many months, but we discontinued it for a number of reasons: poor step coverage, occasionally very strange I-V characteristics of the probes, and the fact that the geometry of the film under study was more complicated than if it was on a smooth flat substrate.

The final sample configuration is shown in Figs. 4 and 5. The procedure was as follows:

The Al film, typically 3000 Å thick, was evaporated onto a $(35\times10\times1)\text{-mm}^3$ glass substrate at a rate of at least 60 Å s^{-1} in a pressure of 5×10^{-7} Torr. In one region of the film we etched a $(13\times2)\text{-mm}^2$ strip on which to measure the normal-state thermopower,

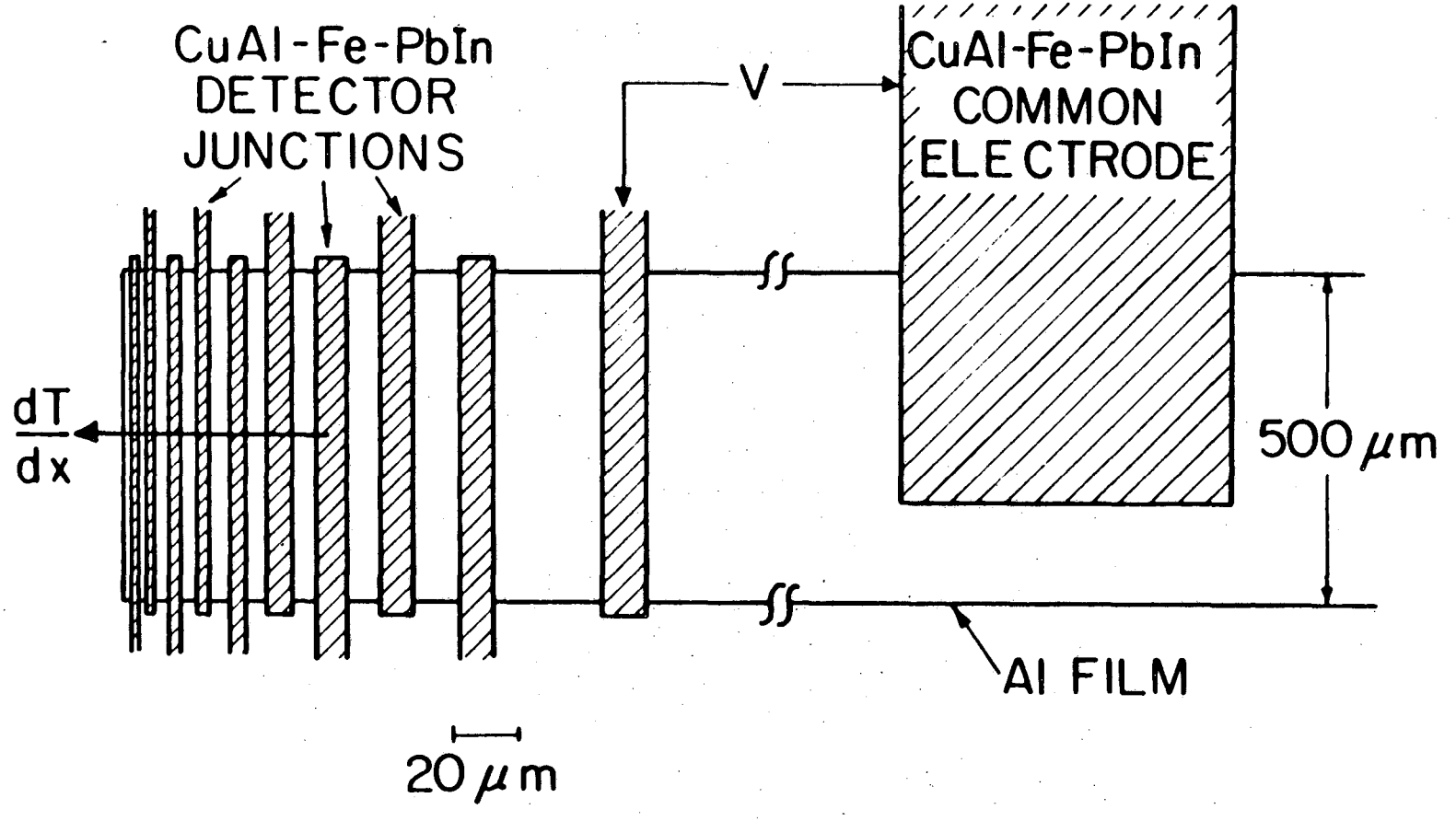

Fig. 4. Sample configuration (note different length scales).

Fig. 5. Scanning electron micrograph of typical sample showing Al strip and probes. Edge of Al film is visible on extreme left.

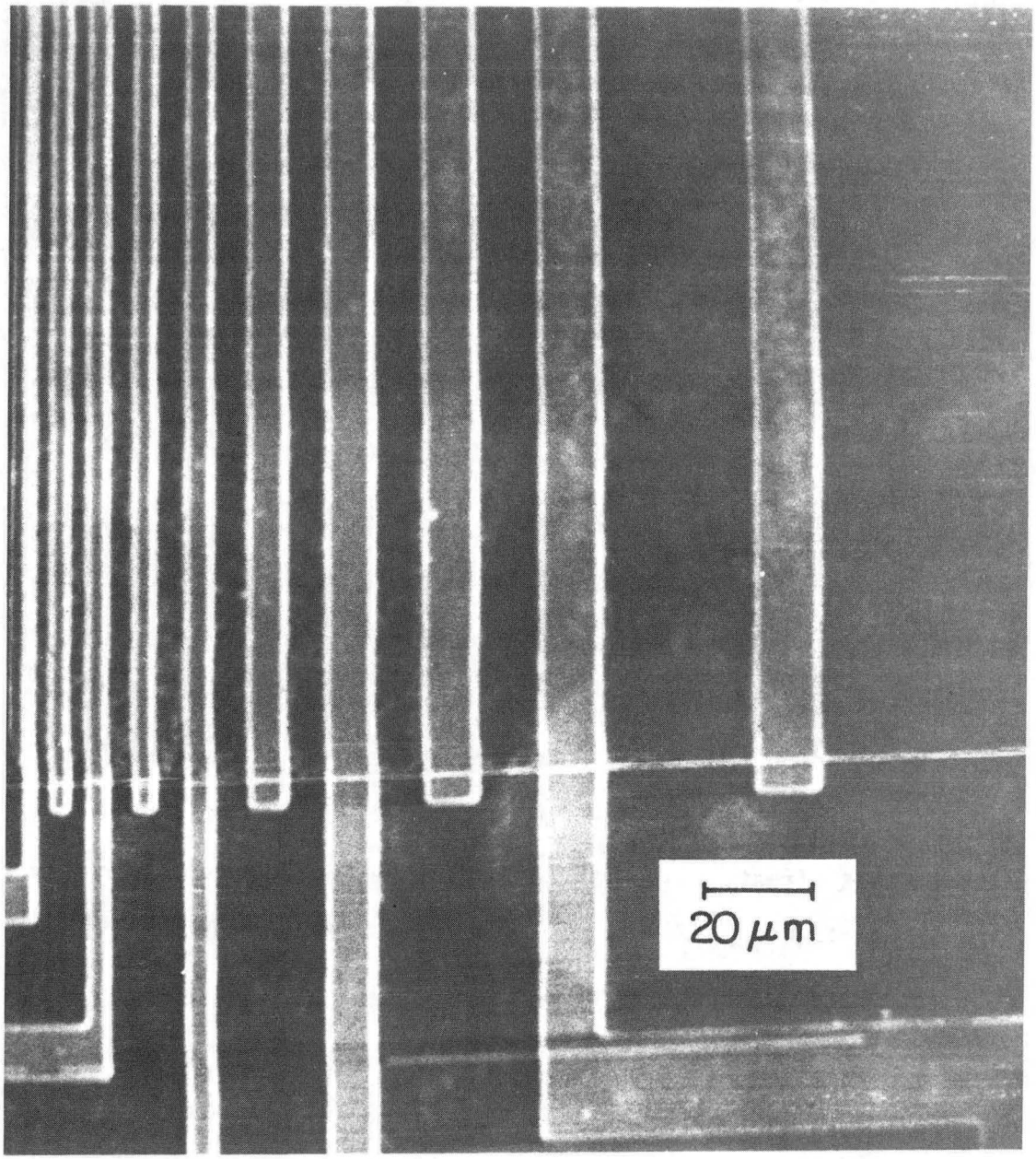

XBB 840-7439

while in another region we etched a strip 500 μm wide and 3 mm long on which to fabricate the array of probes. We next developed a photoresist pattern to make the probes via a lift-off technique. Before depositing the probes we ion-milled the Al surface in 2.5 mTorr of Ar at 1.4 kV and 10 μA mm^{-2} for 30 s. The Al was oxidized by exposing it briefly to 10^{-2} Torr of a 95 vol% Ar/5 vol% O_2 mixture, the gas was pumped out, and the probes were deposited. The ion-milling step reduced the tunneling resistance to the probes by as much as 3 orders of magnitude. The probes consisted of 8000 Å of Cu (3 wt.% Al) followed by 50 Å of Fe and 2000 Å of Pb (5 wt.% In). The PbIn eliminated the series resistance of the probes, which would have produced large levels of Johnson noise. The CuAl could not be made thicker than about 1 μm without the probes peeling off. At 8000 Å they were not thick enough to prevent Josephson tunneling; we typically saw 10-50 μA at the lowest temperature. We introduced the layer of Fe to quench this effect. Since the Fe is separated from the Al film by the thick CuAl layer, we expect it not to have affected the superconducting properties of the Al.

Near the end of the film the probes were 2-3 μm wide with 6 μm separation between centers. The sensitivity of the measurement was limited by the Johnson noise in the tunneling resistance; we reduced this resistance both by the ion-milling process and by making the junctions very long (500 μm). Ion-milling and depositing the probes in situ was absolutely essential; all other attempts which had involved breaking vacuum proved unsuccessful. Even with this step, in

the original geometry which had a 50 μm wide Al film, the resistance was too high, which is why we went to the 500 μm wide film.

With these fabrication steps, the tunneling resistance was typically 1 mΩ for the narrow probes, giving a voltage sensitivity of about 0.2 pV $Hz^{-1/2}$. Junctions farther from the end of the film were made wider to give a somewhat higher voltage sensitivity in the region where smaller signals were expected. These very low resistance junctions showed substantial leakage, and, to a good approximation, we found $g_{NS}(0) = 1$ over the temperature range studied.

The fabrication procedure had very tight margins: the ion-milling had to be energetic enough to clean off the aluminum oxide, which is quite robust, while not so energetic that it burned the photoresist. The CuAl probes had to be thick enough to reduce supercurrents, but not so thick that they peeled off. Even when the fabrication appeared to proceed flawlessly, sometimes the sample had some strange behavior such as very unusual I-V characteristics in the detector junctions. None of these samples could be used in the experiment.

Finally, many of the samples were acceptable in every way except that the probe resistances were simply too high, 10 mΩ or more. We investigated two of these to some extent, performing the current injection experiment on them. They were made using a 50 μm wide Al strip, and had probe resistances of roughly 0.1 Ω. Because of the large level of Johnson noise, there was no detectable thermoelectric effect below T_c. Of the many tens of samples fabricated, three samples had none of the above problems.

C. Cryostat Design

The sample was mounted in a vacuum can. One end of the substrate was clamped to a copper block in weak thermal contact with the helium bath and a noninductive heater was attached to the other end (Figs. 6 and 7). Three 28Ω Allen-Bradley carbon resistance thermometers were attached to the reverse side of the substrate with General Electric varnish; two were used to determine the temperature gradient while the third measured the temperature of the sample in the vicinity of the probes. A similar resistor was attached to the copper block and another was placed in the helium bath to provide temperature regulation by means of a heater and a feedback circuit. All the carbon resistors were calibrated against a Ge thermometer attached to the copper block.

Superconducting contact was made to the film by means of pressed indium contacts attached to thin strips of lead foil which ensured that thermal leakage from the sample was negligible. The lead strips were attached to terminal posts from which Nb wires were brought outside the vacuum via epoxy feedthroughs. These wires were soldered to a superconducting rotary switch that we operated from outside the cryostat to measure the voltage on each probe in turn. The switch consisted of a stationary phenolic disk with 12 pellets of PbBi cast into holes, and a rotatable disk with a solder-coated screw. The rotating part of the switch was spring loaded (at the top of the cryostat) to maintain sufficient pressure between the screw and a given pellet to produce a superconducting contact. The voltage

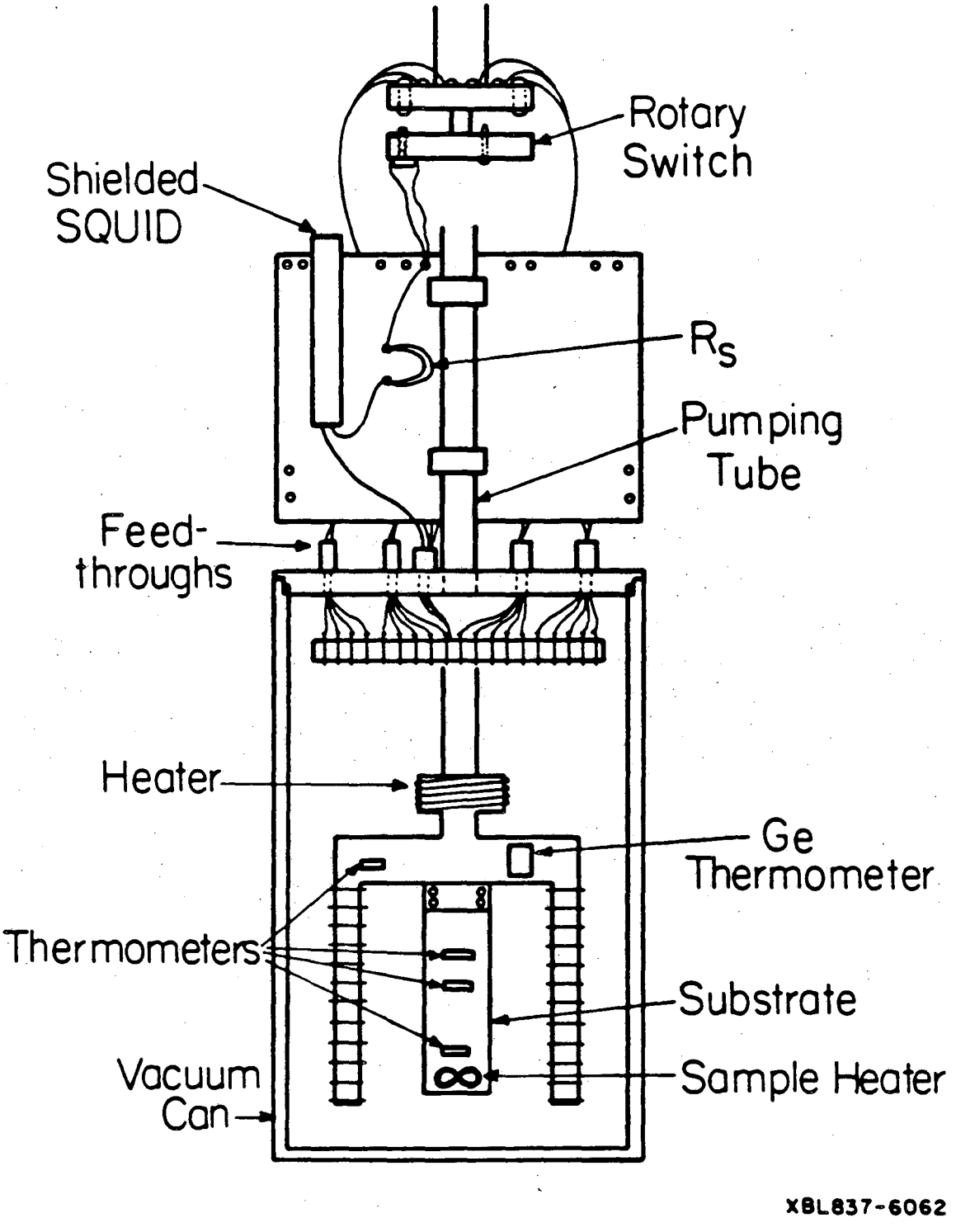

Fig. 6. Configuration of cryostat insert.

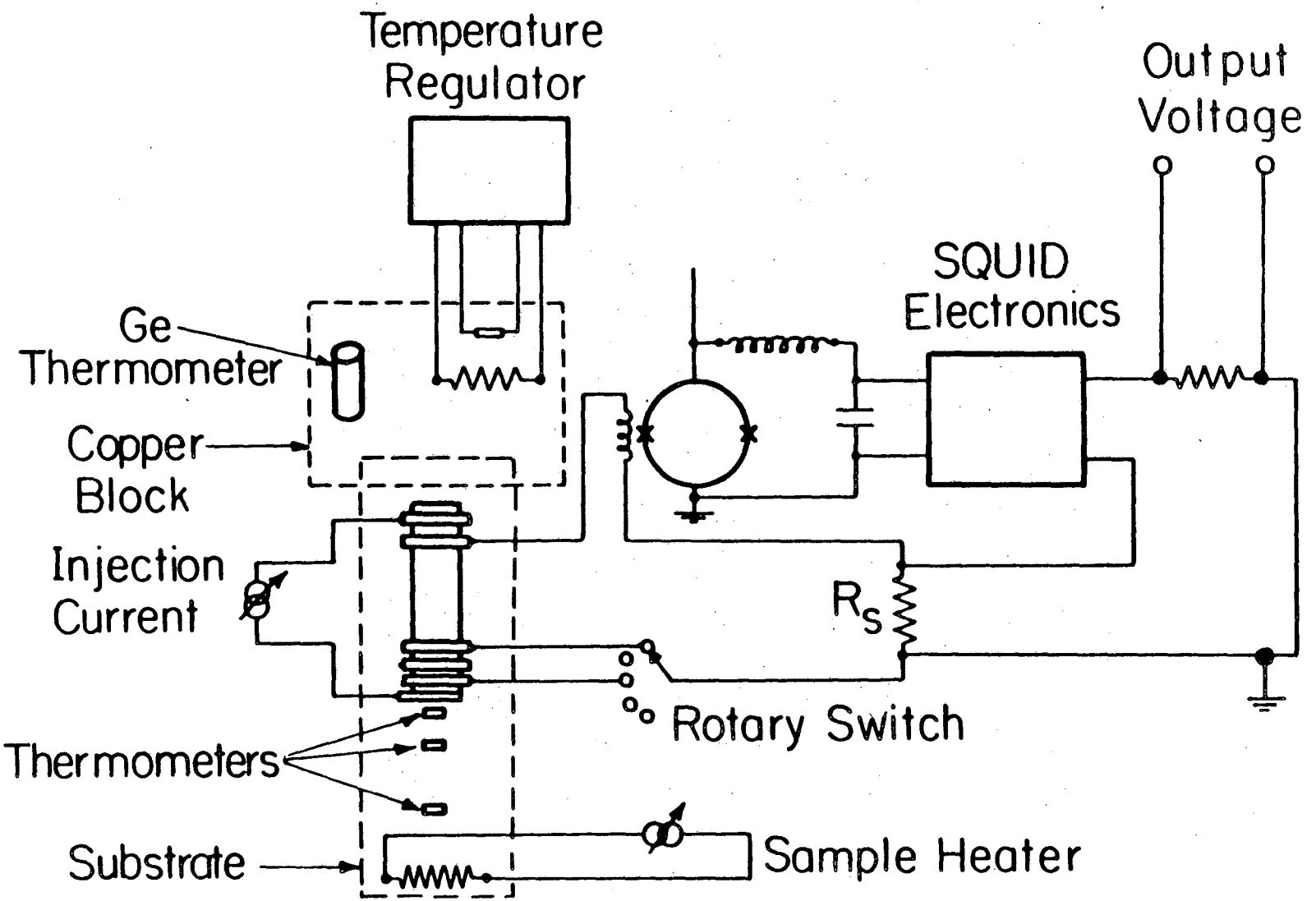

Fig. 7. Measurement circuits.

developed across each junction was measured relative to a wide junction far from the end of the strip with a null-balancing dc superconducting quantum-interference device (SQUID) voltmeter.[45] The series resistance R_s was 2.85 μΩ. The voltage gain of the feedback system was 3.5×10^9, and the noise due to the SQUID was at least 2 orders of magnitude below the Johnson noise of the junction.

All leads were secured as well as possible to minimize microphonic noise. The vacuum can, SQUID, and switch were enclosed in a lead shield, and the cryostat was surrounded with three concentric μ-metal shields. The experiment was performed in a shielded room. The insert was immersed in liquid helium, the temperature of which could be lowered to about 1 K, using a booster pump backed by a rotary pump.

D. Measurement Techniques

The voltage generated at a given probe was measured by locking the SQUID in the feedback mode, turning on the heater current to establish a known temperature gradient, and recording the output from the SQUID on a chart recorder with a bandwidth of 0.25 Hz. After the sample had reached a steady state (the thermal time constant was typically 3 s), the heater current was turned off. This procedure was repeated for a range of temperatures and temperature gradients, as well as for each probe.

We made a number of tests to eliminate spurious effects. The measured voltage was independent of the direction of the heater current, demonstrating that the magnetic flux from this source had no

effect. When the temperature of the sample was raised uniformly we observed no voltage, indicating that the effect did not arise from the temperature difference between the sample and the measuring circuit. Similarly, we observed no voltages at probes far from the end of the sample, where Q* was very small, even though the temperature gradient was the same in this region as in the region near the end. Finally, we found it essential to set the SQUID output exactly to zero before applying the temperature gradient. A nonzero output produced a feedback current in the measurement circuit that could give rise to a spurious signal because of the change in the tunneling resistance wnen the temperature of the sample was changed.

The normal-state resistance and thermopower S^N were measured by passing an electric current or a heat current through the large sample and measuring the voltage generated. To measure the charge imbalance generated by current injection, we applied a known current to one probe, and measured the voltage at neighboring probes.

CHAPTER FOUR

RESULTS AND DISCUSSION

Of the many samples studied, we have investigated three in detail. Table I lists their properties. The tunneling resistances were about $10^{-4}\Omega$ for sample 1, and $10^{-3}\Omega$ for samples 2 and 3. As mentioned above, two other samples with probe resistances of about $10^{-1}\Omega$ were investigated to some extent.

A. Normal-state Thermopower

We determined the normal-state thermopower $S^N(T)$ by measuring the voltage generated by a known temperature difference. In Fig. 8 we plot $S^N(T)$ vs. T for sample 2. We note that $S^N(T)$ is negative, implying that the charge carriers are electrons. In a free-electron model with a temperature-independent scattering time, $S^N(T)$ is proportional to T and thus becomes zero at T = 0. The plot of $S^N(T)$ vs T yields a straight line that extrapolates to a positive value of $S^N(0)$, indicating that, as expected, there are corrections to the free-electron model. In the inset of Fig. 8 we show voltage versus dT/dx for the sample; the slight nonlinearity can be accounted for by the temperature dependence of $S^N(T)$. The values of $S^N(T_c)$ obtained for the three samples are listed in Table I, and agree quite well with values quoted in the literature[46] for clean bulk aluminum, which vary from 1 to 2×10^{-8} VK^{-1} at 1.2 K.

TABLE I. Properties of Al films for three samples.

Sample	Thickness (nm)	T_c (K)	$\frac{\rho_{300\ K}}{\rho_{4.2\ K}}$	$\rho_{4.2\ K}$ (nΩm)	l (nm)	τ_E[a] (ns)	$\frac{T}{T_c}$	λ_T (μm)	$S(T/T_c)$ (10^{-8}VK^{-1})	$S^N(T_c)$ (10^{-8}VK^{-1})
1	285	1.220	6.4	5.4	75	1.6±0.2	0.992	16	-1.4±0.3	-0.94±0.06
2	165	1.241	4.4	8.5	47	2.7±0.5	0.998	14	-1.0±0.3	-1.12±0.06
3	326	1.231	6.1	5.4	75	2.3±0.4	0.913	25	-3.6±0.6	-1.05±0.06
							0.947	21	-3.3±0.6	
							0.978	19	-3.0±0.6	
							0.991	16	-2.7±0.6	

[a]Assuming only inelastic scattering processes contribute to charge-imbalance relaxation.

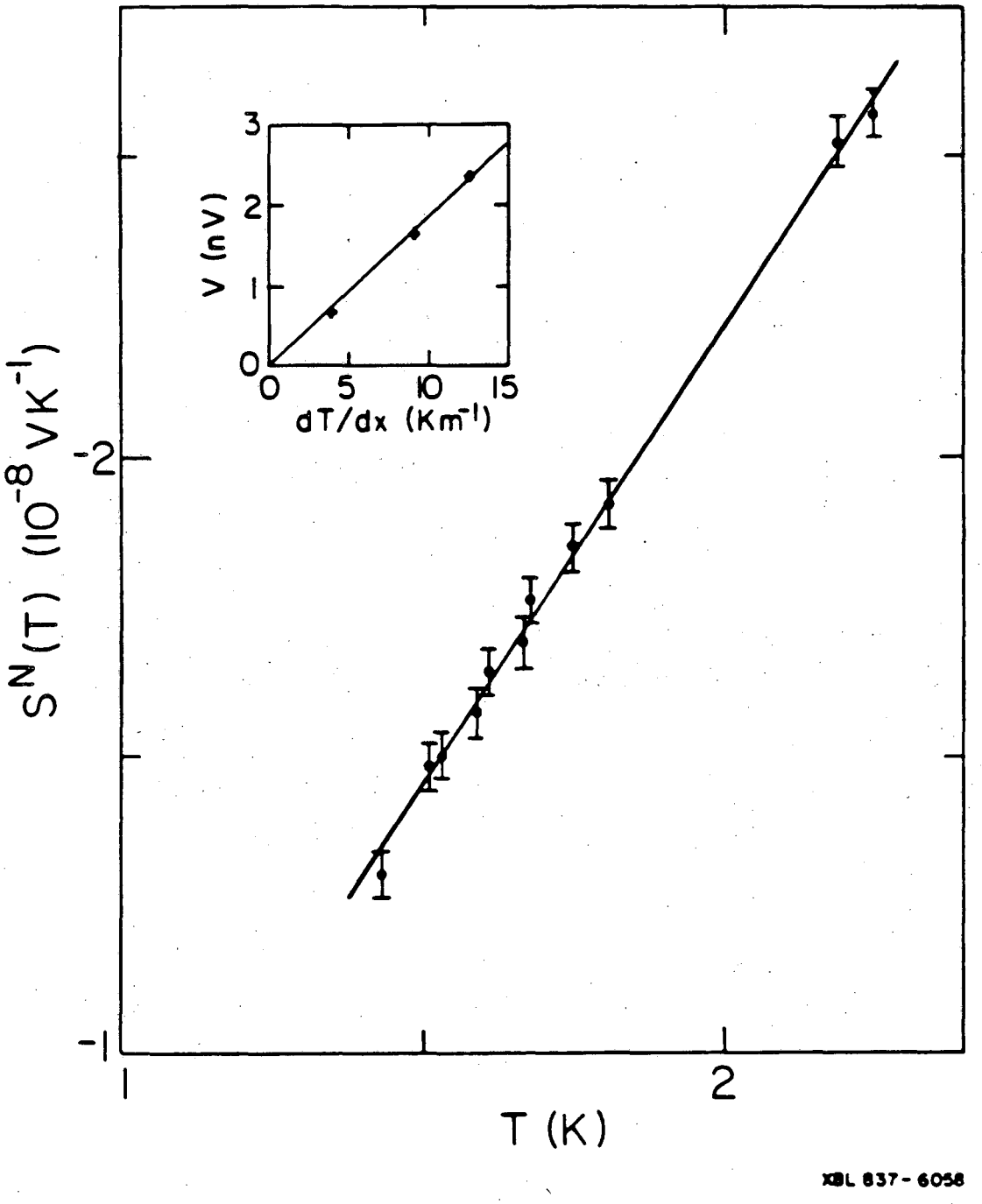

Fig. 8. $S^N(T)$ vs (T) for sample 2 in the normal state. Inset shows voltage across sample vs temperature gradient.

B. Attempted Observation of $\vec{I}\cdot\vec{\nabla}T$ Effect

As a check on our sample and measurement system, we attempted to verify the $\vec{I}\cdot\vec{\nabla}T$ effect. Unfortunately, the sample was not very well suited to this measurement in that current could only be injected through a 2 μm wide normal metal probe. The currents necessary to have any chance of observing this effect were of the order of mA. Such large currents would themselves generate a decaying charge imbalance which, even several decay lengths away, could mask the very small $\vec{I}\cdot\vec{\nabla}T$ effect. We considered adding a superconducting probe to the sample through which to inject the current, but given the difficulty already present in the fabrication process we decided to forego this step. Furthermore, the small probe geometry, which is unnecessary for the $\vec{I}\cdot\vec{\nabla}T$ experiment, limits the voltage sensitivity because of the Johnson noise.

We nonetheless attempted to observe evidence for a voltage proportional to $\vec{I}\cdot\vec{\nabla}T$ when the normal probe was used for current injection. The fact that we could not operate very far below the T_c of the aluminum when applying a temperature gradient limited us in the current we could inject before driving the film normal. With $I = 0.1$ mA and $dT/dx = 23\ Km^{-1}$, we observed no effect. Comparing to the results of Heidel et al.[34] obtained using a different geometry with much higher voltage sensitivity, we would have expected a voltage of roughly 10^{-14} to 10^{-13} V, just below the sensitivity of our experiment. Given the difficulty in our making the measurement and the fact that the effect has already been demonstrated elsewhere, we decided not to pursue it further.

C. Measurements of λ_{Q^*} From Current Injection

We determined λ_{Q^*} by injecting current through a probe and measuring the voltage at nearby probes. The injected current was typically 10 μA. In all cases, the observed voltage was accurately exponential in distance over as much as five decades: a representative example is shown in Fig. 9. Figure 10 shows the result when the current was injected through a probe some distance from the end of the sample. The observed decay length was identical on either side of the probe through which the current was injected, even though the probe spacings in the two regions were different, thereby indicating that the probes did not perturb the Al film sufficiently to affect the rate of decay of charge imbalance. This decay length was also the same as the length observed for current injection at the end of the film, although the magnitude of the charge imbalance itself in the former case was smaller by about a factor of two due to the doubling of the effective volume the charge imbalance was injected into (that is, for injection at the end of the film the charge imbalance is spread over a length of $-\lambda_{Q^*}$, while far from the end it is spread over a length $-2\lambda_{Q^*}$).

The measured values of $\lambda_{Q^*}(T)$ range from about 20 μm close to T_c to 7 μm at the lowest temperature investigated. In Figs. 11 and 12 we plot $\lambda_{Q^*}(T)$ vs $1-T/T_c$ for samples 1, 2 and 3. The slopes are -0.22 ± 0.03, -0.20 ± 0.03, and -0.24 ± 0.02, respectively. We estimate τ_{Q^*} from $\tau_{Q^*} = 2N(0)e^2\lambda_{Q^*}^2/\sigma$ using the measured values of λ_{Q^*} and σ and taking[47,48] $N(0) = 1.74 \times 10^{28}$ eV^{-1} m^{-3}. If we assume for the

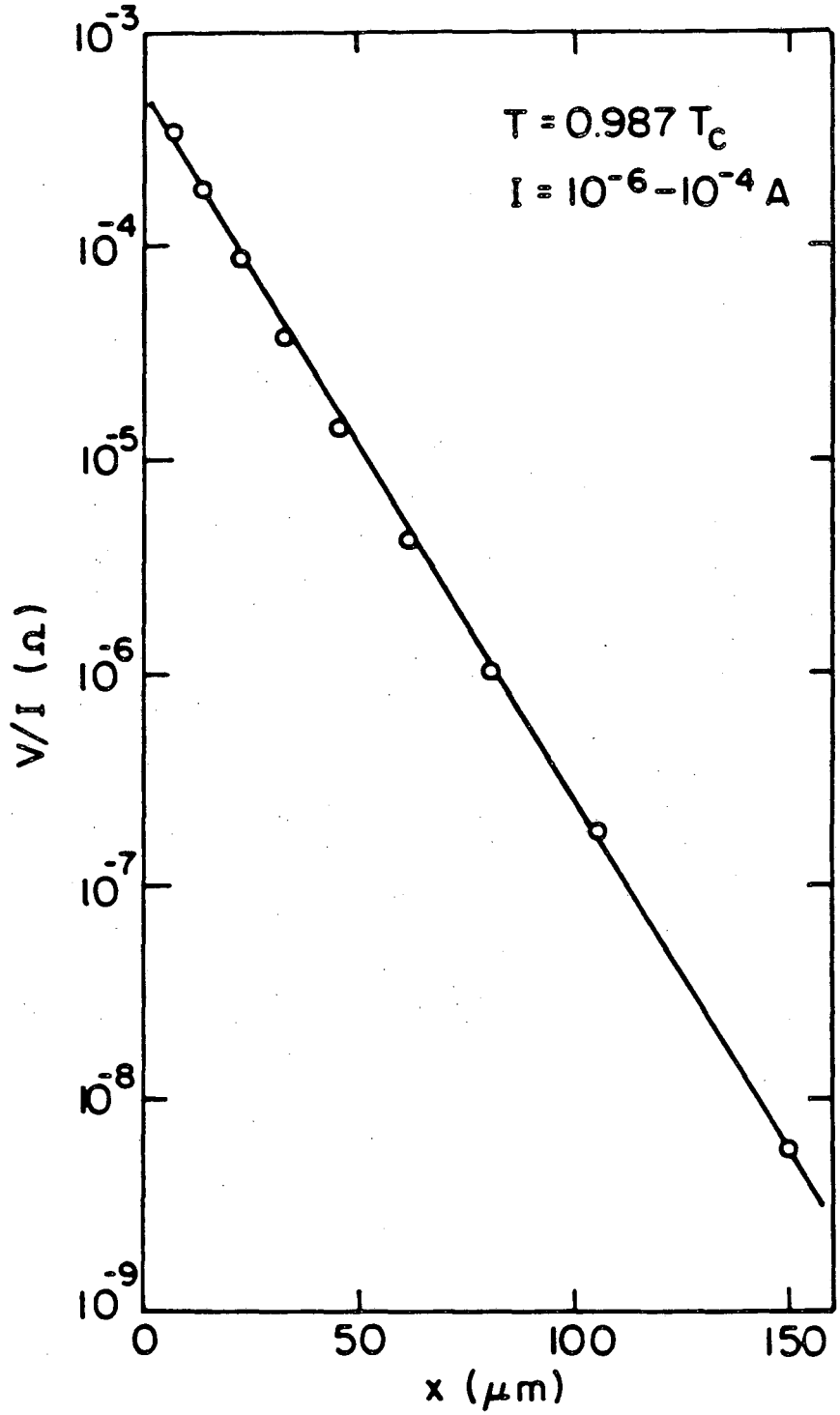

Fig. 9. Measured λ_{0*} from current injection: Voltage V normalized to injection current I for a series of probes on sample 2.

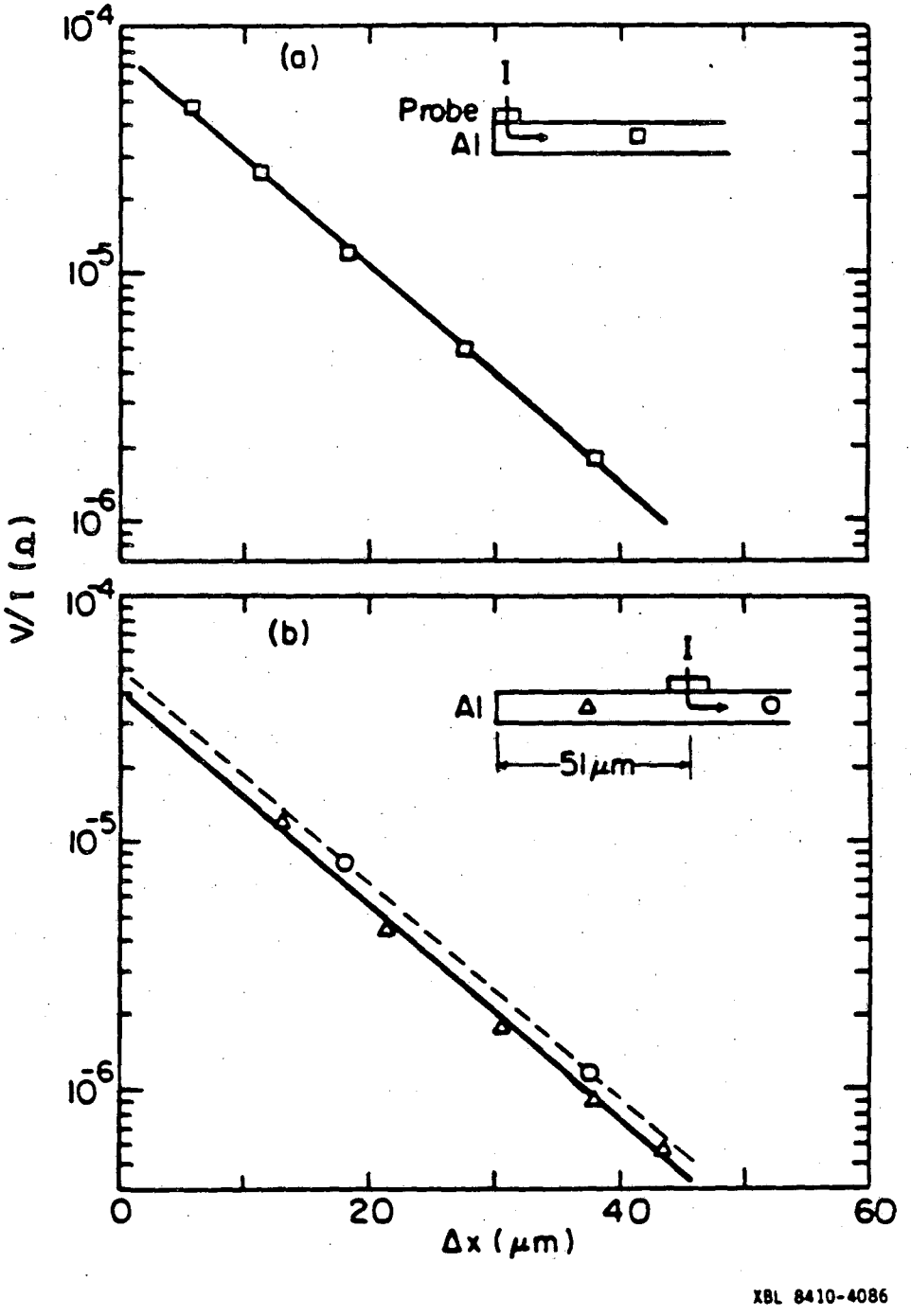

Fig. 10. Measured λ_Q^* from current injection for sample 3 at $T = 0.890\ T_c$. (a) Current injected through probe 1 at end of sample; $\lambda_Q^* = 10.0\ \mu m$. (b) Current injected through probe 6. Probes 1-5 (Δ) give $\lambda_Q^* = 10.1\ \mu m$; probes 7 and 8 (○) give $\lambda_Q^* = 9.9\ \mu m$. The finite width of the injection probe leads to uncertainty in the origin x = 0 and may explain why the data points do not lie on exactly the same line.

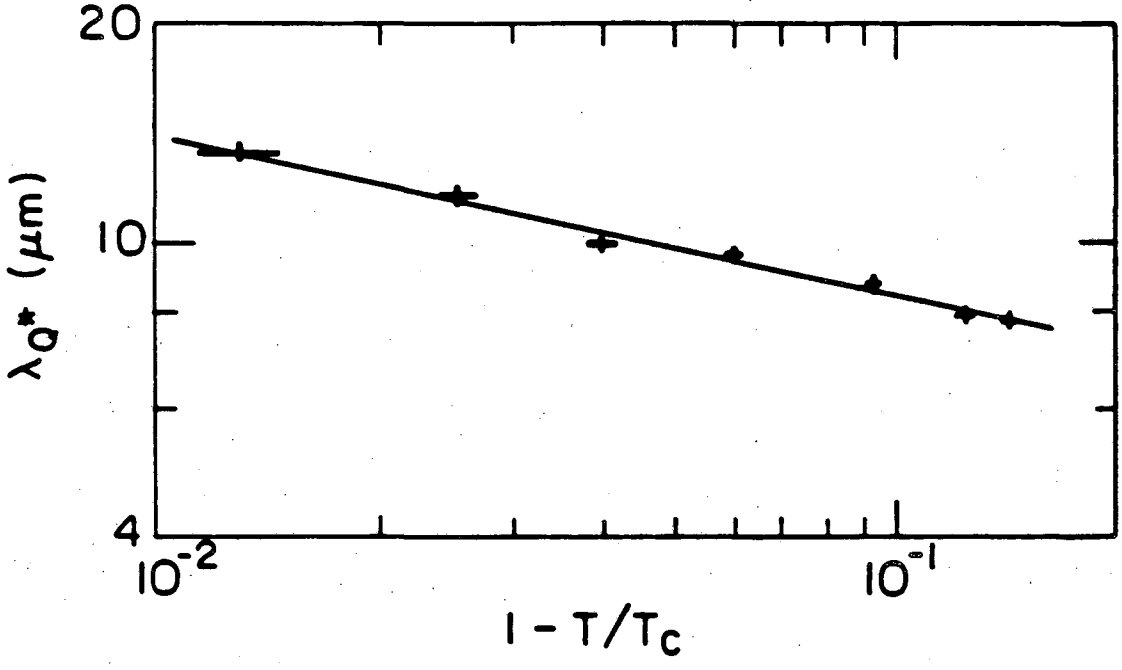

Fig. 11. Temperature dependence of λ_{Q^*} from current injection: λ_{Q^*} vs $1 - T/T_c$ for sample 1.

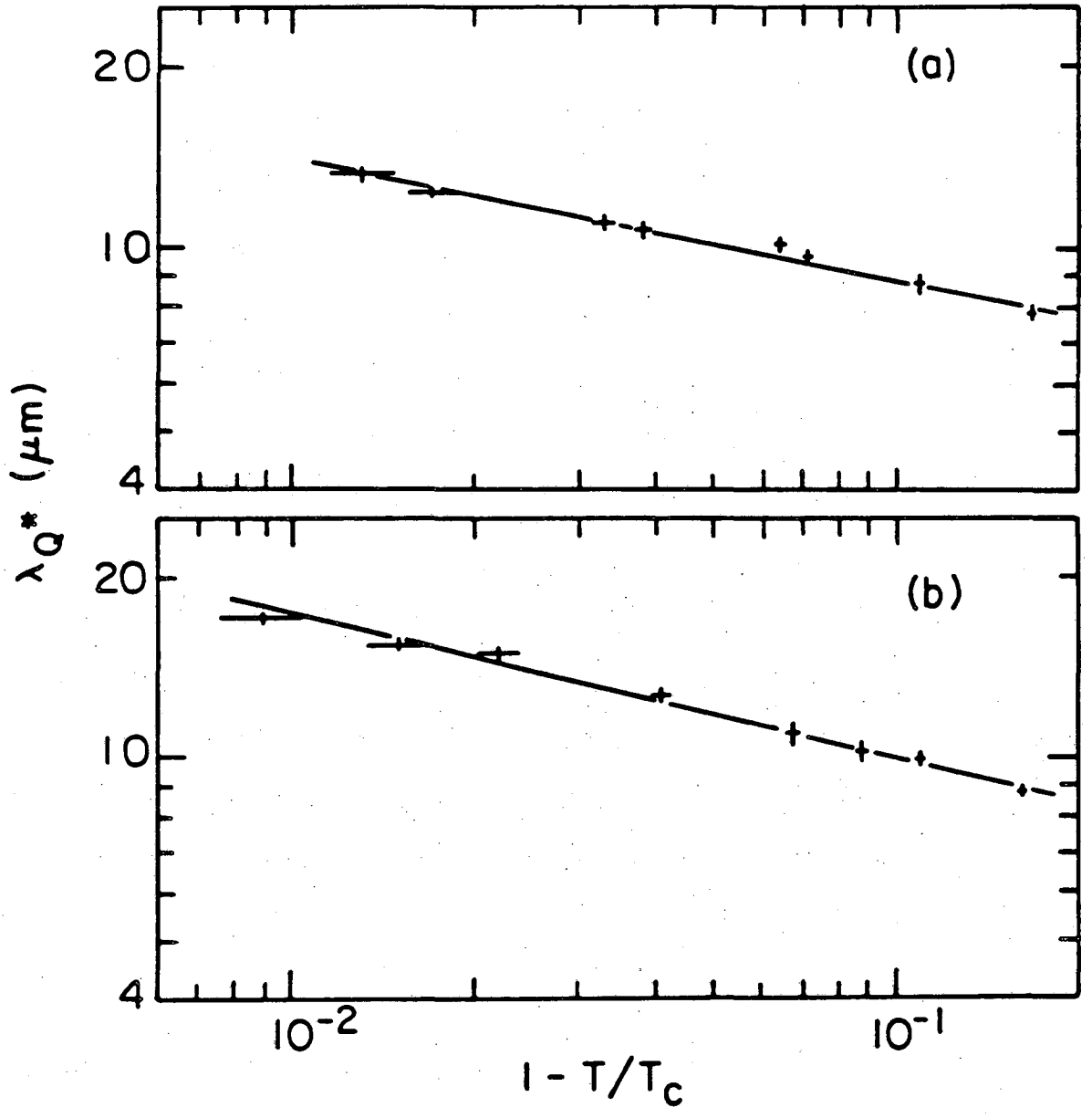

Fig. 12. λ_{0*} vs $1 - T/T_c$ for (a) sample 2 and (b) sample 3.

moment that only inelastic processes contribute to the charge relaxation, we can then estimate τ_E from Eq. (2.13). These values are listed in Table I.

These results, in the light of previous estimates[40] of τ_E, are very puzzling. First, the fact that the slope of log λ_{Q*} vs $\log(1 - T/T_c)$ is, to within the experimental accuracy, equal to -1/4, implies that τ_{Q*}^{-1} is proportional to Δ. One would expect this result very close to T_c if inelastic processes alone contribute to the charge relaxation. However, over the temperature range studied, we expect a more rapid decrease of λ_{Q*} with decreasing temperature due to the onset of charge relaxation via elastic scattering in the presence of gap anisotropy. This would make the slope steeper than -1/4, whereas the data yield a slope, that, if anything, is slightly less steep[49] than -1/4. Second, the inferred value of τ_E, about 2 ns, is about a factor of 6 smaller than that obtained by Chi and Clarke[40] (CC) on films with very similar transition temperature and mean free path. In the CC experiments, charge imbalance was created by current injection through a tunnel junction on one side of the Al film, and detected by means of a tunneling contact on the other side of the film. In order to eliminate the possibility that the Al used in the present experiment was in some way different to that used in the earlier CC experiments, we fabricated two samples in which the Al was deposited simultaneously, one in the configuration of the present experiment and one in the CC configuration. The transition temperature and mean free path of the films were comparable to those of samples 1 and 3. For

the CC-type sample we found that the plot of $\tau_{Q^*}^{-1}$ vs Δ/k_bT showed substantial upward curvature implying a significant contribution from elastic scattering. This contribution was estimated by fitting the data to the computed curves in CC. The remaining inelastic contribution was found to correspond to $\tau_E = (11\pm3)$ ns, in excellent agreement with the values obtained by CC. By contrast, the values of $\tau_{Q^*}^{-1}$ obtained from the measurement of λ_{Q^*} yielded $\tau_E = 2.2$ ns. We note, incidentally, that the supercurrent density in the Al strips during the decay-length measurements was much too small to have any measurable effect on the charge-imbalance relaxation.[50]

The discrepancy between the two measurements of τ_E is startling, and we have no explanation for it. However, the value of 2 ns is only a factor of 2 below the value obtained by Stuivinga et al.[51,52] (using $\rho l = 4 \times 10^{-16}\ \Omega m^2$) from measurements of λ_{Q^*} in Al films near phase slip centers. These authors suggest that their films may be thin enough that electron-electron scattering could contribute significantly to the charge relaxation. However, our films are too thick for this effect to be significant. In any case, we made both types of measurement on the same film.

One concern is that perhaps the probes themselves alter the measurement; that is, that they perturb the underlying film so as to induce an additional mechanism for charge imbalance decay. The experimental evidence is strong that any such perturbation is slight. The probes would presumably affect only the aluminum more-or-less directly underneath, so one would expect the observed decay length to depend on

the probe spacing: where the probes are spaced more closely, more aluminum is covered, and the perturbation would be greater. As mentioned above, no such dependence on probe spacing was observed.

As a further check on whether this effect was significant, we looked at samples with a wide range of tunnel resistances. Any proximity effect from the probes must scale with the junction resistance. For sample 1 this was a few times $10^{-4}\Omega$, for samples 2 and 3 it was roughly $10^{-3}\Omega$, and for the two 50 μm wide samples studied the probe resistances were of order $10^{-1}\Omega$, equivalent to $10^{-2}\Omega$ on a 500 μm wide strip. Effective probe resistances thus ranged over a factor of about 30 from sample to sample. The two 50 μm samples are not listed in Table I, as they were investigated much less thoroughly than the other samples. The values for τ_E obtained for these two, 3.5 ± 0.8 and 3.3 ± 0.8 ns, are slightly higher than but fairly consistent with values obtained for samples 1, 2 and 3. If the probes were perturbing the sample significantly, one would expect that an increase in the junction resistance of a factor of 30 would be reflected in the observed decay rate. We see some slight increase in τ_E which may or may not be significant, but the large discrepancy between these and other measurements of τ_E still remains.

When the experiment was performed, there was no theory available for estimating the effect of the probes on the charge imbalance decay rate. For this reason we satisfied ourselves with the experimental checks listed above. Recently Lemberger[53] has developed a theory which makes quantitative predictions for the additional charge

imbalance relaxation due to the proximity of the normal probes. His model predicts that for our probe resistances, the charge imbalance rate should be increased significantly, as much as by a factor of 10 if the aluminum film were uniformly covered by the probe material. Because of this large predicted effect, we felt it necessary to perform a detailed computer calculation for the effect in our geometry.

The Lemberger model assumes the superconducting film thickness is small compared to a coherence length. In our films, the thickness was 3000 Å and the G-L coherence length at 0.9 T_c was about 10,000 Å, so this assumption is not completely valid. For this reason the following computations give an overestimate for the effect. The Lemberger model also assumes probe geometries much larger than the charge imbalance decay length, clearly not the case here. To account correctly for our geometry, we solved the differential equation governing the decay separately under each probe and in each region between probes, using the actual probe dimensions and resistances. We then matched these solutions by imposing the boundary conditions that Q* and dQ*/dx be continuous. The first condition is necessary to avoid infinite currents, and the second requires the current to be continuous, which is necessary in steady state. These continuity conditions are important in that they smooth out and therefore reduce the effect of the probes. We solved the differential equations for various values of τ_E, choosing the one which gave the best fit.

Taking this new effect into account, we saw the biggest change in τ_E for sample 1, because its probe resistance was lowest. The best

fit was obtained for τ_E = 3.0 ns, a significant change from the 1.6 ns we otherwise inferred, but still significantly different from the 12 ns or so measured in other ways. As seen in Fig. 13, the 12 ns curve is still a very poor fit. For samples 2 and 3, which had higher probe resistances, the fitted values of τ_E were within 10% of what they would be without taking this effect into account. Recalling this is still an overestimate, we see that for our geometry the predicted effect is very small in two of our samples, and may be significant in one, which might explain why our value for τ_E came out somewhat lower in that one. These results are consistent with the experimental checks we made, which suggested a very slight effect.

We are still left with the problem of why measurements of τ_E in Al do not agree, while they do agree in other materials such as Sn.[38,54] One difference is that the electron-phonon scattering time is much longer in Al than in these other materials. It is possible that other mechanisms which would play a small role in these materials could be much more significant in Al. Another possibility is that the grain boundaries in Al induce additional charge imbalance relaxation. Since the charge imbalance propagating along a film would encounter more grain boundaries than that flowing through the film from top to bottom, the observed relaxation rate would depend on which type of measurement was being made. In any case, it remains an open question.

In concluding this section we emphasize that the discrepancy with theory in the measured value of the magnitude and temperature dependence of λ_{Q^*}, although of considerable inherent interest, does not

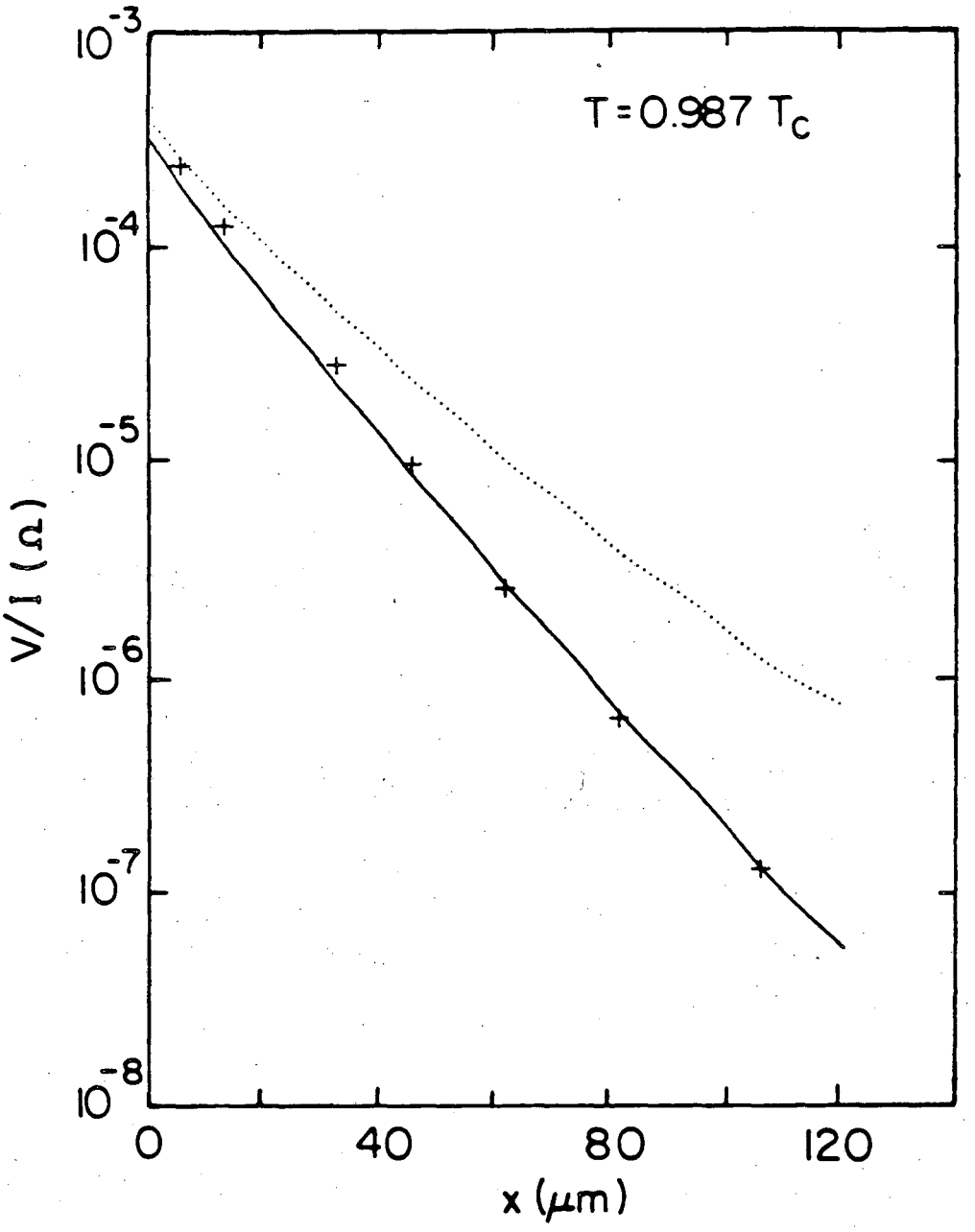

XBL 8410-4084

Fig. 13. Measured and calculated charge imbalance decay from current injection. Data (+) are from sample 1 at T = 0.987T_c. Curves were calculated taking into account a new charge imbalance mechanism predicted by Lemberger.[53] Dotted line is for τ_E = 12 ns, while the solid line is for τ_E = 3 ns. The size of the crosses slightly overestimates the uncertainty in the data.

enter into our subsequent discussion of the thermopower in the superconducting state. To analyze the thermopower data, we require only the actual value of λ_{Q*}, obtained from the current injection measurements.

D. Thermopower in the Superconducting State

We now turn to a discussion of the charge imbalance generated by a temperature gradient. Figures 14 and 15 show V(x) vs x for samples 1 and 2 at one temperature and for sample 3 at four temperatures. The temperature gradients were typically 20 K m^{-1}, giving a temperature change of about 2 mK over the distance shown in the figures. Thus, we are justified in assuming that τ_{Q*} is constant over the measured regions. Figure 16 shows that the voltage at the probe near the end of the film was nearly linear in dT/dx. We could not use substantially higher gradients because part of the Al film would then have been above T_c.

For sample 3, the voltage at 0.991 T_c varied from 5.3 pV at the probe 6 μm from the end of the film to 0.55 pV at the probe 68 μm from the end. In contrast to the current-injection results, the voltage shows a significant downward curvature near the end of the Al film. A straight-line fit to several of the data points furthest from the end yields a decay length of (24 ± 4) μm. This decay length is independent of temperature to within the fitting uncertainty of about ±15%. By contrast, the decay length measured from current injection (Section C) varied approximately as $(1 - T/T_c)^{-1/4}$, which changes by a factor of about 1.8 over the temperature range studied for this sample.

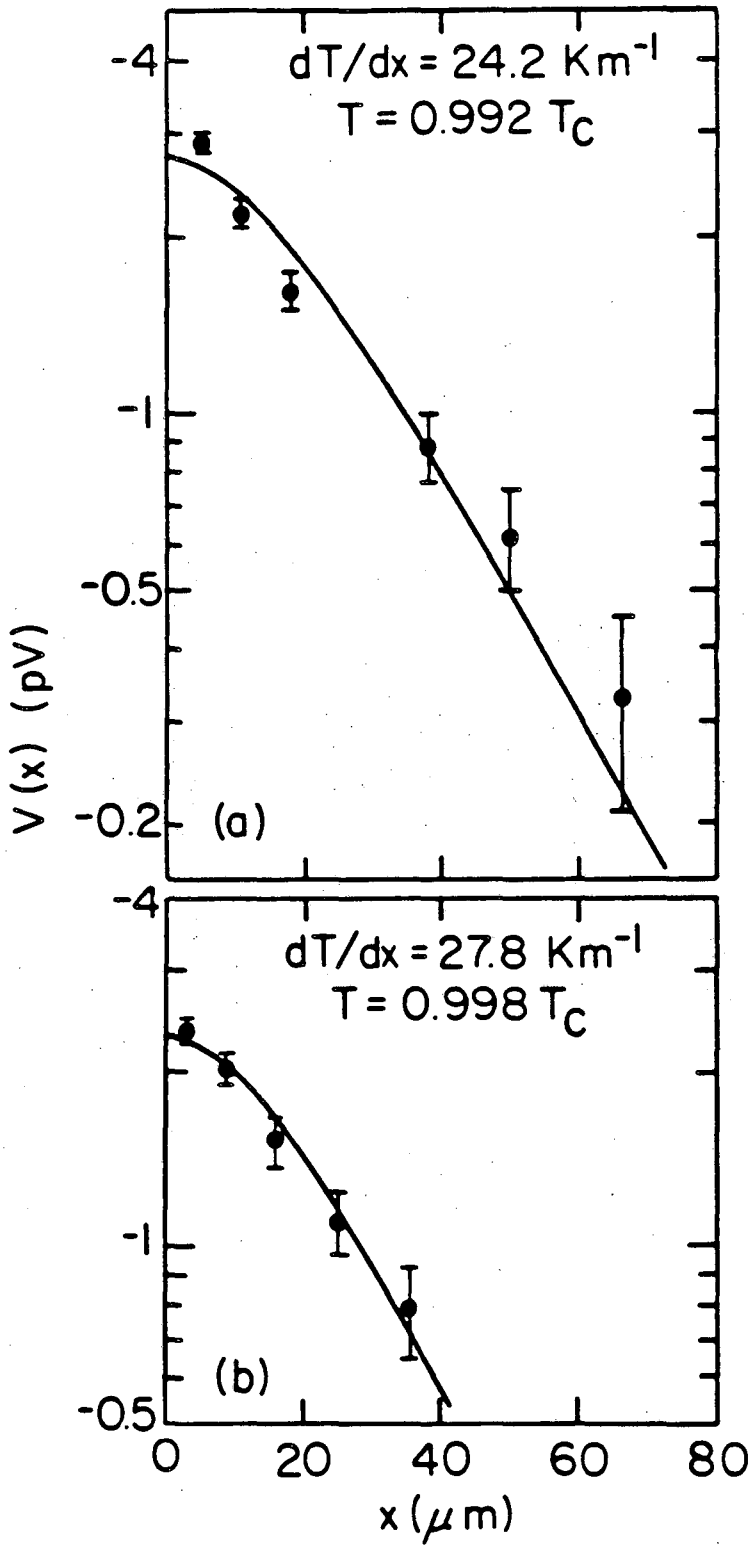

Fig. 14. V(x) vs x for thermopower measurements on (a) sample 1 and (b) sample 2. Solid lines are fits to Eq. (4.3).

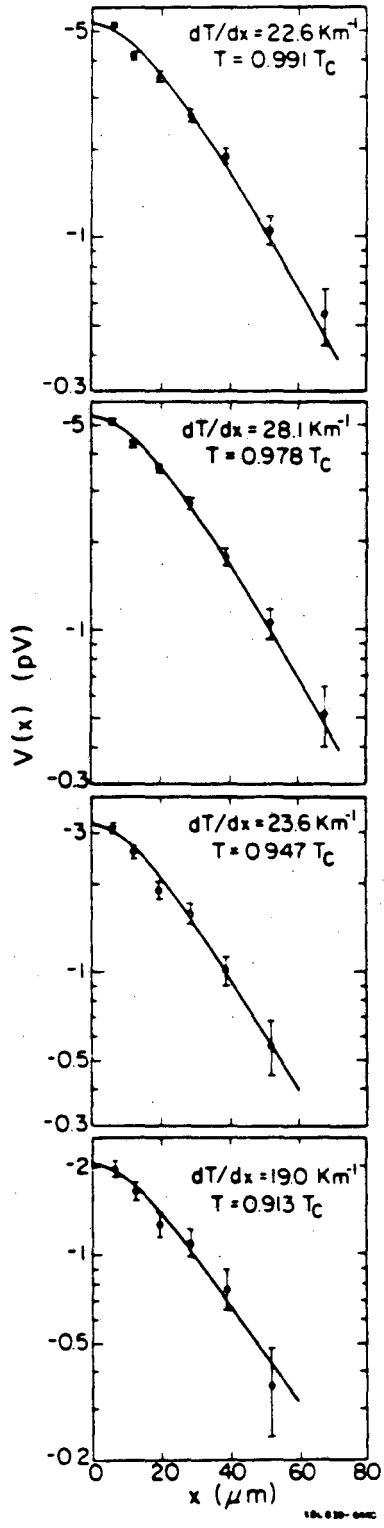

Fig. 15. V(x) vs x for thermopower measurements on sample 3 at four different temperatures. Solid lines are fits to Eq. (4.3).

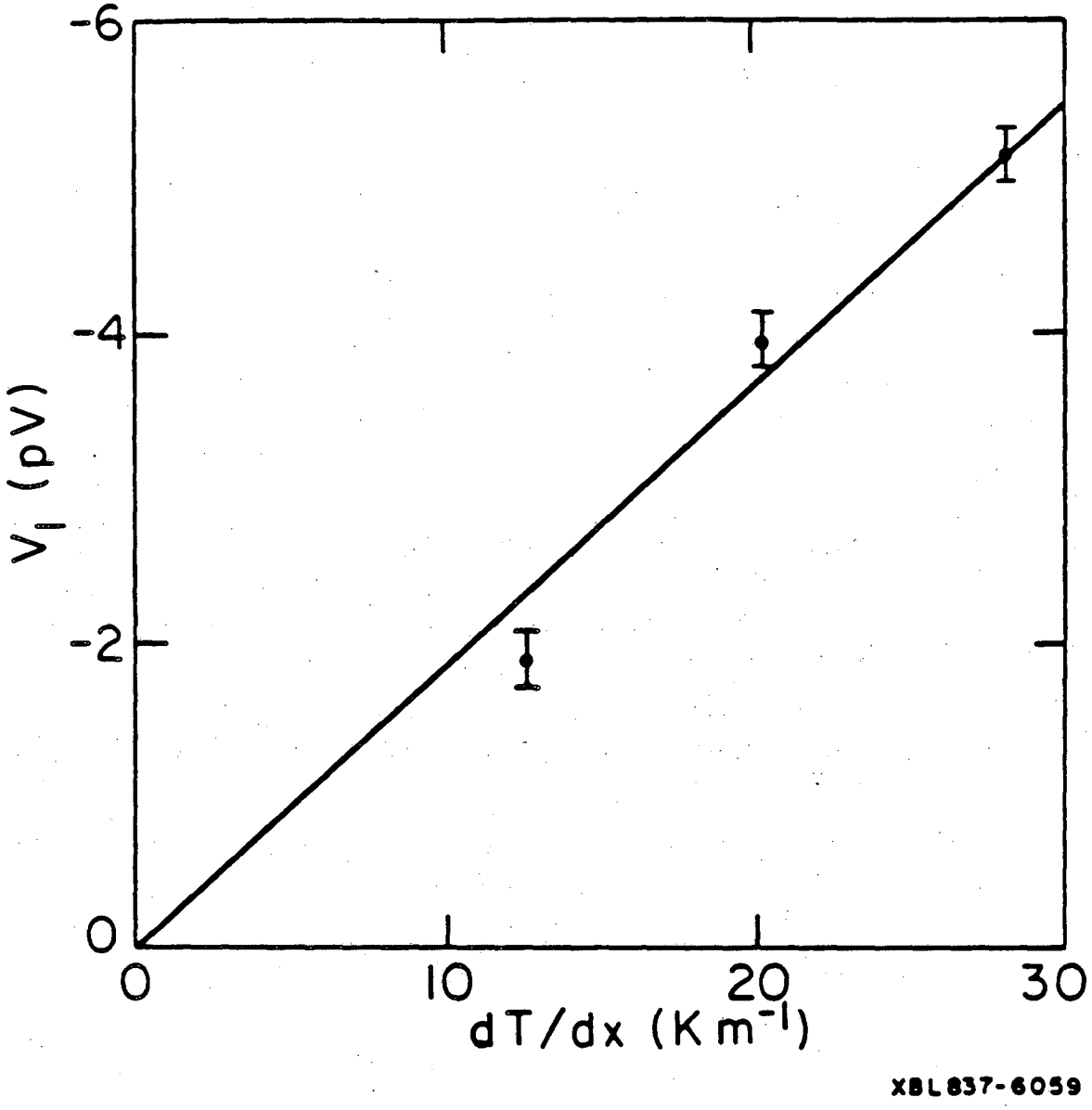

Fig. 16. Voltage measured at first probe V_1 vs dT/dx for sample 3 at $T = 0.987T_c$.

Furthermore, the length obtained from current injection was always shorter than the length measured in the thermoelectric case. Thus, we are forced to conclude that the charge-imbalance decay length in the thermopower measurements is not equal to λ_{Q*}, and we must reexamine the assumptions made in the derivation of Eq. (2.11).

The assumption most likely to be invalid is $d^2T/dx^2 = 0$. In the experiment, we establish a uniform temperature gradient along the glass substrate, but when the heat flows into the Al film, it does so over a characteristic length λ_T which results in a nonuniform temperature gradient near the end of the film. The value of λ_T depends on the thermal conductivities of the film and substrate and on the Kapitza resistance between them. To analyze this situation, we will assume that the heat flow in the substrate is not significantly perturbed by the presence of the film. We justify this assumption as follows. We estimate the thermal conductivity of the Al film at T_c from the measured electrical resistivity and the Wiedemann-Franz law to be about 6 W $m^{-1}K^{-1}$. The thermal conductivity of the glass at the same temperature is about[55] 0.03 W $m^{-1}K^{-1}$. Since the ratio of the thicknesses of the substrate and film is at least 3000, the ratio of their thermal conductances (for equal width) is at least 15. We feel justified, therfore, in assuming that the heat flow is quasi-one-dimensional. With this simplification, it can easily be shown that the gradient is given by

$$\frac{dT}{dx} = \frac{dT}{dx}\Big|_{\infty} \quad [1 - \exp(-x/\lambda_T)] \quad , \tag{4.1}$$

where $dT/dx|_{\infty}$ is the gradient far from the end of the film, and

$$\lambda_T = (gd/y_K)^{1/2} \quad . \tag{4.2}$$

In Eq. (4.2), g and d are the thermal conductivity and thickness of the Al film, and y_K is the Kapitza conductance of a unit area between the film and substrate. If we assume d = 3000 Å, g = 6 W $m^{-1}K$, and $y_K = 5 \times 10^3$ $Wm^{-2}K^{-1}$ at T_c,[56] we find λ_T = 20 μm. We note that the characteristic length for the conversion of the phonon current entering the film from the substrate into a quasiparticle current is much smaller than λ_T, and does not enter into our calculation. When Eq. (4.1) is inserted into Eqs. (2.9) and (2.10), one finds

$$V(x) = \frac{\lambda_{Q^*}^2}{\lambda_{Q^*}^2 - \lambda_T^2} (\lambda_{Q^*} e^{-x/\lambda_{Q^*}} - \lambda_T e^{-x/\lambda_T}) S \frac{dT}{dx}\Big|_{\infty} \quad . \tag{4.3}$$

We have fitted Eq. (4.3) to our data using the values of $\lambda_{Q^*}(T)$ from the current-injection experiments, and regarding S and λ_T as adjustable parameters. The resulting best fits are shown in Figs. 14 and 15. We note that the fit is rather sensitive to the value of S, which scales the magnitude of the curves. Given the uncertainties in the data, the fits are very satisfactory. The values of λ_T required to fit the data near T_c, listed in Table I, vary from 14 to 25 μm, in reasonable agreement with our estimated value of 20 μm. However,

in the case of sample 3 the value of λ_T increases from 16 to 25 μm as the temperature is lowered from 0.991 T_c to 0.913 T_c. This increase is higher than one would predict from Eq. (4.2). The thermal conductivity in the superconducting state g is proportional to[4,19,42] $T[1 - (\Delta/k_BT)^3/2\pi^2]$; y_K is expected to scale as T^3. As a result we expect λ_T to scale as T^{-1}, whereas the observed dependence is much stronger than this. We believe the discrepancy reflects the over simplification involved in this model. The values of S obtained from three samples are also listed in Table I. The error bars represent the uncertainties in fitting the data to the model, but do not take into account possible errors due to inadequacies in the model. Within the uncertainties, the values obtained from samples 1 and 2 are in excellent agreement with those obtained from measurements in the normal state. On the other hand, for sample 3 the value of S at the highest temperature is more than 2 times greater than the value of S^N. As we see from Table I the observed values of S appear to increase slightly as the temperature is lowered to 0.9 T_c. Overall, we feel that the agreement between the values of S and S^N is quite acceptable for all three samples, and that our results provide a very convincing demonstration of the ability of the theory to predict thermoelectric effects in superconductors.

It would, of course, be advantageous to study samples in which $d^2T/dx^2 = 0$, but, at least for the sample geometry we have used, this appears to be very difficult. To make λ_T significantly smaller one must either increase y_K substantially, which is impossible, or decrease the film thickness d by a large factor, which would have the

additional effect of reducing l and hence λ_{Q*}. Going to a different substrate material would not help significantly since Al has substantial thermal mismatch to most common materials.[56]

An alternative approach would be the use of a normal-state-superconducting interface, in which a normal-metal film overlaps the end of the Al film so that the heat flow is continuous across the interface, provided the thermal conductances of the films are matched. We attempted this in sample 3, depositing a CuAl film at the same time as the probe deposition which butted up against one end of the Al. Unfortunately, a simple heat flow model predicts such a film does very little good unless the thermal conductance matching is quite precise; in our case we predict that less than 10 percent of the heat flow down the Al film came through the interface. Ideally, we needed a layer of pure Cu of just the right thickness, and a very clean interface; this would have required another photolithographic step. Again, given the inherent difficulty already present in the sample fabrication, we were forced to forego this attempt.

CHAPTER FIVE

SUMMARY

We have clearly demonstrated the existence of a transport current j_N produced by a temperature gradient in superconducting Al films by measuring the charge imbalance near the end of the film where $dj_N/dx \neq 0$. To explain our data, we have had to take into account the fact that d^2T/dx^2 is also nonzero over a thermal healing length λ_T near the end of the sample. Using values of λ_{Q^*} measured in current-injection experiments, we have fitted our data to obtain values of λ_T and S. The values of S for two samples agreed well with the corresponding values of S^N, while the value of S for a third sample was more than a factor of 2 greater than S^N. Given the possible inadequacies in the simple model used, such agreement is quite reasonable.

We have also measured values of λ_{Q^*} from the decay of charge imbalance generated by current injection, and deduced values for τ_E of about 2 ns. This value is within a factor of 2 of that obtained by Stuivinga et al.[51,52] from the charge-imbalance decay length near phase slip centers in Al. Measurements of τ_{Q^*} on the same film using the conventional three-film, two-junction configuration yielded $\tau_E = (11 \pm 3)$ ns. The values of τ_{Q^*} obtained from our decay-length measurements scaled rather accurately with Δ/k_BT, implying that either the inelastic decay rate is enhanced for some unknown reason or that there is an additional unidentified mechanism that also produces a relaxation rate proportional to Δ/k_BT. In either case,

the charge-relaxation rate due to elastic processes over the temperature range studied has been rendered relatively unimportant. We have possibly seen evidence for a new charge imbalance decay mechanism predicted by Lemberger, but we have shown this mechanism cannot explain the discrepancy between the two measurements of τ_E. We emphasize that these discrepancies do not affect the validity of the thermopower results, for which we require only the measured value of λ_{Q^*}.

The field of thermoelectric effects in superconductors has largely been characterized by conflicting results and disagreements with theory. This experiment does not explain the discrepancies in previous attempts to observe the fountain effect; however, it does provide the most convincing demonstration of this effect since it was predicted in 1944. Overall, our results provide a strong experimental verification of the theory of thermoelectric effects in superconductors.

CHAPTER SIX

INTRODUCTION TO THE STM

A. Overview

The remainder of this thesis deals with the development of a Scanning Tunneling Microscope, or STM. This instrument, which operates on the principle of vacuum tunneling, was first developed at IBM Zurich by Binnig, Rohrer, Gerber and Weibel[57]. It represents an exciting advance in the field of surface science, as it can image a surface with 0.1 Å vertical resolution and 2 to 5 Å lateral resolution, where the precise value depends on the definition chosen. This resolution is sufficient to resolve individual atoms.

This report describes our efforts to develop an STM at U.C. Berkeley. Although still under development, it has furnished some preliminary results. Chapter Six describes the background and theory of the STM. Chapter Seven gives details of its construction, with emphasis on those details which differ from the IBM device[58]. Chapter Eight contains a discussion of the limitations of our system due to noise and presents some preliminary results. Chapter Nine contains a concluding summary and some discussion of our future plans for the instrument.

B. Background

The quantum mechanical tunneling of electrons through a potential barrier plays an important role in a variety of physical systems. In 1973 Esaki[59], Giaever[60], and Josephson[61] were awarded the Nobel prize

for work on tunneling. Their work has in turn led to the development of important semiconducting and superconducting devices.

In most conventional tunneling devices the tunneling barrier is formed by an oxide layer 10 to 50 Å thick at the interface of two conductors. One problem with this technique is that its use is limited to those materials which readily form oxides[62]. Moreover, the properties of the oxide itself, such as its resistivity and defect density, and the presence of electronic states in the barrier, can lead to non-ideal behavior which is often difficult to predict or control.

In many ways, a vacuum gap is the ideal tunneling barrier: it is well-characterized, independent of the materials used, and the barrier width can be altered in a well-controlled manner. Recently, a number of attempts have been made to observe tunneling through a controllable vacuum gap [63-66]. One of the more successful was that of Teague[66], who varied the spacing between flat Au electrodes using piezoelectric ceramics. He found the tunneling current varied exponentially with the electrode spacing, in agreement with the theory of Lang and Kohn[67].

In 1972, Young and co-workers attempted to construct a surface microscope based on the principle of vacuum tunneling[68]. Their apparatus, like the STM, used a tip to scan along a surface. Because of mechanical vibrations, their microscope did not function in the vacuum tunneling regime, although they did observe vacuum tunneling with a simplified apparatus which did not scan the tip. The actual microscope did function in the less sensitive field-emission regime, with vertical resolution of 30 Å and lateral resolution of 1000 Å.

In 1982, Binnig, Rohrer, Gerber, and Weibel published a description of the first STM[57]. Its operation is quite straightforward in principle. A sharp metal tip is brought close to the surface under study and a small voltage (typically ~1 mV) is applied between tip and sample. Provided the tip is close enough to the sample, typically within 10 Å, electrons will tunnel quantum-mechanically across the vacuum gap. Because the electronic wavefunctions decay exponentially into the vacuum, the current which flows in the tunneling regime will be an extremely sensitive function of the spacing between tip and surface. This process is to be contrasted to that of field emission, in which the applied voltage is great enough that the electrons can exist as free particles in the vacuum. In field emission, the current is relatively insensitive to the tip-to-surface spacing.

In the STM, the tip is attached to three piezoelectric drives, which allow the tip to be moved both in the plane of, and perpendicular to, the surface. As the tip is scanned along the surface, changes in surface topography will cause changes in tunneling current. In actual operation, the tip is controlled by a servo loop which adjusts the tip-to-surface spacing so as to keep the current constant. In this way, the feedback signal reflects the topograph of the surface, as illustrated in Fig. 17.

The scanning tips are 1 mm tungsten rods sharpened on a grinding wheel at 45°. It is remarkable that such tips can routinely give lateral resolution of 20 to 30 Å. This resolution is a consequence of the properties of vacuum tunneling, which are discussed in the following section.

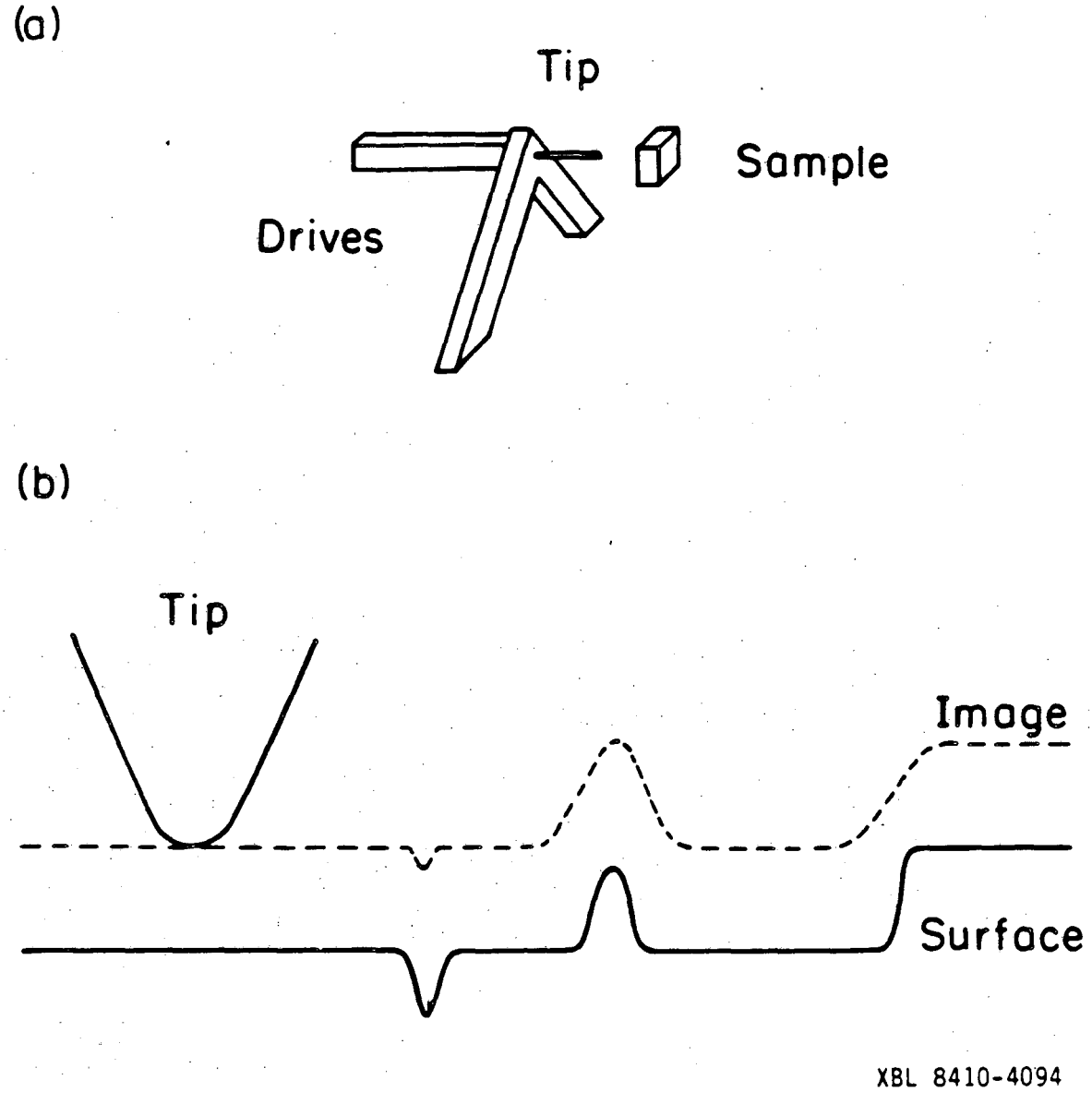

Fig. 17. The three orthogonal piezoelectric drives with the tip attached are shown in (a). In (b), an image of the surface is produced by scanning the tip laterally while keeping the distance to the surface fixed. The lateral resolution is a function of the surface topography and the tip size.

C. Theory

To first approximation, the vacuum tunneling characteristics can be derived from the WKB approximation, as used by Simmons in his treatment of thin-film metal-insulator-metal junctions[69]. Consider the tunnel junction represented in Fig. 18, with the current flowing from left to right. Assuming that the barrier is approximated by the simple one shown, then in the limit $eV << k_BT$, the current density J is given by

$$J = J_o \left[\phi e^{-A\phi^{1/2}s} - (\phi + eV)\, e^{-A(\phi + eV)^{1/2}s} \right] \quad . \tag{6.1}$$

Here s is the barrier width, ϕ is the arithmetic mean of the work functions of the two electrodes, and $A = 4\pi(2m)^{1/2}/h \simeq 1/eV^{1/2}\text{Å}$. Taking the limit $eV << \phi$, and multiplying by an effective tip cross-sectional area C, we find

$$I = I_o \frac{C}{s} \phi^{1/2}\, Ve^{-A\phi^{1/2}s} \quad . \tag{6.2}$$

Here $I_o = (2m)^{1/2}(e/h)^2 = 3.2 \times 10^{-6}$ A/(Å$eV^{1/2}$V). The junction is thus ohmic for $eV << \phi$, with resistance exponentially dependent on barrier width. (At larger voltages, a correction term of order V^3 becomes significant). Taking ϕ = 3 eV, s = 6 Å, and C = 1000 Å^2, say, Eq. (6.2) predicts a gap resistance of roughly $6 \times 10^7 \Omega$. For this case, the current density with V = 1 mV is 160 A/cm^2. Note that this treatment neglects thermal activation of electrons over the barrier. This

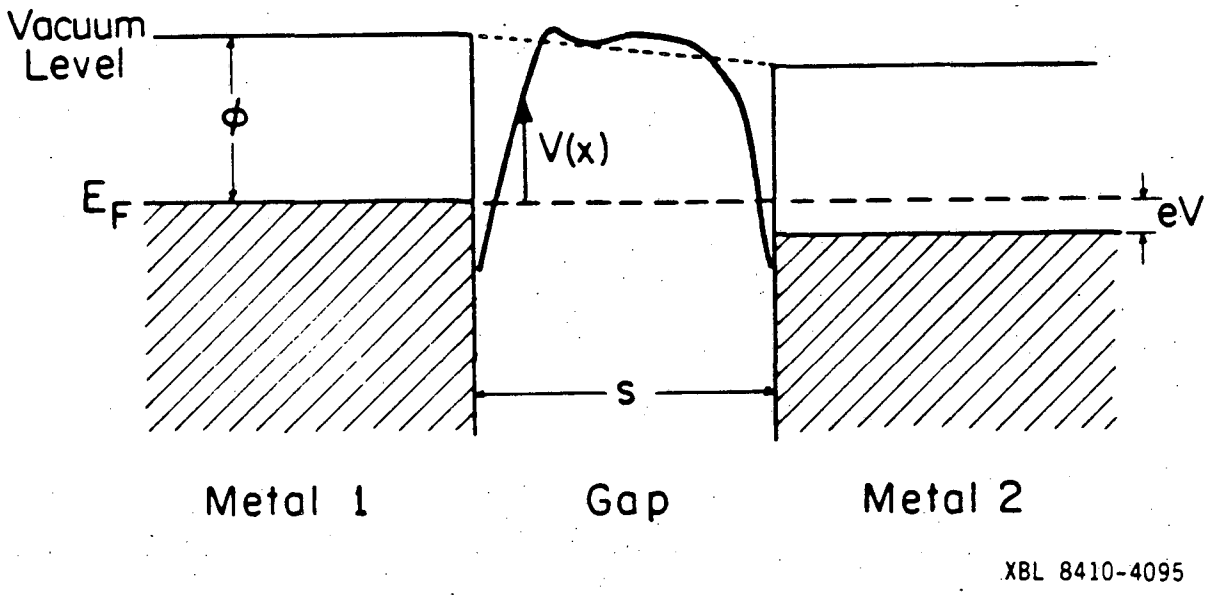

Fig. 18. (After Simmons[69]) Energy levels and potential barrier for tunneling between two metals separated by an insulating barrier. The bold curve in the gap represents the actual potential barrier, and the dotted line is the approximate potential barrier.

is reasonable, since for most metals ϕ is typically 3 to 5 eV, much larger than $k_B T$, which is 0.025 eV at room temperature.

For a work function of 5 eV, Eq. (6.2) predicts a change in resistance of roughly one decade for 1 Å change in s. This strong dependence on spacing gives the STM its high vertical resolution.

A number of theories which take into account the three-dimensional geometry of the tip have been proposed in order to explain the high lateral resolution of the STM[70-72]. Tersoff and Hamann[70] have suggested that the local radius of curvature R of the tip limits the lateral resolution ξ to $\xi = [(R + s)/(A\phi^{1/2})]^{1/2}$; here s is the distance of nearest approach between tip and sample, and $A\,\phi^{1/2}$ is the inverse electronic decay length into the vacuum. Because that portion of the tip closest to the sample dominates the tunneling process due to the exponential dependence of Eq. (6.2), R may be quite different from the global radius of curvature, for instance because of a small protrusion on the end of the tip. Fitting to results of Binning and Rohrer[73] exhibiting 5 Å resolution, Tersoff and Hamann inferred a tip radius of R = 6 Å. For the ~30 Å resolution more commonly obtained, one would expect R = 400 Å.

Theories such as that of Tersoff *et al.* are not complete theories of the STM, as they do not account fully for many-body effects. Electrons interact with each other via the coulomb interaction and the Pauli exclusion principle. A theory which correctly accounts for these exchange and correlation effects, such as that for the metal surface developed by Lang and Kohn[67], has yet to be worked out for the STM.

D. Applications

Granted that a complete theory of the STM has yet to be developed, some impressive capabilities have been convincingly demonstrated. To understand the potential value of the STM, one must consider problems in the study of surfaces and some of the other techniques available.

The surface structure of a crystal is more complicated than the bulk structure because of the loss of periodicity at the surface. Because the surface atoms are lacking neighbors on one side, the bulk structure may no longer be the lowest energy configuration at the surface, and the surface atoms may physically shift into another configuration. When the surface plane of atoms moves uniformly away from the bulk, the process is known as relaxation; when the surface atoms rearrange themselves within the plane it is known as reconstruction. Reconstructions can change the periodicity of the surface. A wide variety of reconstructions are known to occur in nature. The determination of their structure is an active field of study for surface scientists.

The study of adsorbates on surfaces is also of great fundamental as well as technological interest. Knowledge of where adsorbates bond, and in what orientation, is very important in the field of catalysis, as the catalyst's function is usually to provide a substrate onto which the reacting species can adsorb. One such catalyst is platinum, which greatly increases the rate of certain hydrocarbon reactions in the catalytic converter in an automobile.

Clearly, a technique such as STM, which probes surfaces and has atomic resolution, is valuable for studying such systems. Other

available techniques give useful but somewhat different information. Low Energy Electron Diffraction, (LEED), for example, is a standard technique in which electrons with energy ~100 eV impinge on a surface. Such electrons have wavelengths of the order of an atomic spacing, and thus are diffracted at the surface. The resulting diffraction pattern is quite sensitive to the periodic structure at the surface. However, LEED information is incomplete, as phase information is lost, and it is quite difficult to transform the LEED pattern into an unambiguous real-space structure, particularly when the unit cell contains many atoms. Furthermore, LEED patterns give information which is averaged over some fairly large area, which is not always desirable. For example, a surface which is ordered only in some small region may give a LEED pattern which is nearly indistinguishable from that due to a totally ordered surface. Another useful technique is that of Scanning Auger Microscopy. It does not provide structural information, but it does give information as to the type of adsorbates on a surface with ~200 Å resolution. Transmission Electron Microscopy can now give real-space images with atomic resolution laterally, but the vertical resolution is of the order of 100 Å. Such images are therefore averages over many planes of atoms. Some surface information can be obtained by looking at surfaces edge-on[74], but in most cases the information is still incomplete. None of these techniques gives exactly the same information as does the STM.

STM has the advantages that it gives a real-space image, unlike LEED, and probes just surface atoms, unlike TEM. In addition, it

gives local information, and is potentially useful for imagining aperiodic structures. Finally, STM has the exciting potential, as yet only partially realized, of allowing local work function measurements. By modulating the tip position and lock-in detecting the current, one can make a local map of work function. One can thereby distinguish between different atomic species at a surface, with demonstrated resolution of ~50 Å[58].

STM does not replace other surface science techniques but works best in conjunction with them. The STM has the limitation that the information it gives is quite local: so far the STM has been limited to imagining areas a few thousand Å on a side. Sometimes a more global view is desired; in such cases techniques which give more averaged information would be more useful. Moreover, the STM does not give strictly topographical information; it gives lines of equal electron density (and work function); such information by itself may be non-trivial to interpret. The STM can supply information which can not be obtained in any other way, but the information may not be complete. As such the STM provides a valuable complement to the wide variety of other available surface tools.

CHAPTER SEVEN

CONSTRUCTION

In this chapter we discuss the construction of the Berkeley STM. The important components necessary for operation of an STM are: (1) a vibration isolation system, (2) a relatively coarse position controller, in our case a walker, (3) the piezoelectric scanning drives, (4) the servo feedback electronics, and (5) a computer which in our case controls the experiment. In addition, (6) some sort of vacuum system is needed; in our case this is a standard stainless steel UHV system.

A. Vibration Isolation System

Clearly, if the tip-to-sample distance is to be held fixed at 10 Å to within 1%, it is necessary to isolate the microscope from external vibrations. We have constructed our microscope in the sub-basement of our laboratory, which rests on bedrock, to minimize vibrations at the outset. The background level of vibration of the floor,[75] along with the vibrations generated by people and equipment in the laboratory, will still be much greater than the microscope can tolerate, so that good vibration isolation is needed. We followed the approach of Binning and Rohrer and assembled a vibration isolation system inside the vacuum chamber. The system is a two-stage low-pass filter built up from three concentric stainless-steel rings. A photo is shown in Fig. 19. The outermost ring is bolted directly to the vacuum system, and the inner two are suspended from springs. Samarium-cobalt magnets and copper blocks provide eddy-current damping as the magnets move

Fig. 19. Photo of author with the Berkeley STM. The microscope rests on top of a two-stage vibration isolation system which uses springs for isolation and copper blocks and magnets for eddy-current damping.

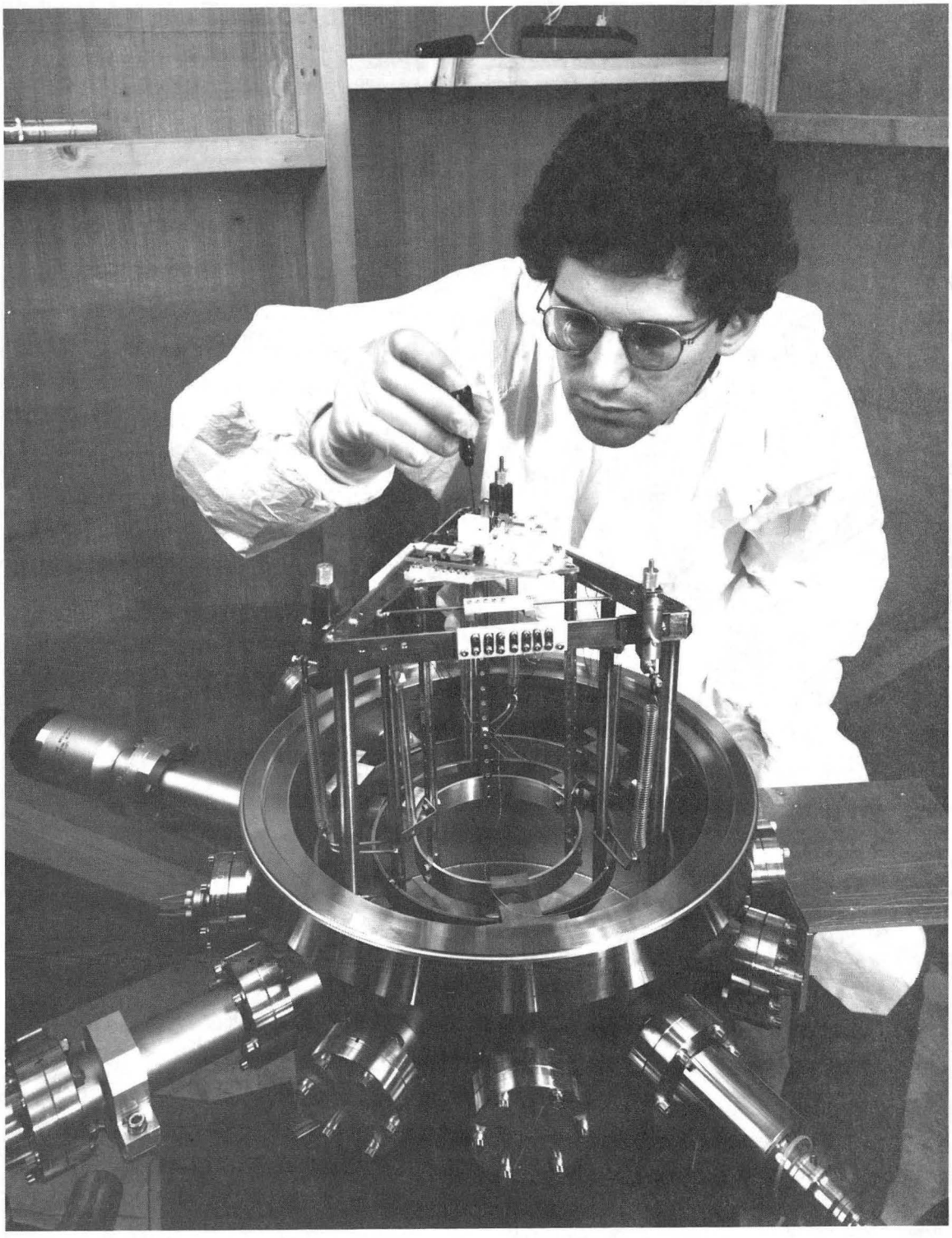

CBB 848-6133

relative to the blocks. This provides a velocity-dependent damping force which depends on the strength of the magnets, the conductivity of the copper, and the geometry.

We have attempted to make the resonant frequencies of the system as low as possible for optimum high frequency performance. It is useful to keep in mind that the lowest possible resonant frequency of the system is, to first approximation, determined solely by its geometry. A simple example makes this clear: a mass m, placed on a spring of unextended length ℓ_0 and spring constant k, in a gravitational field g extends the spring a length ℓ, where $mg = k(\ell - \ell_0)$. The resonant frequency is given by $\omega = (k/m)^{1/2} = [g/(\ell - \ell_0)]^{1/2}$. For soft springs and large mass, $\ell >> \ell_0$, so $\omega \simeq (g/\ell)^{1/2}$, which is also the resonant frequency of a pendulum of length ℓ. In our case ℓ is constrained to be less than 0.3 m to fit in the UHV system, so ν will always be greater than 1 Hz. The resonant frequency of the inner stage, deduced from $\omega = [g/(\ell - \ell_0)]^{1/2}/2\pi$, is 2.4 ± 0. 1 Hz. The resonant frequency of the outer stage when it is not loaded by the inner stage is estimated at 2.8 ± 0.2 Hz.

The frequency response also depends on the amount of damping present. To achieve maximum damping acceleration for a given damping force we have made the system as light as possible. The quality factor Q of each stage is roughly 3 ± 1.

In order to make quantitative estimates for frequency response for our system, we have modeled it by the two coupled oscillators shown in Fig. 20(a). Damping terms of the form $\gamma\dot{x}$ were included, where $\dot{x}$ is

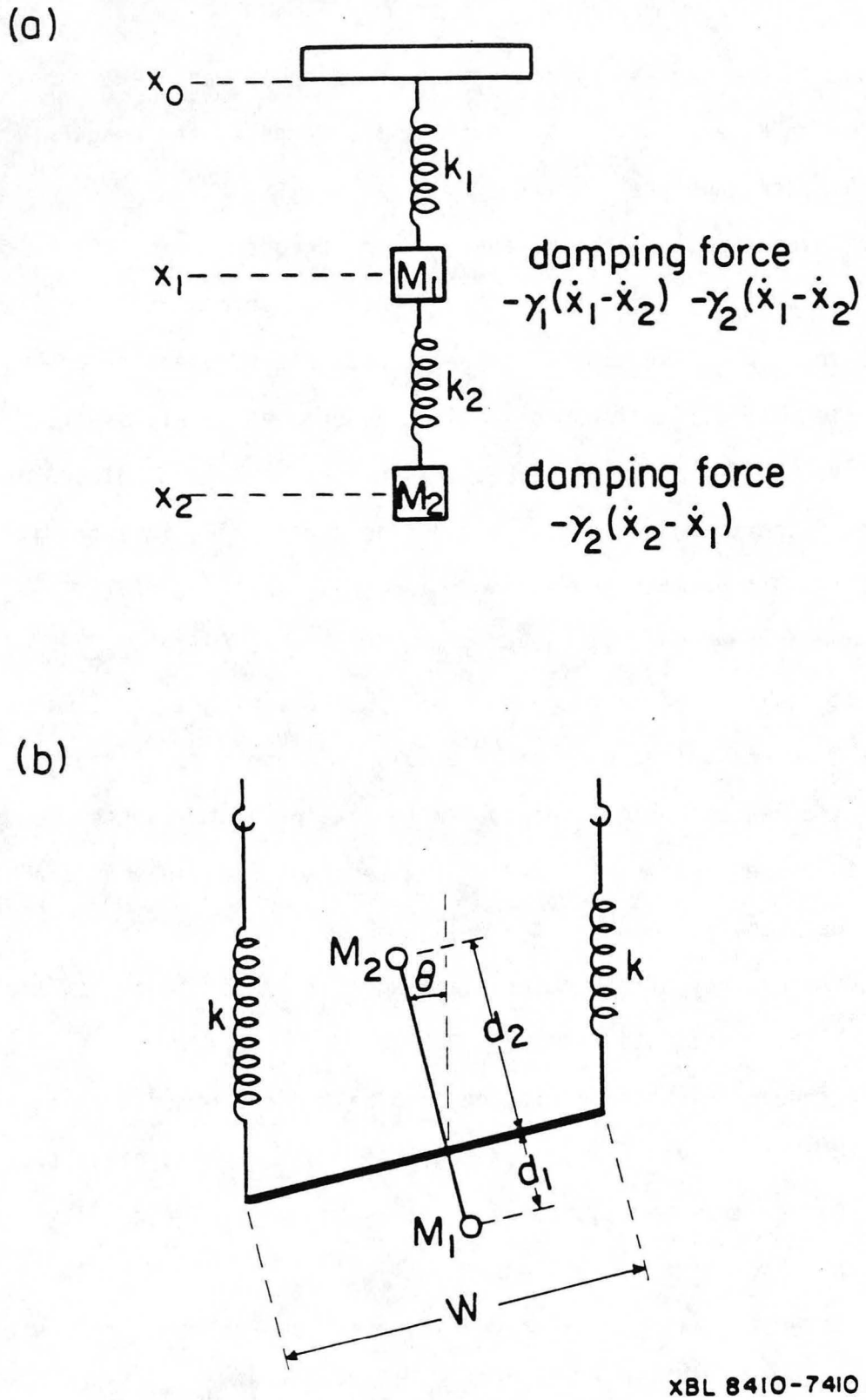

XBL 8410-7410

Fig. 20. (a) Simple model used in calculating the vibration system response. The damping terms differ for M_1 and M_2, corresponding to the actual arrangement of the copper blocks and magnets. (b) Model used in estimating stability of innermost stage. For motion in the plane, system is stable provided $kW^2 > M_2d_2 - M_1d_1$.

the appropriate relative velocity. We used the above parameters for resonant frequencies and damping and calculated the expected actual response; this is plotted in Fig. 21. This plot also shows the effect of decreasing the damping. Interestingly, increased damping gives better low-frequency response but less attenuation at high frequencies. The reason is that with greater damping the stages are coupled together more closely; the energetic cost of having one stage move relative to the other is greater. Using the parameters measured for our system, the model predicts the following response: amplitude gain of ~7 at 1.7 Hz (17 ± 5 dB in energy), gain of $\sim 1.4 \times 10^{-4}$ at 60 Hz (-77 ± 5 dB), and gain of $\sim 4.9 \times 10^{-7}$ at 1000 Hz (-126 ± 7 dB).

This model is an oversimplification of the actual spring system; high frequency vibrations can be transmitted down the springs much more effectively than this simple one-dimensional model predicts. The springs themselves are made of wires which can support high frequency vibrations. To damp these out, we have suspended the springs from Viton O-rings. Although the current system is somewhat sensitive to acoustic noise, as will be discussed in Chapter Eight, an earlier version without Viton was substantially more sensitive to such noise.

A similar problem is that high frequency vibrations can be transmitted down the wires used to make electrical connections to the inner stage. To minimize this effect we have used wires ~100 μm in diameter, the smallest size which can be conveniently insulated with UHV-compatible insulation. The wires are clamped down at each stage of the isolation system.

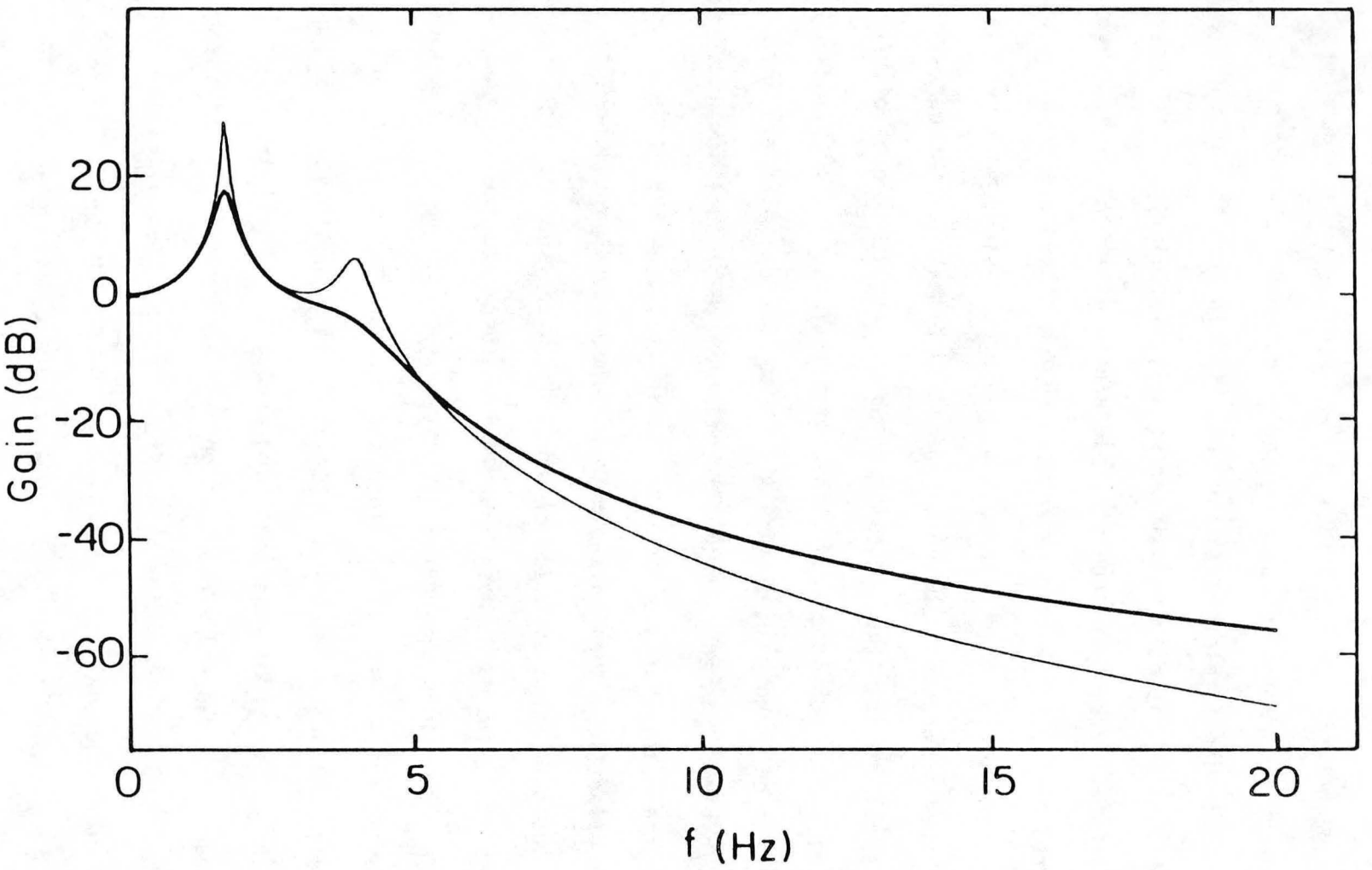

XBL 8410-4093

Fig. 21. Calculated response of the spring system shown in Fig. 20(a). The bold curve is the expected response determined from the actual parameters (frequency and Q) estimated for our system. The other curve shows for comparison the expected response with one-fourth the damping.

One way in which our vibration system differed significantly from the IBM design (and most others) is that the microscope sits on a stage held above the plane of the rings and magnets. This arrangement provides easy access to the sample, as seen in Fig. 19, but it also introduces some serious problems. First is that of stability: the high center of mass makes the stage prone to tipping over. One can derive the stability criterion for the simple model shown in Fig. 20(b). Assuming massless springs and bars and motion confined to a plane, the arrangement is stable provided $kW^2/g > M_2 d_2 - M_1 d_1$. Here k is the spring constant of each spring, and the dimensions and masses are as shown. Because of the large moment arm d_2, an increase in M_2 has a large effect on the stability. To enhance stability we made W as large as our geometry allowed.

This large moment arm also gives rise to a rocking mode. In this mode, the motion at the top of the stage, where the microscope sits, is much greater than the motion at the bottom, where the copper blocks are located. This mode is therefore not very well damped; its observed Q is 6 ± 2. Furthermore, unless the system is perfectly symmetric, any vertical motion which is not damped out will eventually couple into this rocking mode. An improved vibration isolation system is under construction which will be lighter to improve its damping, and more symmetric to inhibit the rocking motion.

Finally, as is clear from Fig. 21, this system does not attenuate low frequencies; in fact, certain frequencies are amplified. As long as the microscope is assembled rigidly, such vibrations will not lead

to any relative motion between pieces. To this end we have assembled the microscope on a solid quartz substrate clamped to the vibration stage, and clamped the individual components together whenever possible.

B. Walker Fabrication and Performance

The piezoelectric drives which move the tip have a range of several thousand Å. A coarse control which has a much larger range is also needed, since in the initial setup the tip and sample will be separated by macroscopic distances. Because of the need to isolate the microscope from vibrations, a mechanical arrangement operated from outside the vacuum chamber, such as a differential screw, is impractical. Some sort of light and compact UHV-compatible motor is necessary. The IBM group developed a type of piezoelectric walker which they dubbed a "louse". Our walker is based on the same principle, but has been simplified considerably.

The walkers are made of PZT, a commercially available piezoelectric ceramic which we use for all of our electromechanical devices. PZT is a lead-titanate/lead-zirconate based material and has a relatively high mechanical extension for a given applied electric field. A voltage applied along the axis of polarity of the material causes the material to shrink along that axis. The material must then expand in the orthogonal directions, to an extent which depends on the geometry and Poisson's ratio. For our geometries this orthogonal motion is ~10 Å/V.

The walker is basically a flat slab of PZT which can be made to expand or contract lengthwise by applying a voltage between top and

bottom. Our walkers have feet at each end which can be clamped capacitively to a substrate. By clamping and unclamping the feet and simultaneously stretching the body in the correct sequence, the walker can take steps either forward or backward (see Fig. 22).

We fabricated our walker as follows: we first cut a rectangle, roughly 12 mm x 40 mm, out of a slab of PZT. The PZT was supplied metallized and poled in thicknesses of 0.1" and 0.2". We cut out a channel roughly 1 mm deep on the bottom, leaving two regions, one at each end, to form the feet. We then polished the feet by hand, using polishing paper with 6 μm grit. We polished the feet until interference rings were visible on both feet when the walker was pressed against a piece of optically flat quartz. This check assured the feet were flat both locally and globally. After polishing, the bottom of the walker was metallized with approximately 4000 Å of evaporated Al. This was followed by 50 Å of Cr and then 3000-4000 Å of SiO. The Cr improves adhesion of the SiO, which acts as an insulator. We have extended this technique to make walkers that can move in two dimensions, using an L-shaped piece of PZT with each side 12 mm x 40 mm.

The walker moves on an optically flat quartz substrate. An L-shaped walker with sample mount is shown on the quartz substrate in Fig. 23. This quartz substrate was also metallized and coated in the same manner as the walkers. The metal films on feet and substrate separated by the SiO layer act as a capacitor. An applied voltage across this capacitor creates an attractive force that clamps the feet to the substrate.

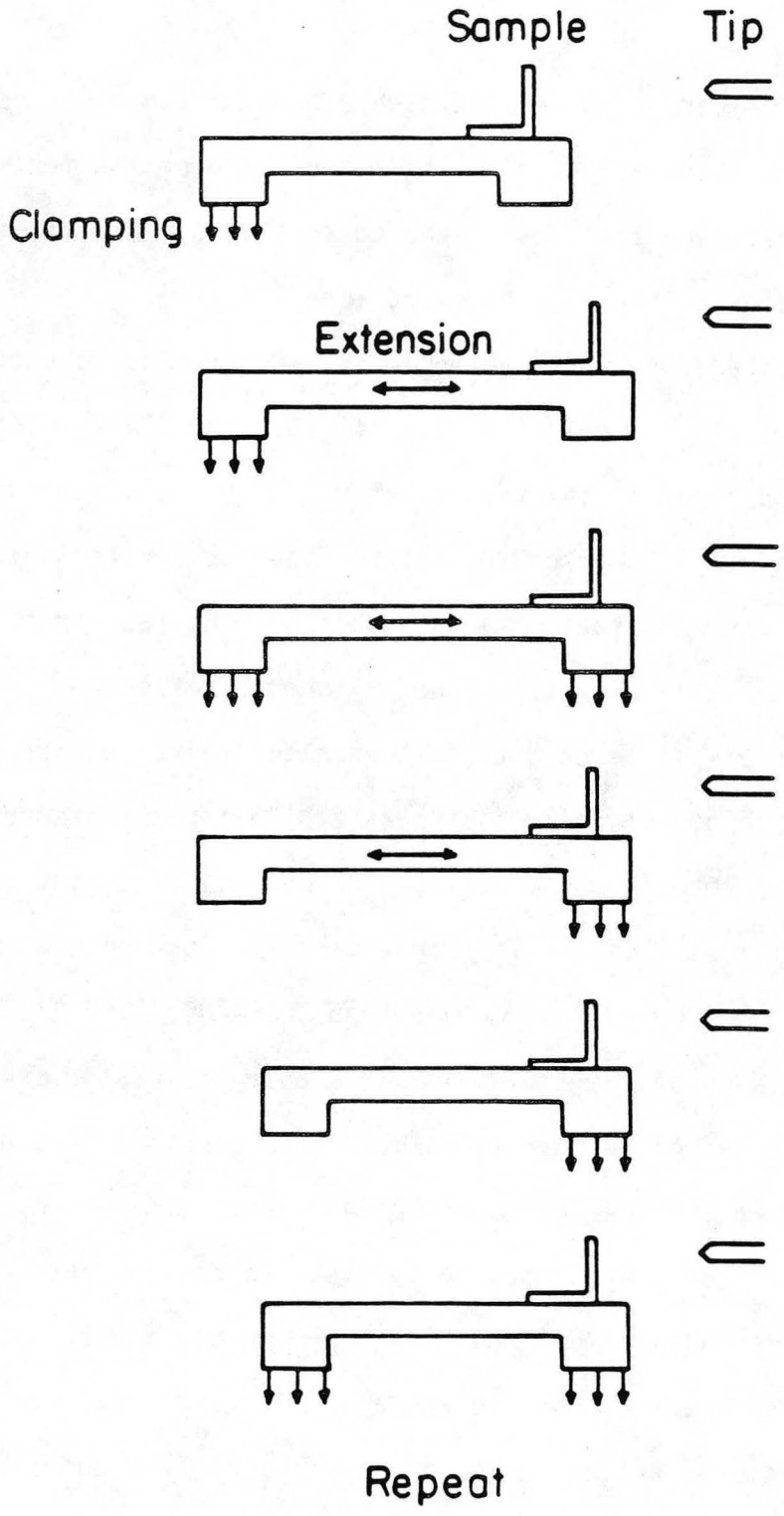

Fig. 22. Sequence of applied voltages to move the walker to the right. A reversed sequence moves it to the left.

Fig. 23. Photo of walker with sample (left) and the X-, Y-, and Z-drives and mount (right). These sit on an optically polished quartz substrate, part of which has been metallized. A MaCor sample mount is bolted to the walker. Electrical contact is made to the walker with stainless steel clamps, and to the drives with indium pads.

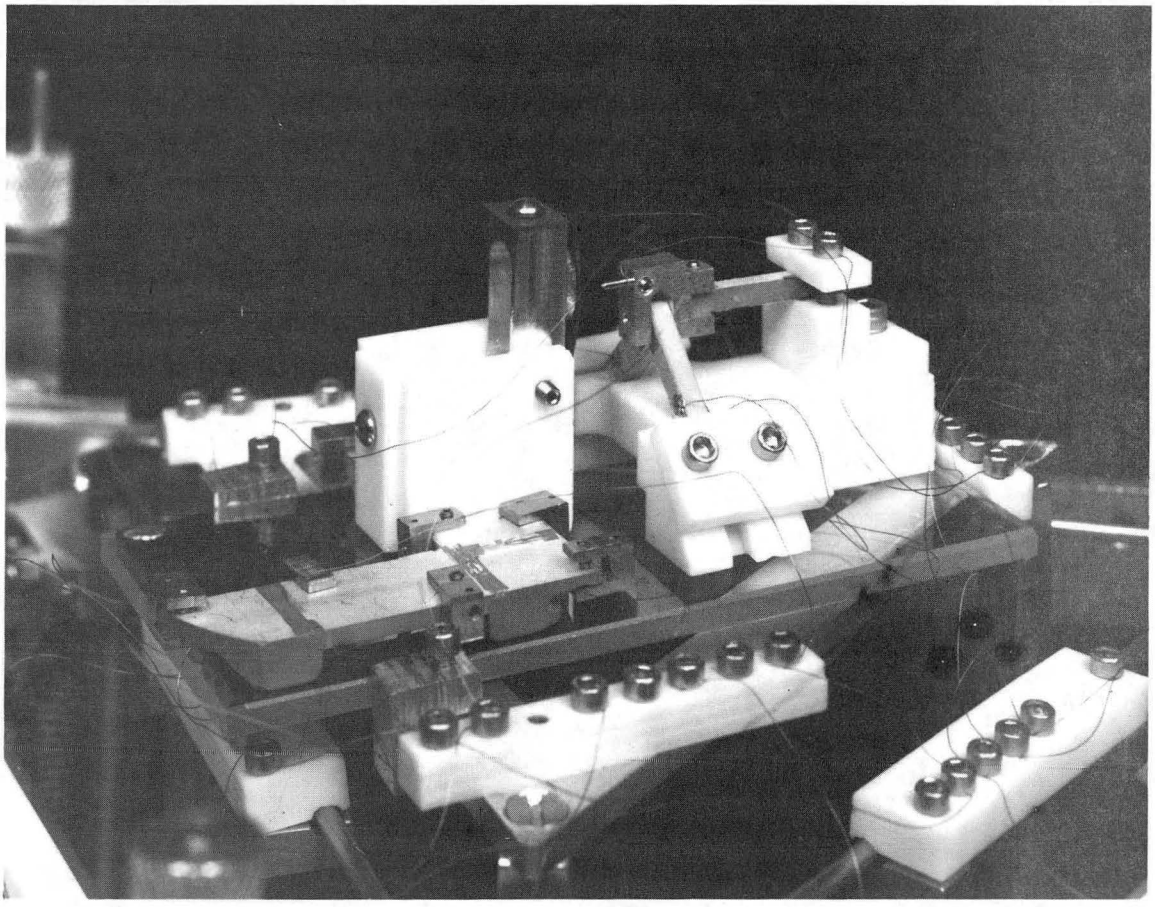

CBB 848-6137

Our walkers differ considerably from the IBM louse, which utilizes polished slices of $SrTiO_3$ as a dielectric layer. An SiO thin film has a much lower dielectric constant, but can be made much thinner, and so larger capacitances can be achieved. This allows us to use a relatively small clamping voltage of 60 V (in comparison with the hundreds of volts[76] necessary with $SrTiO_3$). The IBM louse also required ball bearings under the feet to allow them to pivot and so track a substrate that is not flat. We avoid this problem by ensuring that the feet and substrate are both optically flat. This technique makes walker fabrication quite simple, requiring roughly a day's work.

The motion of the walker is controlled by a DEC LSI 11/23 computer. The computer generates 5 V square waves in the correct sequence. These square waves are fed into high voltage FET switches. The sequence of six pulses produce the motion shown in Fig. 22. The extension and clamping voltages are set by high voltage power supplies.

We checked the motion of the one-dimensional walkers by observing them under an optical microscope at 80X. Under the microscope, we observed a walker move as quickly as 40 μm/s. This speed was with the extension voltage at 300 V and walker taking 100 steps/s. We have run the walkers at speeds up to 300 steps/s. The observed motion in 1000 steps vs extension voltage is shown for two different walkers in Fig. 24. In both cases the average step size increased linearly with incremental voltage with a slope of 20 to 25 Å/V, in good agreement with the 30 Å/V predicted from the geometry and properties of the PZT. One of these walkers, however, required roughly 200 V extension voltage to overcome some barrier and begin moving.

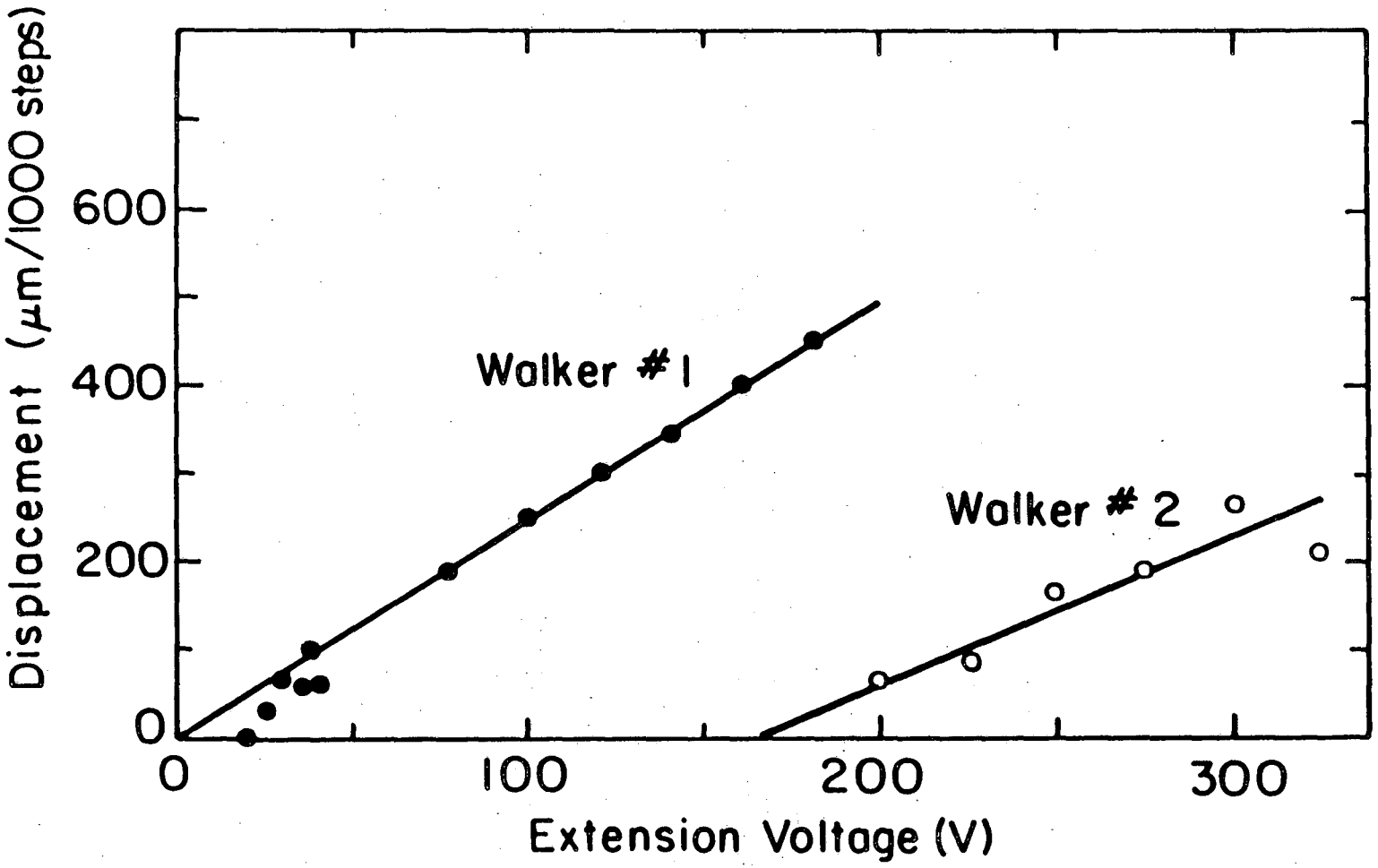

XBL 8410-4091

Fig. 24. Motion of two similar walkers as a function of applied extension voltage. The step size increased by roughly 25 Å/V for each walker, although for walker #2 no motion was observed below 200 V.

We further checked the motion by using the walkers to push a mirror which formed one side of an interferometer. In this way we were able to see that clamping a foot caused a motion or roughly 200 Å. This motion is probably due to the feet not being absolutely parallel, so that clamping one foot rocks the walker very slightly. This explanation is supported by the fact that the measured capacitance of the foot to substrate is 150 pF, which implies a gap of 5 μm, much greater than the 8000 Å thickness of the two SiO films.

The walkers are fairly reliable provided they are operated under suitable conditions. Dust and local irregularities on the substrate can cause a walker to slow down or stop altogether; the performance of the walkers improved substantially when we started to test them under a laminar flow hood. In addition, the walkers become less reliable when carrying additional mass. The two-dimensional walker shown in Fig. 23 was rather unreliable when carrying the sample and mount pictured, but became considerably more reliable when the mount was replaced by a lighter one. With the lighter load, this walker was able to move the sample forward and backward in vacuum in roughly 300 Å steps over a distance of 1 mm.

Often these walkers only walk in one direction. However, we found that they can be made to walk in the opposite direction by reversing the polarity of the extension voltage. We believe the problem occurs when only one foot is clamping, since adding weight on top of the other foot can sometimes correct the problem. It has been shown that by having an asymmetric mass distribution on a walker, it can be made

to hop without clamping the feet[77]. It is possible that this hopping mechanism is partially responsible for motion of our walkers.

In sum, the walker technology has basically worked. Our walkers have brought the sample into the range of the fine control (Z-drive) so that tunneling could be observed and scans taken. Because of thermal drifts, this coarse adjustment is sometimes necessary several times a day while taking data. With the two-dimensional walker, we have been able to move the sample sideways, although it sometimes crashes or moves out of range. In conclusion, we have designed and built a simple walker, which provides the coarse control necessary to the operation of the STM.

C. Fine Positioning Control

The heart of the STM is the scanning tip along with the piezoelectric drives which control tip position. The X- and Y- drives scan the tip along the sample parallel to its surface. The Z-drive moves the tip perpendicular to the surface to keep the tip-to-surface current constant while scanning.

The present XYZ-drives and mount are shown in Fig. 23. The design of the drives follows that of Binning and Rohrer. As suggested by Golovchenko[78], the mount is made of MaCor, a machineable ceramic made by Corning which is UHV compatible. The drives are 2.5 mm square in cross-section, and are roughly 10 mm long. The X- and Y- drives are shaped out of a single V-shaped piece of PZT. The Z-drive is a separate piece of PZT. The X-, Y- and Z- drives are joined by an aluminum

holder and are held firmly together with set screws. The metallization has been scraped off that part of the PZT in contact with the aluminum so that the drives are electrically isolated from the aluminum and each other. The aluminum piece also holds the tip, which is a 1 mm diameter tungsten rod which has been ground to a point on one end. The entire assembly is then tightly clamped into the MaCor mount. This forms a highly rigid structure, with no observable slipping of the drives during operation.

The length chosen for the drives is determined by the trade-off between dynamic range and frequency response. A longer drive extends more for a given voltage but also resonates at a lower frequency. The mechanical resonance of the Z-drive limits the gain and frequency response of the controlling feedback loop, since if the feedback gain is greater than one at the resonant frequency of the drive, the system will oscillate. The lowest natural resonant frequency for transverse vibrations in a free-standing beam is given by[79]

$$f = 0.16 \frac{T}{L^2} \left(\frac{\gamma}{\rho}\right)^{1/2} \text{ Hz} \quad , \tag{7.1}$$

where T is the thickness, L the length, γ the modulus of elasticity, and ρ the density, all in MKS units. Using the values[80] $\gamma = 6.1 \times 10^{10}$ Nt/m^2, $\rho = 7500$ Kg/m^3, $T = 2.5 \times 10^{-3}$ m, and $L = 2.0 \times 10^{-2}$ m, the expression predicts f = 3 kHz, in fair agreement with the roughly 2 kHz we observed in our original 20 mm drives. Shortening the drives by a factor of two increased the

resonant frequency by roughly a factor of four, as predicted, to ~8 kHz.

We calibrated the extension of the 10 mm drives with an interferometer and found 15 ± 1.5 Å/V for the X- and Y- drives and 10 ± 1.5 Å/V for the Z-drive. We have assumed the extension is linear in the applied voltage. For a 0 to 300 V applied voltage, we thus have a 4500 Å range in X and Y and a 3000 Å range in Z. As our high voltage amplifiers handle 300 V, we are limited to imaging areas several thousand Å on a side. We also have used the interferometer to find out whether moving the X- or Y- drives caused any motion in the Z-direction. We verified that the transverse motion was less than 10% of the longitudinal motion.

Ideally, one would like large X- and Y- drives for large scanning range and a short Z-drive for fast frequency response. If the drives are physically connected, however, motion in the Z-drive may still excite lower frequency modes in the X- and Y- drives, as some coupling is inevitable, particularly since the PZT has a Q of ~60.[80] To bypass this problem, one must physically separate the drives. We are currently exploring possibilities such as building the Z-drive on the walker and placing the sample on the X- and Y- drives.

D. Feedback Electronics

As the tip is scanned over the surface under study, an electronic control loop adjusts the vertical position of the tip to keep the tip-to-surface current constant, as in Fig. 17. This scheme allows

the topography of the surface to be mapped out; the feedback voltage applied to the Z-drive reflects the topography and is taken as the signal out of the microscope.

A simplified schematic of the feedback electronics is shown in Fig. 25. The basic components are a voltage bias for the tip-to-sample resistance, a current-to-voltage preamplifier, a logarithmic-amplifier, an integrator, and several amplification stages including a high voltage amplifier.

The voltage bias is set by a mercury battery used with a resistor divider network. We typically bias at 1 to 10 mV, and can reverse the bias polarity.

For the current-to-voltage preamplifier we use a Burr-Brown 3528 low-noise FET input op-amp with a 10MΩ resistor in feedback. The combination of a few pF stray capacitance of the input leads and the large feedback resistor limits the frequency response of this stage to roughly 30 kHz. To improve performance it will be necessary to limit lead length by placing the preamplifier inside the vacuum chamber, as is currently done by the Stanford group[81].

The output of the preamplifier is rectified and fed into the logarithmic-amplifier, which linearizes the exponential dependence of the tunneling current. Previous workers[82] have found this stage necessary.

The purpose of the integrator is to reduce the loop gain at high frequencies. Other stages will introduce phase shifts at high frequencies; if the loop gain is greater than one when the phase shifts accumulate to ~180°, the feedback is positive and the system will

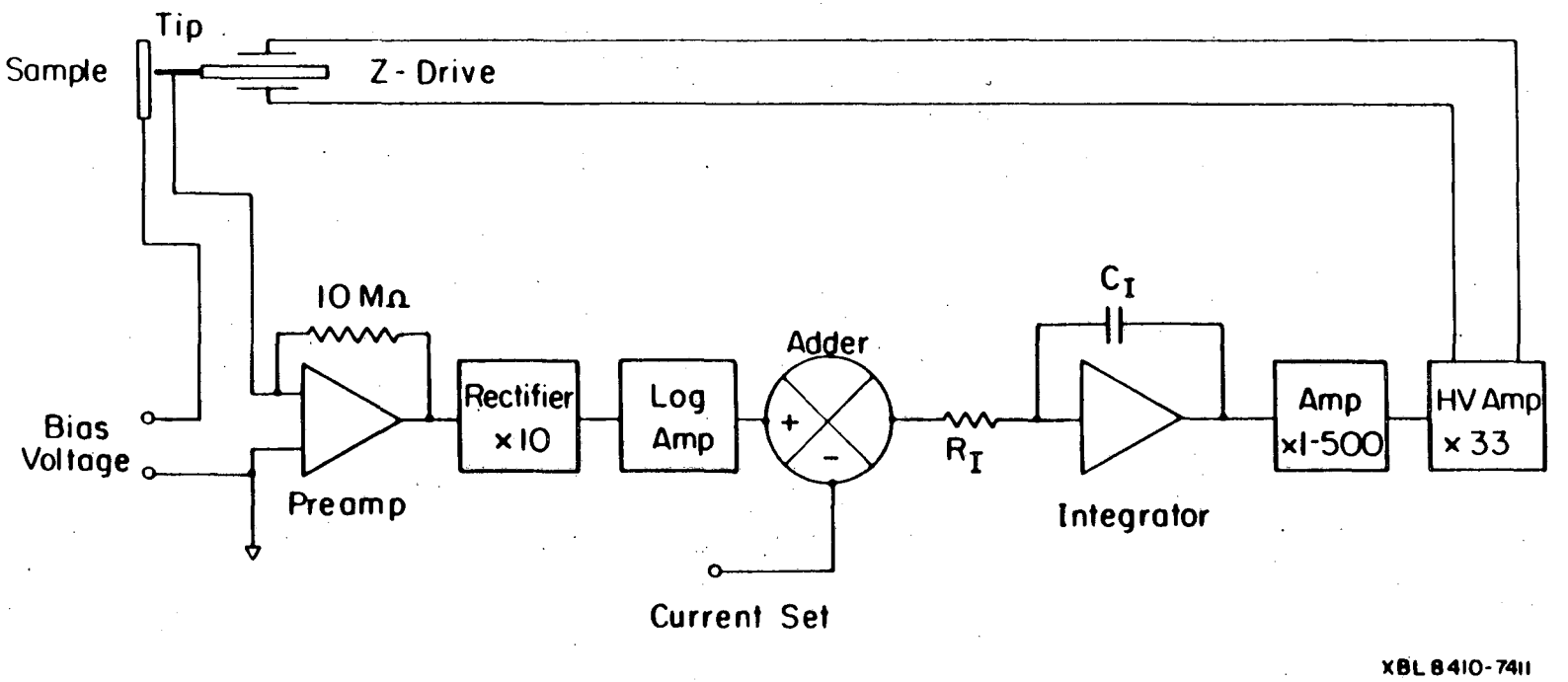

Fig. 25. Schematic of feedback electronics.

oscillate. It is straightforward to show that for an integrator with time constant RC in a feedback loop of gain G, the feedback voltage as a function of frequency is given by:

$$\frac{V_f(\omega)}{V_f(0)} = \frac{1}{1 + j\omega RC/G} \quad . \tag{7.2}$$

Thus, the integrator pole is effectively shifted from $\omega = 1/RC$ to G/RC. We operate with $R = 1\ M\Omega$ and $C = 0.1\ \mu F$, which gives a time constant of 0.1 s. We can operate with a gain G of up to about 600, so that the 3 dB point of the feedback loop is roughly 1 kHz. This best-case response is shown in Fig. 26; we usually operate with a bandwidth of several hundred Hz. As G is increased, the feedback signal becomes increasingly noisy. When G becomes too large, the system oscillates at 7-8 kHz, which is the mechanical resonant frequency of the Z-drive.

The final electronics stage is the high-voltage amplifier. Due to the difficulty in making a fast amplifier which will also swing large voltages, we split the high voltage stage into two parts: a slow stage which swings high voltages but only handles the low frequency part of the signal, and a fast stage with a 30 V range for the high frequencies. The outputs of these amplifiers go to opposite sides of the Z-drive, so they are in essence added simultaneously. A simplified version of this scheme was suggested by the Stanford group[83]. The schematic for this fast-slow system is shown in Fig. 27. For the slow stage, we used a programmable Kepco 500V bipolar power supply, which

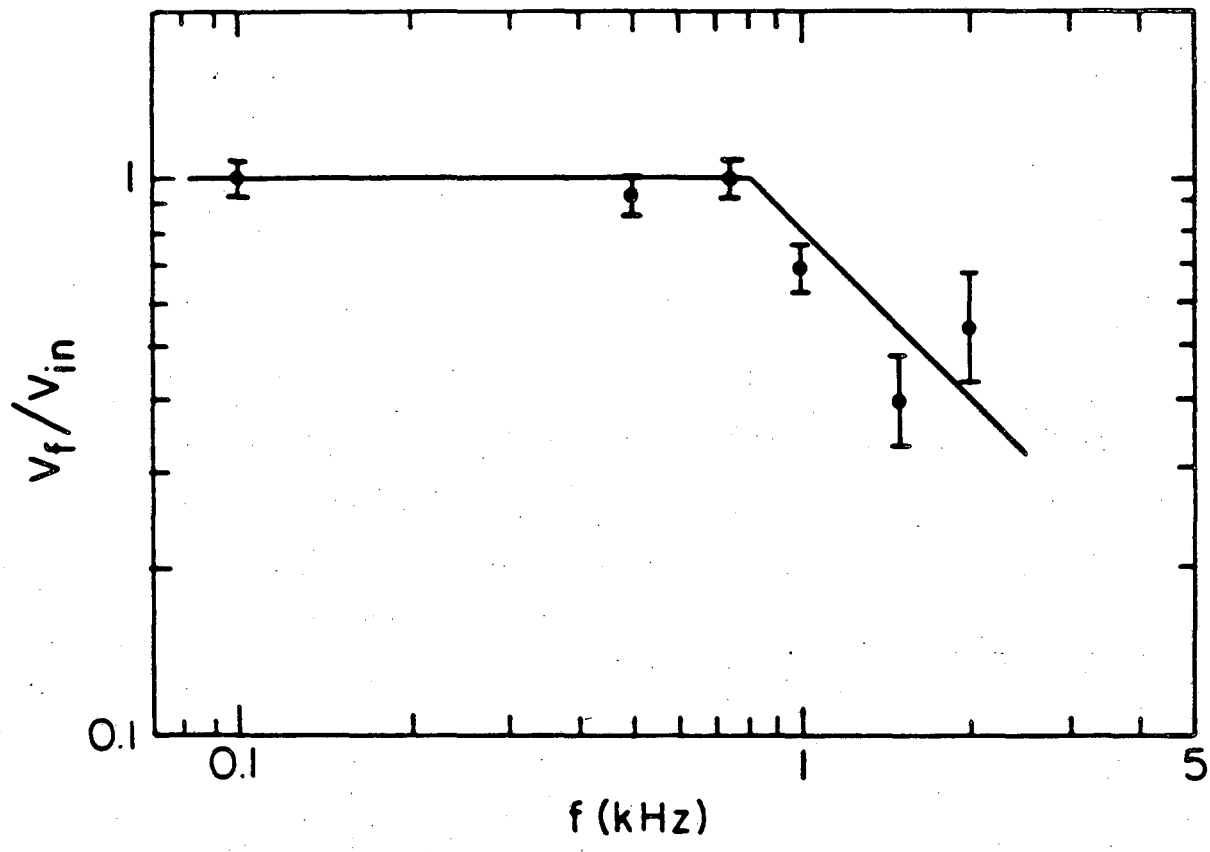

Fig. 26. Frequency response of feedback electronics.

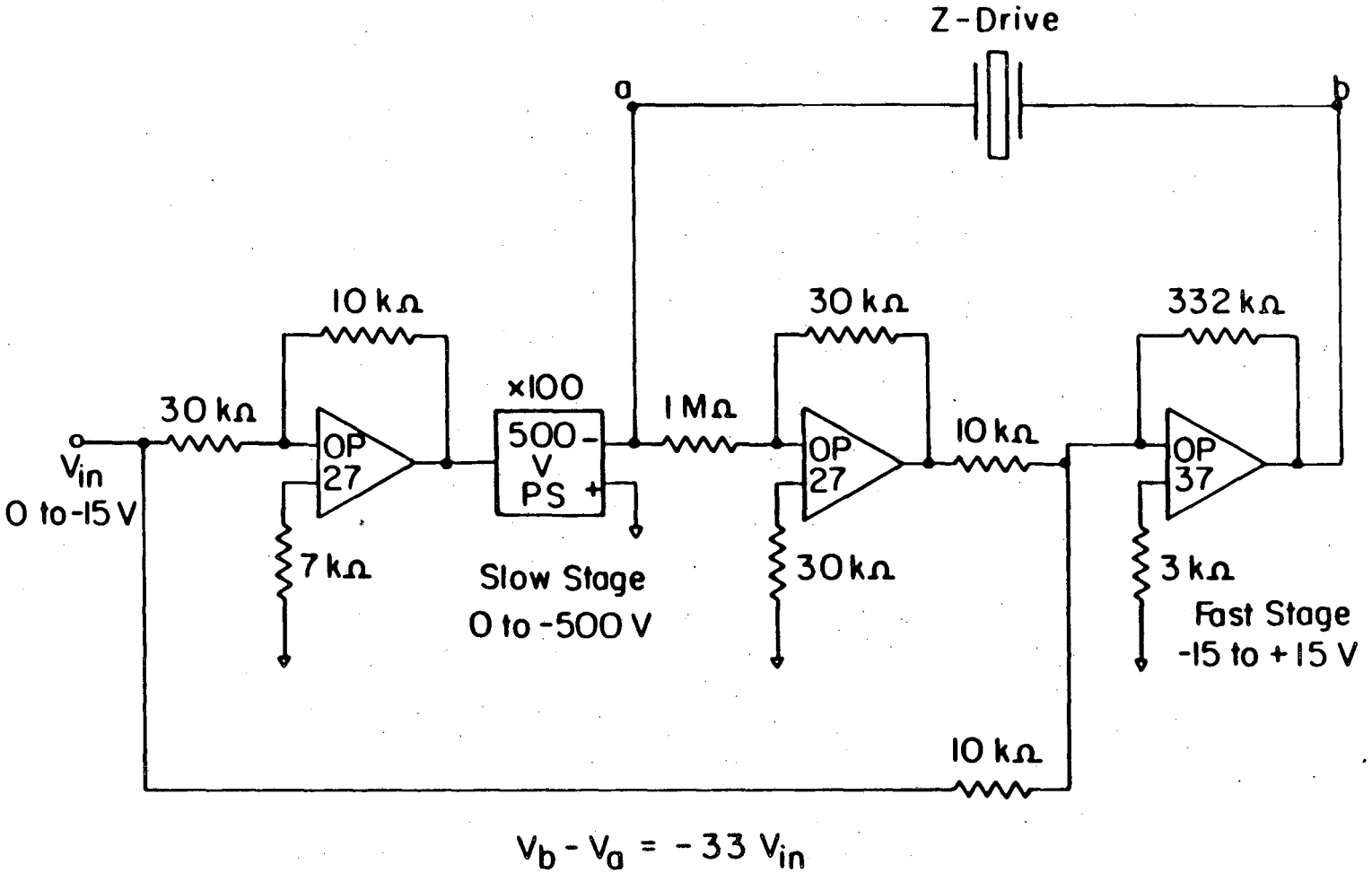

Fig. 27. Schematic of fast/slow high-voltage amplifier. The slow stage has since been replaced by a bipolar power supply.

had a 3 dB point of roughly 1 kHz. The fast stage was built around a PMI OP37 operational amplifier, and had a 3 dB point of 200 kHz.

With the current system, we can take a single 500 Å scan in about 3 seconds (1.5 seconds each direction). A 60 scan picture thus takes roughly 3 minutes.

The electronic feedback loop can, with minor modifications, also be used to make work function scans as well as topography scans. According to Eq (6.2), the work function ϕ is related to the current I and tip-to-surface spacing s by $\phi^{1/2} = (1/A)\, d(\ln I)/ds$. By adding a small AC modulation to the feedback voltage going to the Z-drive, one induces a modulation Δs in tip position. By lock-in detecting the output of the preamplifier, one obtains the corresponding current modulation ΔI, and one can obtain the work function. Some preliminary measurements along with a discussion of some of the problems associated with this method are presented in Chapter Eight.

E. Computer Interfacing

The computer performs several functions. Besides running the walker, the computer controls the data acquisition, and records, analyzes, and displays the data. It can also control UHV sensors (such as a residual gas analyzer) and monitor the feedback electronics. A diagram of the computer functions appears in Fig. 28.

The computer can start a scan by sending a trigger pulse to two analog ramps, which then generate 0-10 V triangle waves. These ramp signals are fed into high-voltage amplifiers which are connected

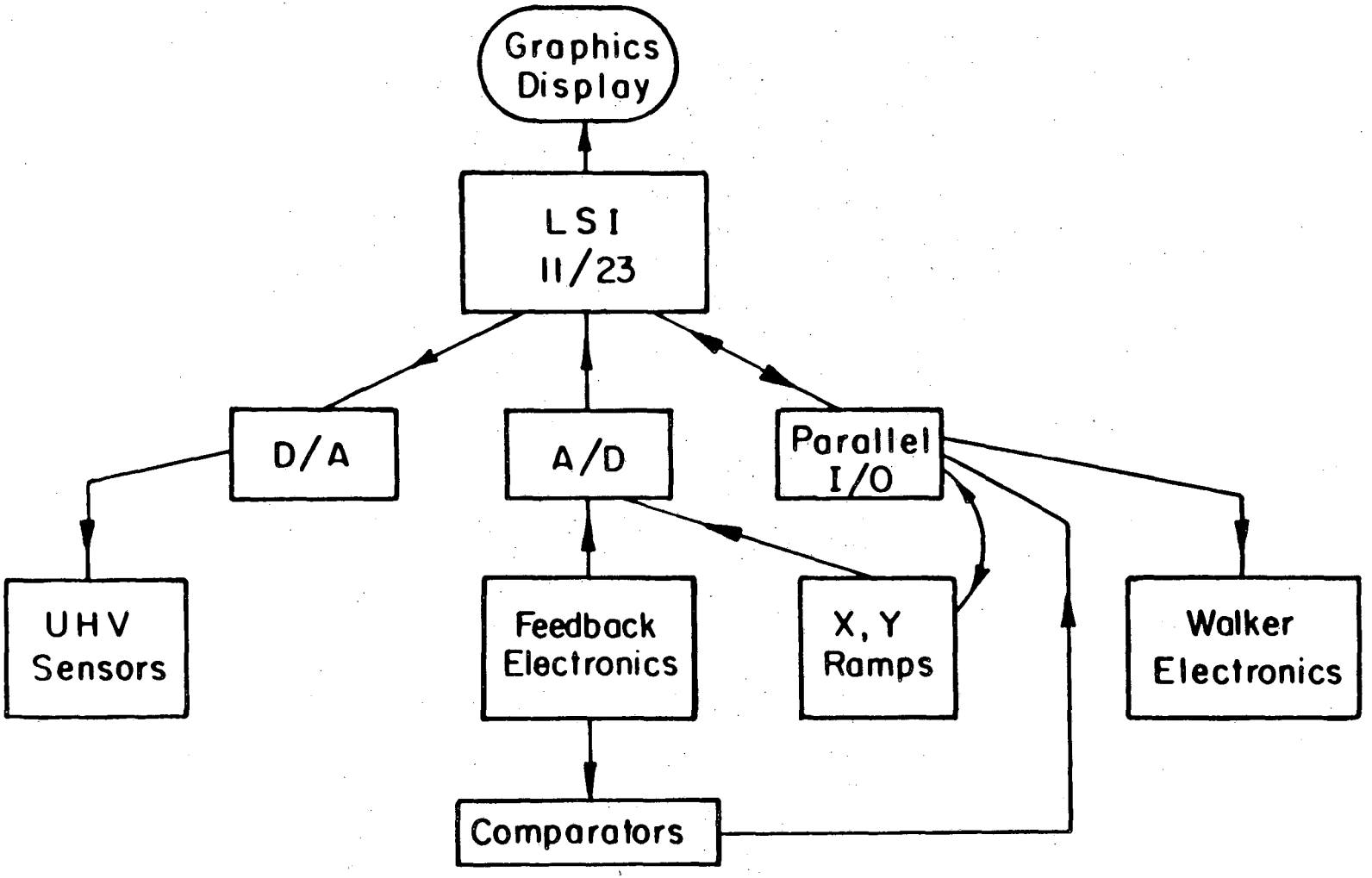

XBL 8410-4089

Fig. 28. Schematic of computer's functions.

directly to the X- and Y- drives. The X-ramp goes through many cycles during one Y-ramp cycle, creating a raster pattern. The computer only logs data when the X-ramp voltage is increasing in order to avoid hysteresis, which is observed to occur for scans taken in both directions. The X- and Y- ramp voltages and the Z-feedback voltage are fed into 12 bit A-to-D converters. The computer typically samples 256 points per X-scan. The rate at which data are taken can be easily varied. Changing this rate is a good way to check whether periodic features in the picture are in reality due to some low-frequency noise in the system.

The data consist of 256xn 3-component vectors, where n is the number of scans. To be useful, these data must be presented in some pictorial manner. A 16 color 480 x 640 pixel color monitor and graphics system is used to present the data. Hardcopy is obtained on a dot-matrix printer or a Hewlett-Packard XY plotter. A particular projection of the data is chosen by specifying a viewing direction; this is the direction from which the surface is viewed relative to the XYZ coordinate system defined by the piezoelectric drives. The particular transformation used is illustrated in Fig. 29. The projection in this viewing direction is then displayed on the monitor. Once in the computer, the picture can be rotated and displayed with hidden lines removed. These transformations are often invaluable, as certain ways of presenting data may reveal patterns the eye otherwise misses, and the most useful presentation may depend on the data involved. To facilitate such data transformations, we have recently obtained a

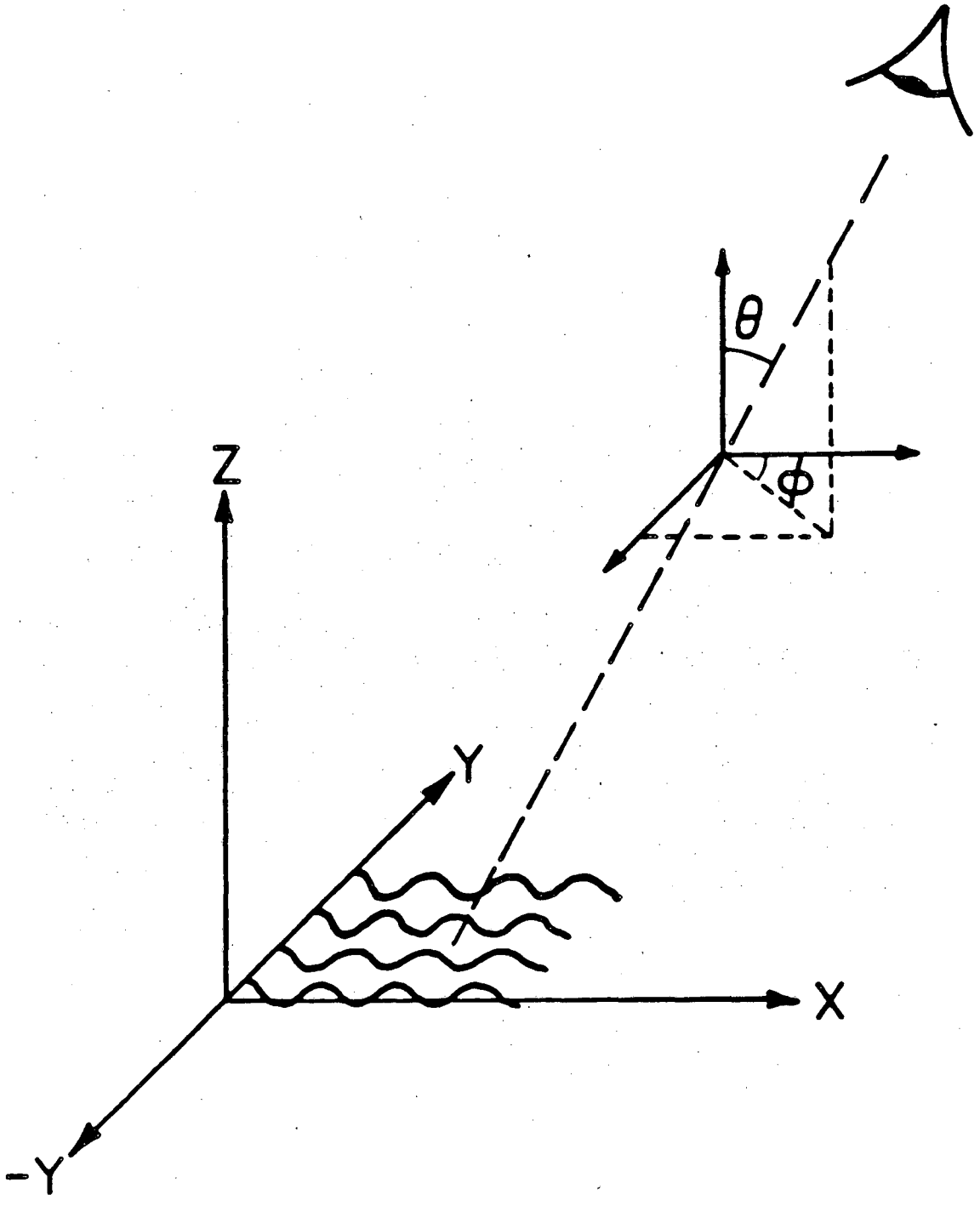

XBL 8410-4088

Fig. 29. Illustration of data presentation on the graphics terminal. Angles ϕ and θ are chosen, and specify a given viewing angle. The data points (X,Y,Z) are transformed into screen coordinates via the projection

$$X_S = -X\sin\phi + Y\cos\phi$$
$$Y_S = -X\cos\phi\cos\theta - Y\sin\phi\cos\theta + Z\sin\theta.$$

As θ is increased, the surface is viewed from an increasingly shallow angle, emphasizing the Z-variation.

high-resolution, 256 color Tektronix 4115B graphics workstation. With this system, the data can be presented as contour plots or as filled panels with a height-coded gray scale.

F. UHV System

For most surface work, it is important that the surface to be studied start out clean; that is, free of contamination from adsorbed materials such as hydrocarbons or water vapor. The time necessary for a gas at pressure P to cover a surface with one monolayer is given roughly by[66] $t = 2 \times 10^{-6}$ C/P, where t is in seconds, P is in torr, and C is the sticking coefficient, or probability that an impinging gas molecule sticks to the surface. In order to maintain clean surfaces for several hours, P must therefore be in the 10^{-10} torr range.

We have assembled our microscope in a Varian stainless steel ultra-high vacuum system capable of reaching 10^{-10} torr. The system is roughed by LN_2-cooled sorption pumps, and pumped by a set of five triode ion pumps. These are both oil-free and vibration-free, producing a clean and mechanically quiet environment for the microscope.

The UHV system will be fitted with a combination Low Energy Electron Diffraction/Retarding Field Analyzer Auger package. The LEED pattern can give the periodicity of the surface reconstruction, information which can be checked against the STM picture. The Auger analysis provides information as to the type of contaminants on the surface. These techniques will be used to determine whether the sample is globally clean and ordered.

Before the surface is studied, it must be cleaned. This must usually be done in situ, as any exposure to atmosphere will contaminate the surface. The cleaning procedure is quite material-dependent, but usually involves both heating to 500 to 1000°C or more and ion-bombardment. Heating is also necessary to induce most surface reconstructions. In our system it is impractical to heat the sample while it is on the microscope, as such high temperatures would depole the PZT. We have therefore devised a method to hold the sample on the microscope with spring clips and remove it to a manipulator for heating. Once on the manipulator the sample can be rotated into place for LEED/Auger analysis and sputtering. Ultimately, a sample introduction system will also be added to allow us to place a new sample on the microscope without exposing the entire chamber to atmosphere.

Currently none of the cleaning or surface analysis equipment has been installed. For purposes of testing the microscope, we used Au samples because of their relative inertness. Since no special cleaning procedures were employed, the surfaces were undoubtedly contaminated to some extent. Because of their low work function, we would not expect atomic resolution on such surfaces. The roughly 20 Å resolution we typically obtained is consistent with that observed by others on such surfaces[84].

CHAPTER EIGHT

MEASUREMENTS AND DISCUSSION

This chapter contains a discussion of what has been achieved so far with the Berkeley STM. Because we do not yet have the ability to clean our surfaces or characterize them with LEED or Auger, these results are quite preliminary. Nonetheless, some interesting capabilities of our microscope have been demonstrated.

All our work so far has been on Au. We have used both thin films and a bulk sample. The films were 800 Å thick, evaporated onto optically polished quartz substrates with 50 Å of Cr underneath to improve adhesion. The bulk sample was single-crystal, but as it had not been annealed, the face was certainly not atomically smooth. The samples were not cleaned in any special way.

In the following section we discuss the various types of noise present in our feedback system. The next section presents some results which were obtained in a vacuum of 10^{-8} torr. We show the exponential dependence of the tunneling resistance on the tip-to-surface separation, and compare the inferred work function to that obtained by a modulation technique. We present some of our better pictures, including one in which atomic steps were apparently resolved. Finally, we also discuss attempts to alter tip and surface in a controllable manner.

A. Noise and Spurious Effects

The noise in the feedback loop is both electrical and vibrational in origin. Because the microscope is in a feedback loop, such noise can be interpreted either as uncertainty in the tunneling current or in the Z-position of the tip. The effect of such noise is to limit the vertical resolution of the microscope. Other spurious signals such as large amplitude low frequency oscillations appear intermittently and can often be eliminated. The cause of these signals is not completely understood, but may depend on the details of the tip and sample, for example, whether or not a whisker connects them.

To reduce the electrical noise at the output of the current-to-voltage preamplifier, we mounted it in an electrically and magnetically shielded box, and shielded the input leads where possible. The noise at the output of the preamplifier had a white spectrum up to its roll-off of 30 kHz, with an rms amplitude of 0.5 to 1.0 mV. Since the preamplifier converts 1 nA to 10 mV, the corresponding current noise is 0.05 to 0.1 nA. This noise amplitude scaled with input lead length; placing the preamplifier inside the vacuum chamber should reduce the noise substantially. We typically operated with the tunneling current regulated at 2 to 20 nA; here the preamplifier noise was 2 to 5 times less than that due to other sources. To operate at tunneling currents much below 1 nA it will be necessary to reduce the preamplifier noise. By comparison, the Johnson current noise in a 1 MΩ resistor, typical of the gap resistance, is 0.02 nA in a 30 kHz bandwidth.

Significant high frequency noise is also produced by the other electronic components. The high frequency noise ($\lesssim$30 kHz) on the

tunneling current is ~3 times larger when the current is being regulated than when it is not. On the other hand, RF noise has not been a problem. We tested the microscope in an RF-shielded room and observed no reduction in noise.

One type of noise which did still plague us was that of 60 Hz noise. The equipment has been checked for ground loops; we believe the 60 Hz noise was due, at least in part, to inductive pickup. If the various cables leading to the bell jar were not shielded, the 60 Hz noise was orders of magnitude larger. The noise was intermittent; at times it corresponded to motion in Z of 1 Å, but typically was at the 0.1 Å level.

The dominant source of noise was vibrational, which occurred both at high and low frequencies. We have at times observed small-amplitude oscillations at roughly 0.5 Hz, a frequency not attenuated by the vibration isolation system. Such noise was rare and was probably related to background vibrations in the building. A more severe problem has been higher frequency acoustic noise. Even with the system in vacuum on the vibration isolation stage, loud noises coupled into the microscope, particularly those frequencies which excited mechanical resonances of the drives. We also saw a large component of vibrational noise at roughly 850 Hz. This apparently was due to some mechanical resonance: we could excite it with a loudspeaker and audio oscillator. The Q of the resonance was quite high, ≥30. We believe this resonance was that of the stainless steel bell jar, since tapping the bell jar produced noise at roughly the same frequency. The fact

that this noise coupled into the microscope implies that the vibration isolation needs to be improved. As previously mentioned, the problem was probably due to high frequency vibrations traveling down the springs or wires. Suspending the outer springs from Viton O-rings reduced this component of the noise by a factor of 2 to 4.

Finally, we observed two other types of spurious effects which usually could be eliminated. Often, after first locking the system into the feedback loop, we observed large amplitude oscillations with a gain-dependent frequency of around 1 Hz. In this mode the Z-drive oscillated between being fully extended and fully retracted. This noise could be eliminated by retracting the Z-drive, taking a step with the walker, moving to a different part of the sample, or employing the "ultrasonic cleaning" technique described in the next section. After such a cleaning procedure, we sometimes observed a second type of spurious signal, a "popcorn" or switching noise comparable in magnitude to that from other sources. This noise usually disappeared spontaneously within a few minutes.

The vertical resolution of the microscope is typically limited by the noise to 0.1 to 0.5 Å. The dominant noise source is usually vibrational, although on rare occasion 60 Hz noise has added up to 1 Å of noise to the Z-drive. For cleaner, higher work function surfaces the sensitivity to vertical tip position is enhanced; provided vibrational noise can be reduced somewhat, we expect to have vertical resolution consistently at the 0.1 Å level. The lateral resolution depends indirectly on the vertical resolution, but it also depends on

the radius of curvature of the tip. The creation of a stable tip which will give high lateral resolution consistently is one of the outstanding problems which remains with the STM.

B. Preliminary Results

To test the microscope, we walked the sample to the tip until contact was made, and took one step back with the walker, at which point the Z-drive could regulate tip position. We then employed an "ultrasonic cleaning" technique employed by Binning and Rohrer[58]. We increased the feedback loop gain until the system oscillated, causing the tip to vibrate against the sample at a frequency of several kHz. This technique has been effective in reducing the observed noise level.

We first tested the microscope in air. Thermal drifts were substantial, 50 Å/min or more. Acoustic noise was also substantial. Nevertheless, we were able to make reproducible one-dimensional scans and resolve 200 Å features.

Placing the microscope in the vacuum system naturally reduced the acoustic noise and thermal drift. In vacuum we verified the exponential nature of the tunneling on a thin film sample. By Eq. (6.2), this is equivalent to measuring the work function. We made the measurement by regulating the tip at a fixed current and varying the bias voltage at a low frequency, about 1 Hz. The feedback circuit then adjusted the spacing to keep the current constant. This AC technique avoided the problem of thermal drift and other low frequency noise.

The results are shown in Fig. 30, plotted as resistance vs relative tip position on a semi-logarithmic scale. Data were taken at three different times on the same sample. Over roughly two decades the resistance is exponential in tip-to-surface spacing. There were some deviations, particularly at high resistances where the bias voltage approached the measured work function. The work function inferred from this curve is roughly 0.15 eV, in contrast to the value of 5 eV expected on clean Au surfaces[66]. Our value is consistent with other STM measurements on uncleaned Au surfaces[84].

We also measured the work function of our bulk sample using an AC modulation and lock-in detection technique, as discussed in the previous chapter. We varied the tip position roughly 0.6 Å at a frequency of 400 Hz, and lock-in detected the signal out of the preamplifier. We obtained a value for the work function of 0.2 ± 0.06 eV, consistent with the previous measurement. The problem with this measurement is that, because of stray inductance between leads, the application of an AC signal to the Z-drive produced a sizeable signal at the preamplifier through inductive pickup. The size of this signal varied linearly with frequency, and at 2 kHz the signal at the output of the preamplifier roughly equaled the signal to the Z-drive! Of course, the inductive signal was 90° out of phase with the modulation signal; we set the phase adjustment on the lock-in amplifier to detect only the in-phase component. Still, best results were obtained when the quadrature signal was smaller than the in-phase signal, which occurred below about 500 Hz. The modulation must be substantially faster if

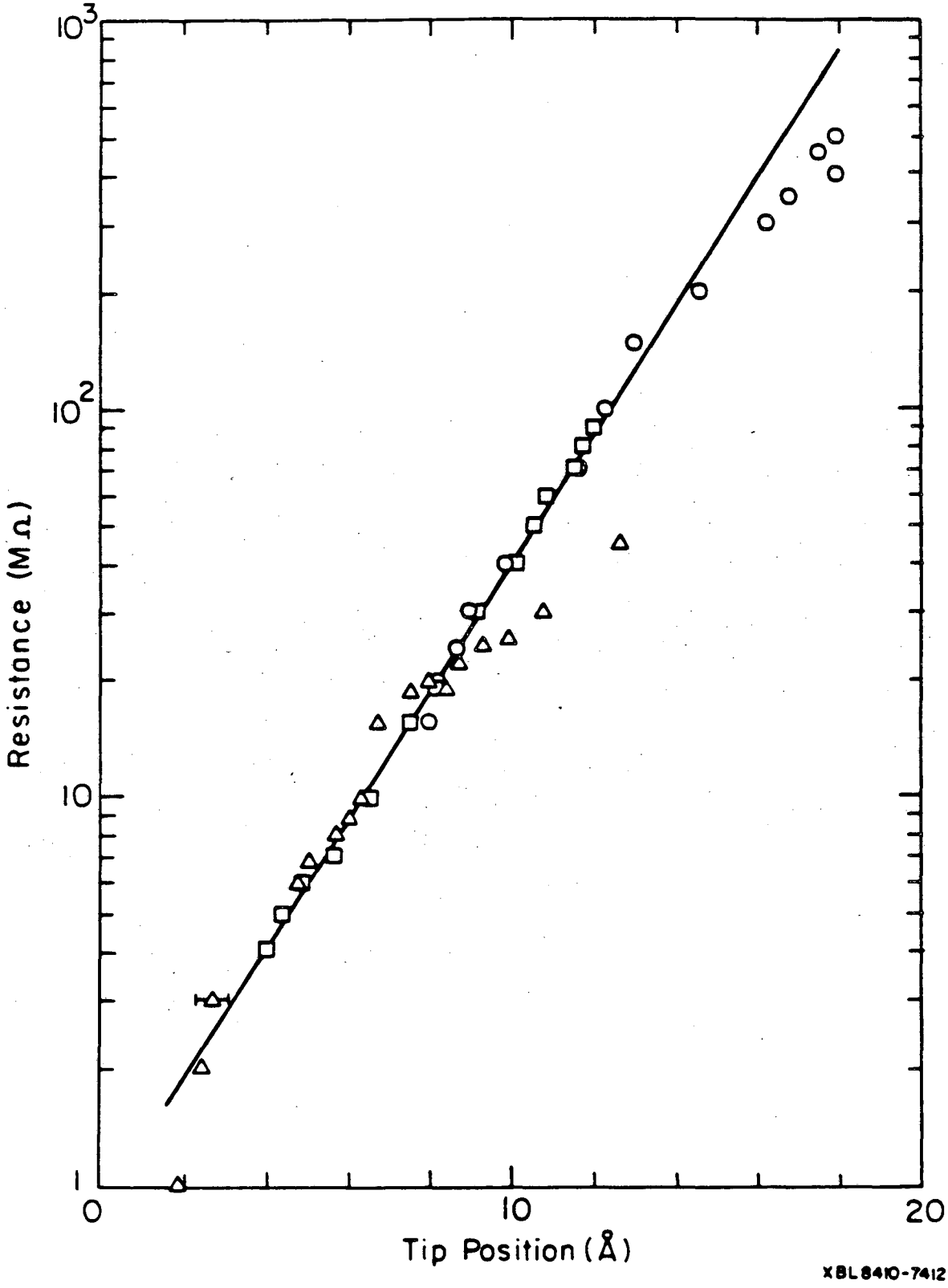

Fig. 30. Data showing exponential dependence of tunneling resistance on gap spacing. Inferred work function is roughly 0.15 eV, much less than the value of 5 eV for a clean surface.[66]

one wishes to make work function measurements while scanning at a reasonable rate. In this case the stray inductance and the preamplifier bandwidth become limitations. For the same reason it is not currently practical to use an AC bias voltage between tip and sample.

A typical picture is shown in Fig. 31. The sample was untreated bulk Au. The roughly 20 Å lateral resolution and 100 Å features are similar to other STM results on untreated surfaces.

In one instance, in looking at the evaporated Au film, we obtained a lateral resolution better than 10 Å. This result has not been reproducible, and was probably a fortuitous occurrence of finding a clean portion of the film. Three views of this picture are shown in Fig. 32. These views clearly illustrate the importance of being able to rotate the data. Figure 32(a) shows the data as they were displayed in real time during data acquisition. Figures 32(b) and (c) show views corresponding to different projections of the data. The periodicity is much more easily discerned in these views. In Fig. 32(b), steps are clearly visible. The height of each step is roughly 2 Å. The step widths increase by 3.1 Å per step, and are half-integral multiples of this unit length; looking from left to right, the step widths are 5.5, 5.5, 7.5, and 8.5 unit lengths, all ± 0.15 unit lengths. One possible interpretation of this result is that these features are atomic steps, with the value 3.1 Å corresponding to a lattice spacing. The lattice spacing in bulk Au is 4.1 Å.[85] The 30% discrepancy could be due to calibration error in the drives, as the calibration was inferred from their geometry and comparison to similar drives calibrated with an

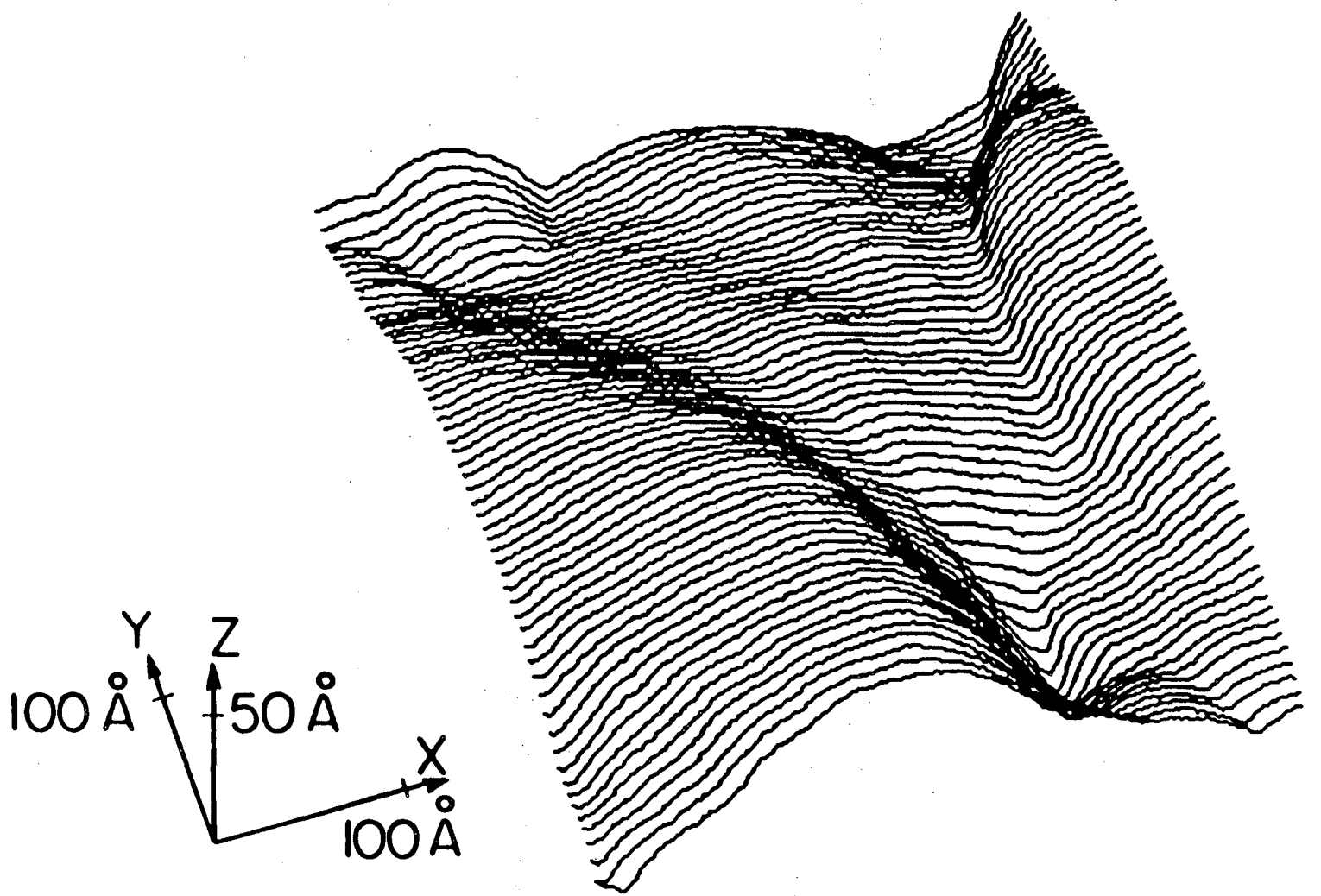

XBL 8410-4177

Fig. 31. Portion of a (210) Au surface that has not been cleaned or annealed.

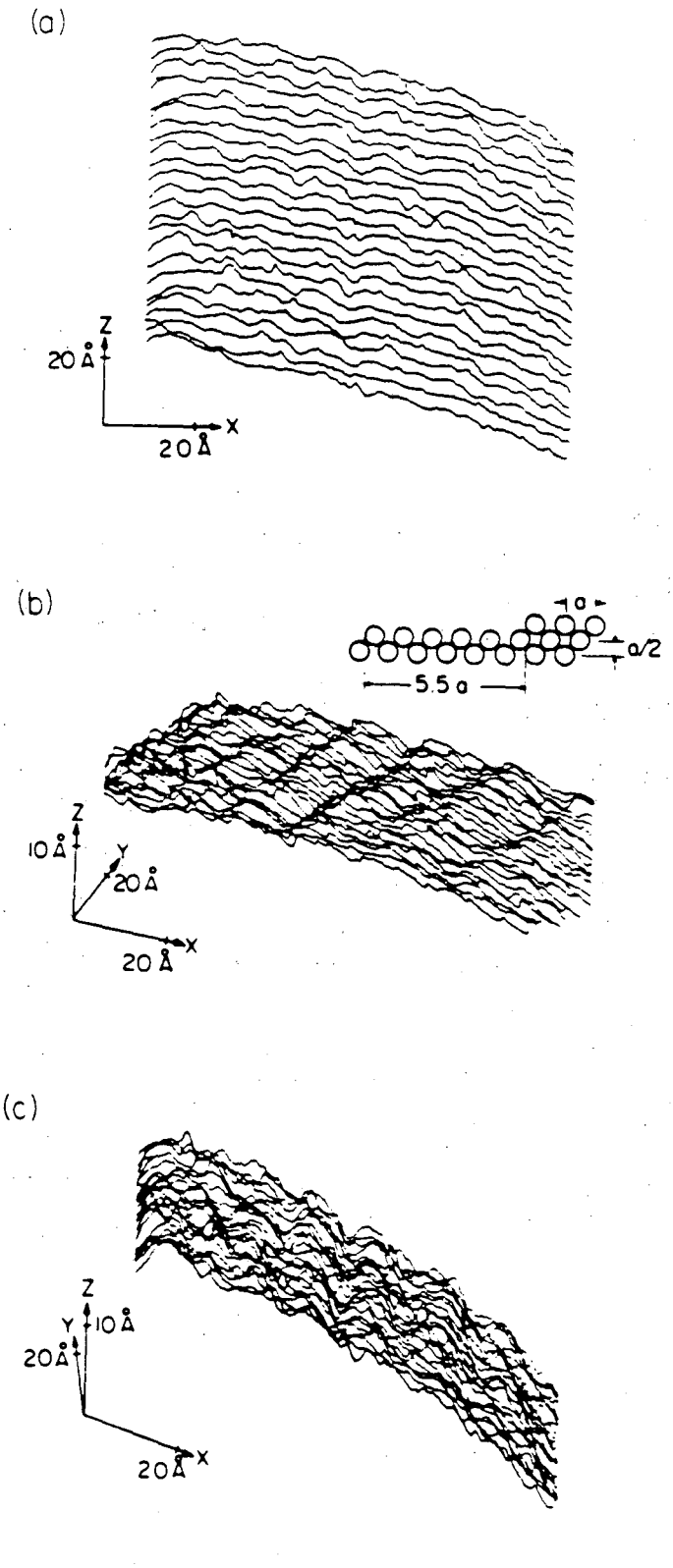

XBL 8410-4180

Fig. 32. Several views of steps observed on an evaporated Au film. (a) Data as displayed in real time. In (b) and (c) stepped structure is apparent. Inset in (b) shows a possible atomic arrangement for such steps. Such an interpretation is quite tentative, considering the quality of the data, its irreproducibility, and the unknown surface characteristics.

interferometer. It appears the microscope resolved atomic step structure, but not the individual atoms which composed the steps.

We have observed the effect of applying a relatively large voltage (~10 V) between tip and sample. Binning and Rohrer reported that the use of fields on the order of 10^8 V/m led to increased resolution, perhaps by "growing" a sharper tip in some way[58]. We applied 10^7 to 10^8 V/m for several minutes, and observed no increase in resolution. We did observe some surface distortion in the region where the field was applied.

Another process we studied was that of gently scratching the surface with the tip. We made the scratches by moving the tip to the desired region, regulating the tunneling current at about 1 μA, (where the preamplifier saturated), and moving the X- or Y- drive in the desired direction. This current corresponded to a tunneling resistance of $10^4 \Omega$, a value much lower than the 1 MΩ or so used while taking scans. The results are shown in Fig. 33. Figure 33(a) shows the area before scratching; we chose it for its combination of fairly flat region and recognizable features. Figure 33(b) shows the result after attempting a vertical scratch down the center of the region. A trench is clearly visible. Figure 33(c) is the result of attempting a horizontal scratch down the center. We did not succeed in scratching the surface, but evidently we created a V-shaped groove in the side of a hill. This result leads us to believe the tip was not in contact with the surface during the entire scratch, but only when it encountered a sharp feature which the feedback loop could not track quickly enough,

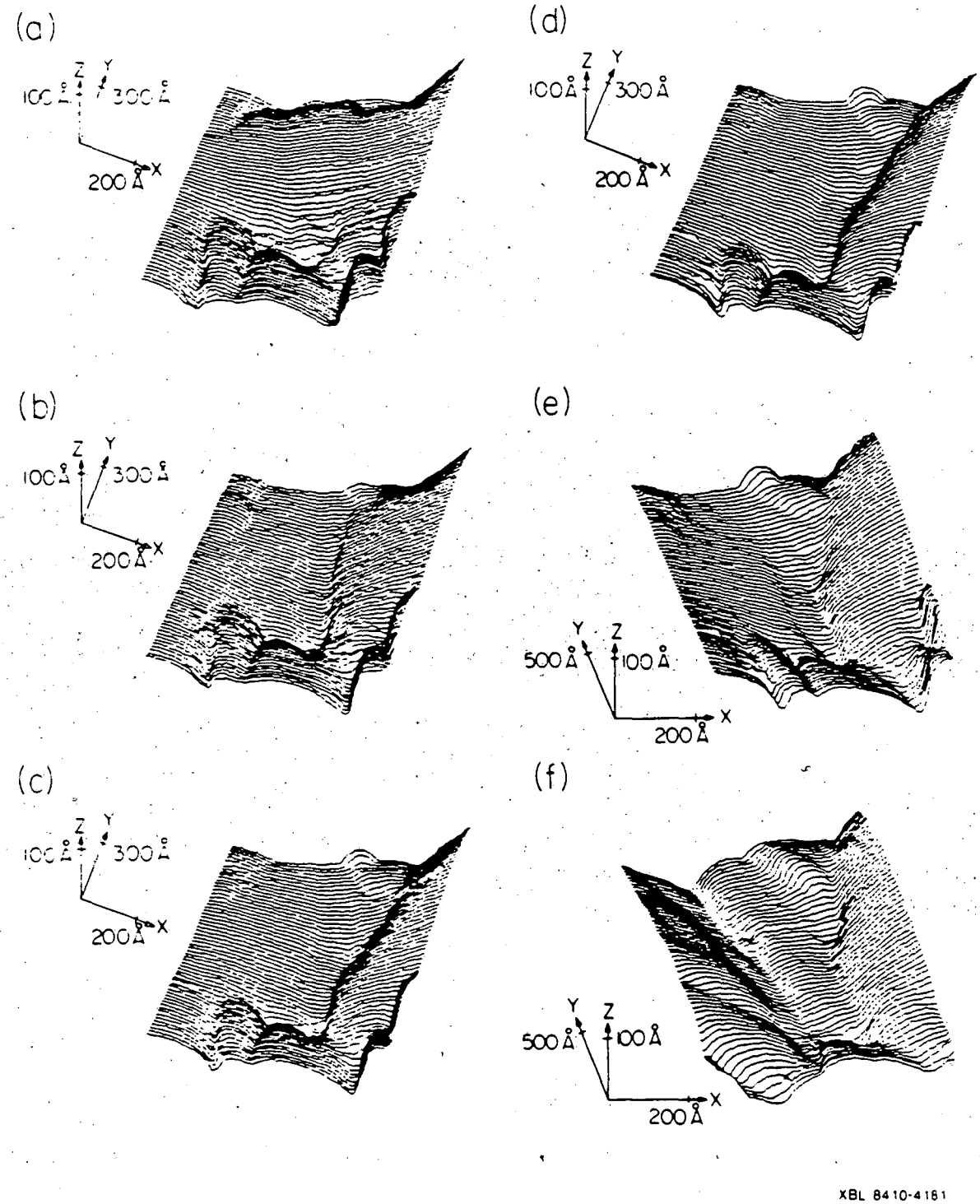

Fig. 33. Series of pictures showing results of scratching tip along surface.

so that the tip touched the surface. Figure 33(d) is a repeat picture taken eight minutes later to ensure the observed features were reproducible. (This picture, unlike the previous one, made use of the hidden line algorithm). Figures 33(c) and (d) are nearly identical, indicating very good reproducibility. The drift in the eight minutes between pictures was less than 30 Å. Operating the system in an air-conditioned room probably reduced the thermal drift, as did assembling the microscope on a quartz plate. Figure 33(e) displays the same data as Fig. 33(d) but from a different viewing angle. Finally, Fig. 33(f) shows the result of scratching another vertical trench to the left of the first one.

The size of these scans can be estimated from a single scan, such as that shown in Fig. 34. The trenches are roughly 20 Å deep and 50 Å wide. As the trenches were dug with the tip, this scan provides some crude information about the tip size. Of course, without knowledge of the actual tip size, one cannot be certain of the actual surface structure, as the observed structure will be some convolution of tip and surface structure. The bulge at the top of Fig. 34(c) indicates a lateral resolution of better than 40 Å, a reasonable value if the tip size is that suggested by the trench scans. We have thus demonstrated the ability to perform micro-machining of some sort at the 50 Å level, and to observe the results.

Figures 35 and 36 show a dent in the surface observed at the time of the tip scratching attempts. Figure 35 is the standard line plot, and Fig. 36 is a gray-scale image produced on the Tektronix graphics

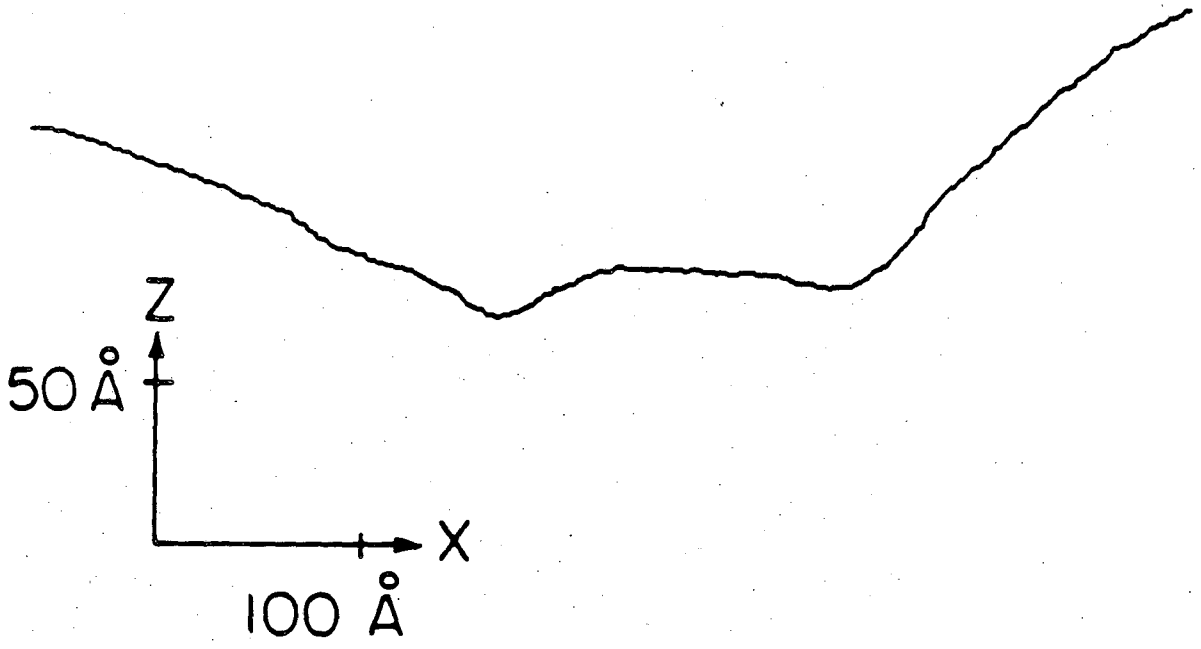

XBL 8410-4178

Fig. 34. Single scan from Fig. 33(f) showing dimensions of trenches.

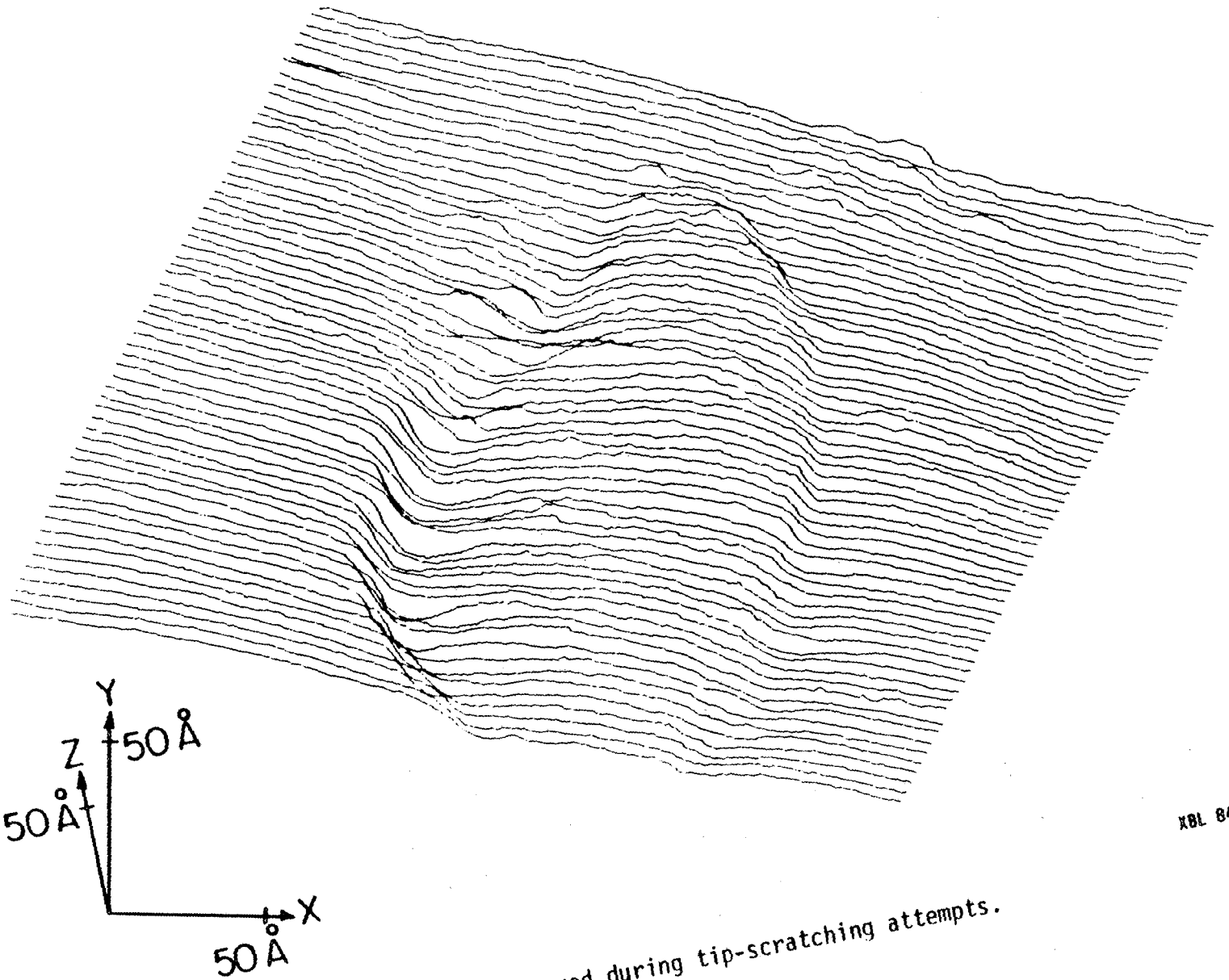

XBL 8410-4179

Fig. 35. Dent in surface observed during tip-scratching attempts.

Fig. 36. Gray-scale fill of data shown in Fig. 35.

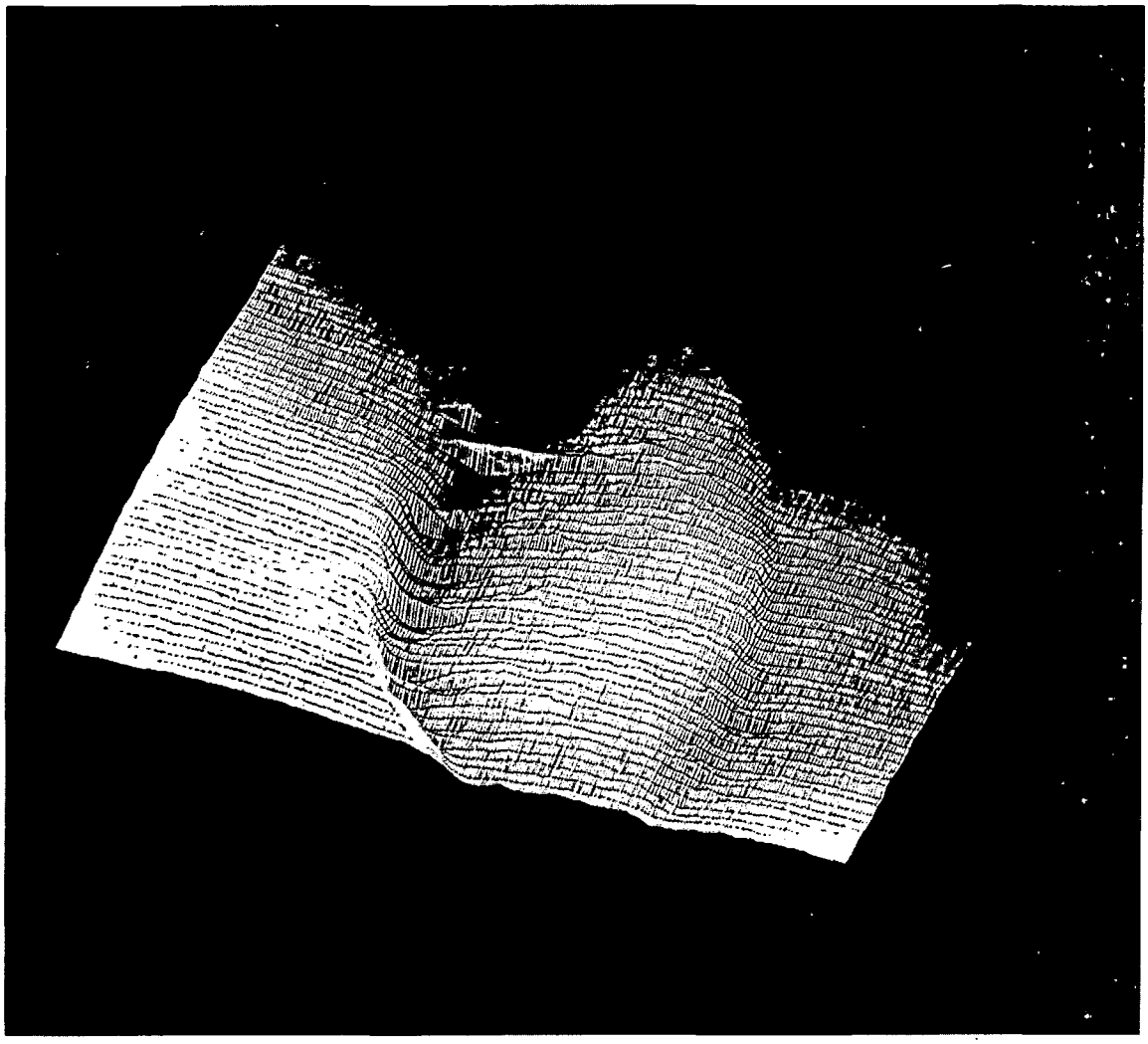

XBC 849-6795

system. The intensity of the image is proportional to its height, with most intense representing the highest. This representation makes obvious the overall tilt to the data. Such a graphics presentation can give a more useful and objective view of a surface than line plots, which the eye is prone to misinterpret. We expect that in the future, such graphics-handling capabilities will become increasingly useful.

CHAPTER NINE

SUMMARY

In conclusion, we have assembled a STM which, on uncleaned surfaces, has typical lateral resolution of 20 to 30 Å and on one occasion had better than 10 Å resolution. Such performance is comparable to that achieved with other STM's on similar surfaces. We have verified the exponential nature of the vacuum tunneling, and have demonstrated the ability to measure the work function of a surface. Finally, we have demonstrated the potential of the STM to machine surfaces, at least to the extent of making relatively controlled scratches in a soft surface with dimensions of a few tens of Å.

A number of improvements to the STM are currently underway. A new vibration isolation system with improved acoustic damping should reduce vibrational noise. Placing the preamplifier inside the vacuum chamber should reduce electrical noise. A new XYZ-drive configuration along with faster electronics are being built and should extend the frequency response of the feedback loop. We are in the process of adding LEED, Auger, a heater and a sputtering system to the UHV system which will allow in situ cleaning and characterization of surfaces. We are confident that clean surfaces with their subsequent high work functions will allow imaging with atomic resolution.

Although it does not yet have atomic resolution, the Berkeley STM is operational, and we are now embarking on a number of experiments. We propose to study a Au replica of a virus as well as make further attempts at micro-machining. Neither of these experiments requires

atomic resolution. With atomic resolution, a cornucopia of experiments presents itself. The STM could be very profitably employed studying semiconductor surfaces and their reconstructions. We are also interested in laser-annealed surfaces of metals and semiconductors. The field of surface physics as a whole is still quite young; the recent development of such a powerful tool as STM should give rise to many exciting applications.

REFERENCES

1. J. Bardeen, L. Cooper, and J. R. Schrieffer, Phys. Rev. 108, 1175 (1957).
2. J. A. Pals, K. Weiss, P. M. T. M. van Attekum, R. E. Horstman and J. Wolter, Physics Reports (Review Section of Physics Letters) 89, 323 (1982).
3. D. J. Van Harlingen, Physica 109 and 110B + C, 1710 (1982).
4. G. Schon, in Festkorperprobleme (Advances in Solid State Physics) edited by J. Treusch (Vieweg, Braunschweig, 1981), Vol. 21, p. 341.
5. C. M. Falco and J. C. Garland, in Nonequilibrium Superconductivity, Phonons, and Kapitza Boundaries, edited by Kenneth E. Gray (Plenum Press, New York, 1981), p, 521.
6. V. L. Ginzburg, J. Phys. USSR, 8, 148.
7. C. J. Gorter and H. B. G. Casimir, Phys. Z. 35, 953 (1934); C. J. Gorter and H. B. G. Casimir, Z. Techn. Phys. 15, 539 (1934).
8. W. F. Vinen, in Superconductivity, edited by R. D. Parks (Dekker, New York, 1969), p. 1167.
9. J. Wilkes, An Introduction to Liquid Helium, (Clarendon Press, Oxford, 1970), p. 53.
10. J. Clarke and S. M. Freake, Phys. Rev. Lett. 29, 588 (1972).
11. N. K. Welker and F. D. Bedard, in SQUID-Superconducting Quantum Interference Devices and their Applications, edited by H. D. Hahlbohm and H. Lubbig (de Gruyter, Berlin, 1977), p. 200.
12. A. A. J. Matsinger, R. de Bryun Ouboter, and H. Van Beelen, Physica 93B, 63 (1978).

13. A. D. Smith, M. Tinkham, and W. J. Skocpol, Phys. Rev. B 22, 4346 (1980).

14. M. V. Karsovnik, V. V. Ryazanov, and V. V. Schmidt, Eksp. Teor. Fiz. Pis'ma Red. 33, 373 (1981), JETP Lett. 33, 356 (1981); V. V. Ryazanov and V. V. Schmidt, Solid State Commun. 40, 1055 (1981).

15. V. V. Ryazonov and V. V. Schmidt, Solid State Commun. 42, 733 (1982).

16. A. Th. A. M. De Waele, R. deBryun Ouboter, and P. B. Pipes, Physica 65, 587 (1973).

17. P. B. Pipes and D. H. Darling, in Proceedings of the International Conference on Low Temperature Physics, LT14, edited by M. Krusius and M. Vuorio (North-Holland, Amsterdam, 1975), p. 521.

18. M. Shott and A. J. Walton, Phys. Lett. 60A, 53 (1977).

19. Y. M. Galperin, V. L. Gurevich, and V. I. Kozub, Zh. Eksp. Teor. Fiz. 66, 1387 (1974) [Sov. Phys.JETP 39, 680 (1974)].

20. J. C. Garland and D. J. Van Harlingen, Phys. Lett. 47A, 432 (1974).

21. N. V. Zavaritskii, Zh. Eksp. Teor. Fiz. Pis'ma Red. 19, 205 (1974) JETP Lett. 19, 126 (1974).

22. C. M. Pegrum, A. M. Guenault, and G. R. Pickett, in Proceedings of the International Conference on Low Temperature Physics, LT14, edited by M. Krusius and M. Vuorio (North-Holland, Amesterdam, 1975), p. 513.

23. C. M. Falco, Solid State Commun. 19, 623 (1976).

24. D. J. Van Harlingen, D. F. Heidel, and J. C. Garland, Phys. Rev. B 21, 1842 (1980).

25. J. Clarke, in Nonequilibrium Superconductivity, Phonons, and Kapitza Boundaries, edited by Kenneth E. Gray, (Plenum Press, New York, 1981), p. 353, M. Tinkham and J. Clarke, Phys. Rev. Lett. 28, 1366 (1972); M. Tinkham, Phys. Rev. B 6, 1747 (1972).

26. C. M. Falco, Phys. Rev. Lett. 39, 660 (1977).

27. M. Tinkham, Phys. Rev. B 22, 2594 (1980).

28. O. Entin-Wohlman and R. Orbach, Phys. Rev. B 22, 4271 (1980).

29. S. N. Artemenko and A. F. Volkov, Zh. Eksp. Teor. Fiz. 70, 1051 (1976) [Sov. Phys., JETP 43, 548 (1976)].

30. D. J. Van Harlingen, J. Low Temp. Phys. 44, 163 (1981).

31. S. J. Battersby and J. R. Waldram (unpublished).

32. J. Clarke, B. R. Fjordboge, and P. E. Lindelof, Phys. Rev. Lett. 43, 642 (1979).

33. D. F. Heidel and J. C. Garland, J. Low. Temp. Phys. 44, 295 (1981).

34. H. J. Mamin, J. Clarke and D. J. Van Harlingen, Phys. Rev. B 29, 3881.

35. C. J. Pethick and H. Smith, Ann. Phys. (N.Y.) 119, 133 (1979).

36. W. E. Lawrence, P. B. Pipes, and K. Schwartzman, Phys. Rev. B 23, 4476 (1981).

37. P. M. Selzer and W. M. Fairbank, Phys. Rev. 48A, 279 (1974).

38. G. J. Dolan and L. D. Jackel, Phys. Rev. Lett. 39, 1629 (1977).

39. J. M. Aponte, J. Low Temp. Phys. 51, 189 (1983).

40. C. C. Chi and J. Clarke, Phys. Rev. B 19, 4495 (1979).

41. A. Schmid and G. Schon, J. Low Temp. Phys. 20, 207 (1975).

42. A. Schmid, J. Low Temp. Phys. 41, 37 (1980).

43. Schmid (Ref. 42) and Schon (Ref. 4) both suggest that $\sigma(T)=\sigma(T_c)[1+(\Delta/2k_BT)\ln(\Delta/\Gamma)]$ near T_c, where Γ is an appropriate pair-breaking energy. This expression is an approximation to the conductivity observed in electromagnetic absorption, where case-II coherence factors are applicable. However, while in the electromagnetic case the superfluid is accelerated, in the presence experiment the superfluid is not accelerated, and it appears to us that the case-II coherence factors are not appropriate. We would expect $\sigma(T)$ to drop smoothly from its value at T_c as the temperature is lowered, reflecting the decrease in the quasiparticle population.

44. P. Dolan and P. B. Pipes, private communication.

45. J. Martinis and J. Clarke, IEEE Magn. MAG-19, 446 (1983).

46. F. J. BLatt, P. A. Schroeder, C. L. Foiles, and D. Greig, Thermoelectric Power of Metals (Plenum, New York, 1976), p. 30.

47. K. A. Gschneidner, in Solid State Physics, edited by F. Seitz and D. Turnbull (Academic, New York, 1964), Vol. 16, p. 275.

48. We note that the value of N(0) used to estimate τ_{Q*} from λ_{Q*} is consistent with the value we have used for $1/\sigma$, $4\times10^{-16}\Omega m^2$, if one takes $v_F=1.36\times10^6$ ms^{-1}, the free electron value of the Fermi velocity divided by the thermal effective mass. The best value for $1/\sigma$ in aluminum is still somewhat of an open question. The somewhat more traditional value of $9\times10^{-16}\Omega m^2$, used by Chi and Clarke (Ref. 40) for example, is inconsistent with the values used for v_F and N(0). The confusion results from the different kinds of effective

mass in aluminum. If we chose the value $9\times10^{-16}\Omega m^2$ for $1/\sigma$, our inferred values for τ_E would be smaller by a factor 4/9.

49. We note that if T_c were larger than our estimate, the slope of the plot of λ_{Q*} vs $1-T/T_c$ would become steeper in the region near T_c. However, we feel that the error introduced by obtaining T_c from the resistive transition is not large enough to affect the slope significantly in the temperature region that we were able to study.

50. T. R. Lemberger and J. Clarke, Phys. Rev. B23, 1100 (1981).

51. M. Stuivinga, J. E. Mooij, and T. M. Klapwijk, Physica 108B + C, 1023 (1981).

52. M. Stuivinga, Ph.D. thesis, Technische Hogeschool Delft, 1983.

53. T. R. Lemberger, Phys. Rev. Lett. 52, 1029 (1984).

54. J. Clarke and J. L. Paterson, J. Low. Temp. Phys. 15, 491 (1974).

55. O. V. Lounasmaa, Experimental Principles and Methods Below 1 K (Academic, New York, 1974), p. 246.

56. S. Kaplan, J. Low. Temp. Phys. 37, 343 (1979).

57. G. Binnig, H. Rohrer, Ch. Gerber, and E. Weibel, Phys. Rev. Lett. 49, 57 (1982).

58. G. Binnig and H. Rohrer, Surf. Sci. 126, 236 (1983).

59. L. Esaki, Phys. Rev. 109, 603 (1958).

60. I. Giaver, Phys. Rev. Lett. 5, 147 (1960); I. Giaver, ibid. 5, 464 (1960).

61. B. D. Josephson, Phys. Lett. 1, 251 (1962).

62. Although the vast majority of tunneling devices are made with oxide tunnel barriers, recently much progress has been made fabricating junctions with artificial barriers. See, for example, S.T. Ruggiero, E. Track, and D.E. Prober, Bull. Am. Phys. Soc. 29, 407 (Program of the 1984 March Meeting in Detroit, Michigan; 26-30 March 1984).

63. G. Binnig, H. Rohrer, Ch. Gerber, and E. Weibel, Appl. Phys. Lett. 40, 178 (1981).

64. John Moreland, S. Alexander, M. Cox, R. Sonnenfeld, and P. K. Hansma, Appl. Phys. Lett. 43, 387 (1983).

65. R. D. Young, J. Ward, and F. Scire, Phys. Rev. Lett. 40, 178 (1981).

66. E. Clayton Teague, Ph.D. Thesis, North Texas State University, 1978.

67. N. D. Lang and W. Kohn, Phys. Rev. B 1, 4555 (1970); N. D. Lang and W. Kohn, ibid. 3, 1215 (1971); N. D. Lang and W. Kohn, ibid. 7, 3541 (1973).

68. R. D. Young, J. Ward, and F. Scire, Rev. Sci. Instrum. 43, 999 (1972).

69. John G. Simmons, J. Appl. Phys. 34, 1793 (1963).

70. J. Tersoff and D. R. Hamann, Phys. Rev. Lett. 50, 1998 (1983).

71. N. Garcia, C. Ocal, and F. Flores, Phys. Rev. Lett. 50, 2002 (1983).

72. A. Baratoff, IBM Research Report (July 10, 1984).

73. G. Binnig, H. Rohrer, Ch. Gerber, and E. Weibel, Bull. Am. Phys. Soc. 28, 461 (1983).

74. See L. D. Marks and D. J. Smith, Nature 303, 316 (1983), for example.

75. We have not measured the absolute vibrational level in our laboratory. Previous measurements indicate that the vibration level in the sub-basement is 30 times less than on the ground floor, and 10^4 times less than on the fifth floor, over a broad range of frequencies (E. Commins, private communication).

76. S. Elrod and C. Quate, private communication.

77. D. Esteve, private communication.

78. J. Golovchenko, private communication.

79. C. F. Beards, Structural Vibration (Wiley, West Sussex, 1983), p. 74.

80. Mel Kullin (Channel Industries), private communication.

81. A. Bryant, S. Elrod, A. de Lozanne, D. Smith, Sang-Il Park, and C. Quate, private communication.

82. R. Wilson; G. Binnig and H. Rohrer, private communication.

83. A. Bryant, Sang-Il Park, and C. Quate, private communication.

84. A. Bryant and C. Quate; J. Golovchenko, private communication.

85. C. Kittel, Introduction to Solid State Physics, (Wiley, New York, 1976), p. 31.

This report was done with support from the Department of Energy. Any conclusions or opinions expressed in this report represent solely those of the author(s) and not necessarily those of The Regents of the University of California, the Lawrence Berkeley Laboratory or the Department of Energy.

Reference to a company or product name does not imply approval or recommendation of the product by the University of California or the U.S. Department of Energy to the exclusion of others that may be suitable.

TECHNICAL INFORMATION DEPARTMENT
LAWRENCE BERKELEY LABORATORY
UNIVERSITY OF CALIFORNIA
BERKELEY, CALIFORNIA 94720